Boundary Layer Ingestion

Theoretical and Experimental Research

(Registration Number: 022#15#MT#FPP)

Tarık Hartuç

Master of Science Thesis

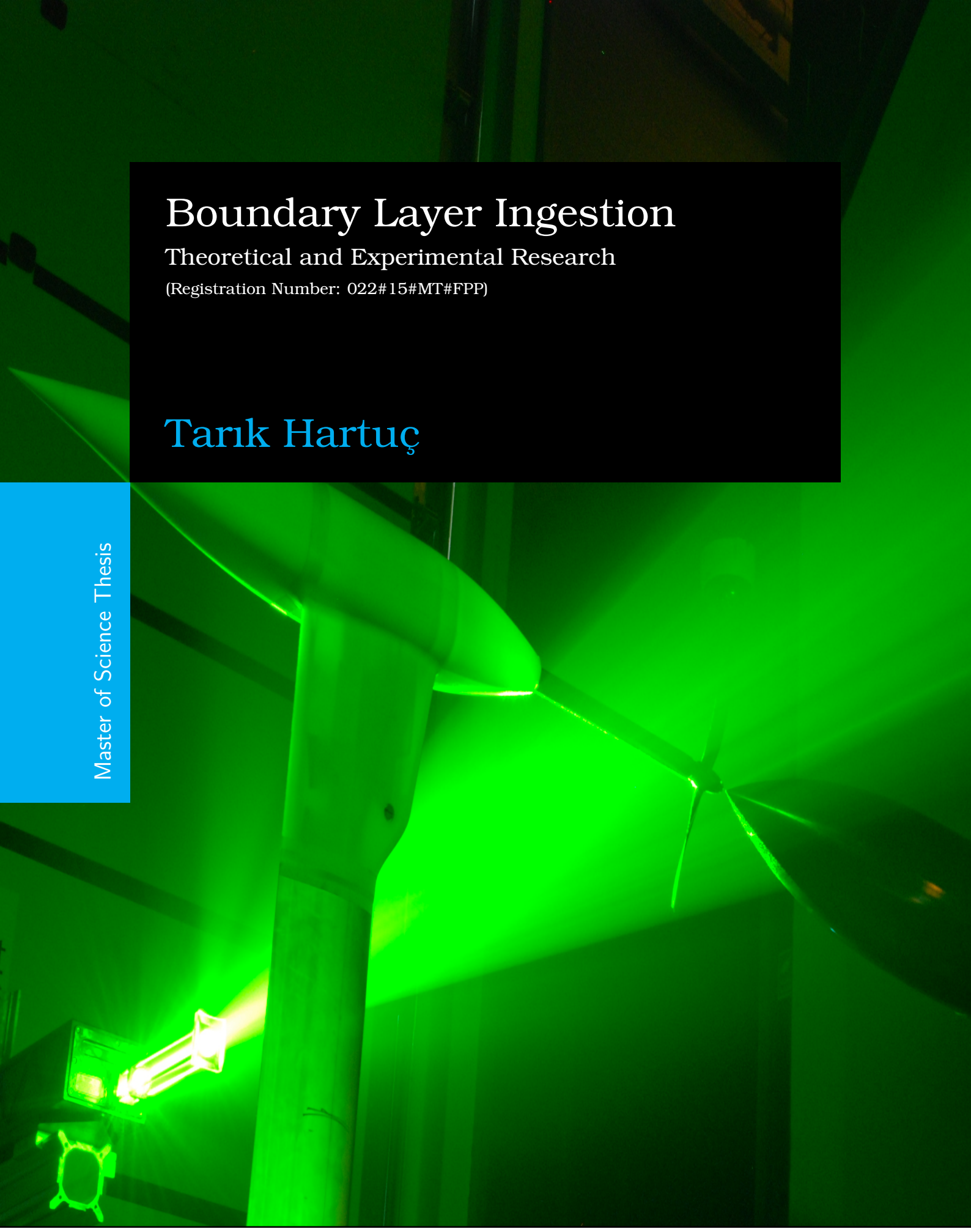

TU Delft Delft University of Technology

Faculty of Aerospace Engineering

Boundary Layer Ingestion

Theoretical and Experimental Research

(Registration Number: 022#15#MT#FPP)

Master of Science Thesis

For the degree of Master of Science in Flight Performance and Propulsion at Delft University of Technology

Tarık Hartuç

March 11, 2015

Faculty of Aerospace Engineering · Delft University of Technology

Abstract

In this thesis both Wake Ingestion (WI) and Boundary Layer Ingestion (BLI) configurations have been investigated and analyzed with respect to their application to aircraft design. WI and BLI in the context used here means positioning the engine such that it ingests boundary layer fluid for the purpose of saving shaft-power.

This research compares propulsors in free-stream, WI and BLI configurations for their shaft-power savings. The power elements present in these configurations are identified theoretically using the Power Balance Method (PBM) and quantified experimentally by using Particle Image Velocimetry (PIV). Also, these different configurations are compared using non-dimensional parameters such as thrust-power coefficient and propeller efficiency. This is accomplished by integrating different instruments able to capture the relevant physical phenomena such as thrust, torque and Rotations Per Minute (RPM). These measurements are conducted in the low-speed wind-tunnel facility of Delft University of Technology. The aim is to experimentally quantify the increase in propeller efficiency for WI and BLI configurations. In order to properly compare the three configurations, these are tested in two different wind-tunnel conditions; 'equilibrium' and 'constant-speed'. In the equilibrium case, propulsor thrust is set identical to body drag for varying wind-speeds whereas the constant-speed case requires the wind-speed to be fixed and propulsor thrust to vary.

The main finding is that a propulsor in WI configuration saves 9% shaft-power w.r.t. an identical propulsor in free-stream configuration under identical net-force conditions. This power saving is more prominently present in BLI configuration where 18% power saving is measured. This measured power saving is due to the fact that the propulsor is immersed in the slower moving wake. The propulsive efficiency, which is different from propeller efficiency, can generate values that exceed 100% in WI and BLI configurations. Therefore, a different definition of efficiency for a wake ingested propulsor is introduced. Using this new definition, the propulsive efficiency does not exceed unity for perfect wake filling configurations.
The PIV analysis on the identified power terms shows that a limited amount of wake power is available for performance enhancement. The analysis also showed that pressure plays a significant role in these tightly integrated configurations which cannot be ignored.

This insight can be used for the development of WI and BLI applications. These applications are needed as a mean to reduce fuel consumption for future aircraft.

Table of Contents

List of Figures

List of Tables

Preface

This thesis is the final requirement for my Master of Science in Aerospace Engineering. I already gained some experience with experimental studies during my internship at Mitsubishi Equipment Europe where I validated CFD results for turbocharger applications. I found it such exhilarating that it changed my educational interests from theory to more experimental. I expressed my interests to Dr. Arvind Rao who graciously honored my request by providing this experimental thesis.

Acknowledgements

First and foremost I would like to thank my supervisor Dr. A. Rao for choosing this thesis for me as well as assisting me by providing me valuable feedback after meetings. I sincerely appreciate the invaluable academic and personal support I received from him throughout this thesis.

I would also like to thank my tutor PhD candidate L. Peijian for his leading role during my thesis in understanding BLI theory as well as the preparation for the experiment. I had fun during the weekly meetings in which we exchanged ideas about various topics. I am honored to be part of his PhD research.

The tremendous help I received from Dr. D. Ragni in setting up the experiment and the clear discussions carried out is extremely appreciated. I choose the word 'clear' deliberately because my experience with meetings and discussions is that usually more questions rise than answers are received.

I also respectfully acknowledge Prof. L. Veldhuis, busy as he is, to guide me and provide intellectual tips for the preparation and planning of the wind-tunnel experiment.

I simply enjoyed the discussions triggered by Prof. G. Eitelberg, the way he ambushed Peijian with his fierce arguments, so thank you for that!

Usually forgotten or not appreciated, but hereby I would like to thank the whole staff of the windtunnel; P.J. Duyndam, W.A. Timmer, N. van Beek, L. Molenwijk, H. Siemer, S. Bernardy, F.J. Donker Duyvis.

Finally, my gratitude goes to my (pregnant!) wife Selin. Seni Seviyorum.

Delft, University of Technology — Tarık Hartuç
March 11, 2015

"Not all theories are solid, not all fluids are liquid." — *Tarık Hartuç*

Chapter 1

Introduction

1-1 Motivation

Throughout aircraft history lowering fuel consumption has been a major requirement (see Fig. 1-1). This requirement has its origins in operational cost savings for airliners. It became even more important after the Middle East oil crisis in 1973 in which the volatile price of oil roof-topped. After this crisis National Aeronautics and Space Administration (NASA) developed a new generation of high-speed propellers for commercial aircraft that demonstrated the potential to reduce passenger aircraft fuel consumption. Different projects were set up which eventually led to the development of the fuel efficient General Electric (GE) 90 jet engine.[14] Technological developments to increase flight efficiency aimed at developing fuel efficient engines and adapting aerodynamic external design of aircraft components. But studies such as Smith (1991) and McLemore Clyde (1962) suggest that ingesting the Boundary Layer (BL) in the engine is another method to increase propulsive efficiency. This rather unconventional method has been investigated by many scientists using different approaches.

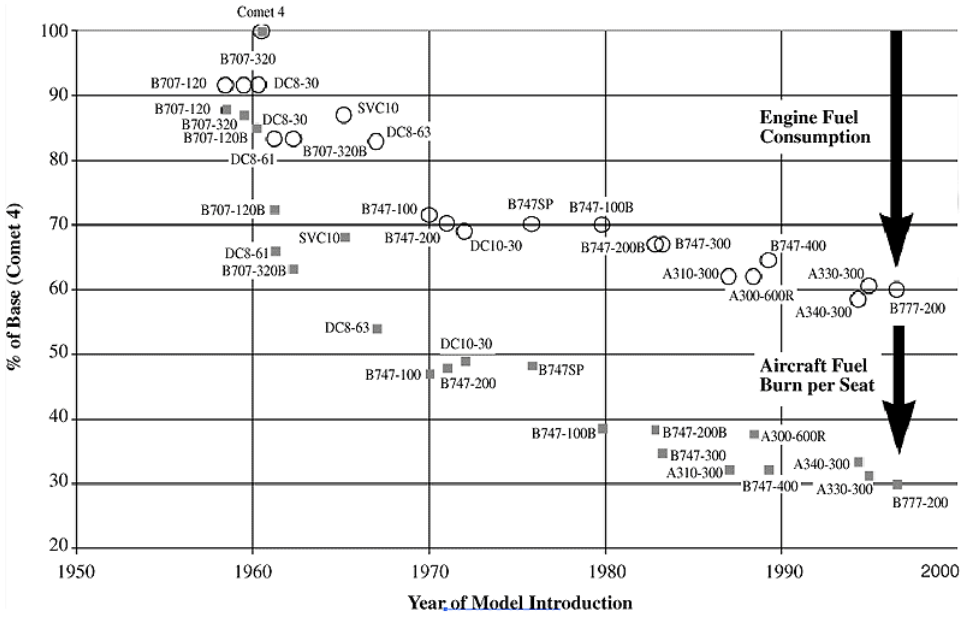

Figure 1-1: Trend in Transport Aircraft Fuel Consumption[6]

Only recently the actual process and individual energy elements involved in Boundary Layer Ingestion (BLI) is defined in Drela (2009). Drela (2009) focuses on capturing all energy elements present in BLI. This theoretical study is extended in Peijian and G. Rao (2013) to a degree in which the energy elements are balanced inside an analytical expression which is quantifiable. This analytical expression is able to link BLI immersed propulsor thrust with other involved energy terms which can provide more understanding in BLI phenomena. The reason why the elements in this expression need experimental quantification is because the knowledge gained from these power elements can be helpful in the decision-making process for fuel efficient BLI transport- or military aircraft in the future.

1-2 Research Question

"To which degree is a propulsor in Wake Ingestion (WI) and Boundary Layer Ingestion (BLI) configuration different in terms of propeller efficiency and what are the limitations of the propulsive efficiency when dealing with these configurations?"

"What is the inter-relation between the power terms, defined using Power Balance Method (PBM), for Wake Ingestion (WI) and Boundary Layer Ingestion (BLI) configurations?"

1-3 Thesis Overview

This report is roughly divided in two parts: Theory (Part I) and Experiment (Part II).
In Part I, the theory behind BLI is treated (Ch. 2) where also the PBM is introduced. In Chapter 3 the PBM is treated in detail which encapsulates the analysis and identification of different power terms present for WI and BLI configurations. Chapter 4 deals with the limitations and interpretation of Froude's propulsive efficiency when dealing with these tightly integrated configurations. Chapter 5 finalizes Part I by introducing the theory behind Particle Image Velocimetry (PIV) which is used for the experiment.

Part II treats the conducted experiment. The experimental setup and implementation can be found in Chapter 6 and 7 respectively. The processing of the quantitative data obtained from the wind-tunnel experiment is treated in Chapter 8. The processed results of the experiment can be found in Chapter 9. This thesis finalizes with the conclusions and recommendations for further studies in Chapter 10.

1-4 Contributions

The contributions of this thesis are:

1. Quantification of the benefits of BLI and WI using wind-tunnel experimentation.
2. Quantification of the power terms, defined using PBM, using PIV.
3. Provide limitations and possible adaptations for the propulsive efficiency.

Part I

Theory

Chapter 2

Boundary Layer Ingestion

In this chapter the theoretical background on Boundary Layer Ingestion (BLI) is treated in detail. The concept and difficulties regarding this technique are highlighted first in Section 2-1. This is followed by summarizing earlier works on BLI in Section 2-2. Finally, the Power Balance Method (PBM) introduced by Drela is explained in Section 2-3.

2-1 Introduction to BLI

Boundary Layer Ingestion is, as the name suggests, the ingestion of the Boundary Layer (BL) in an (aircraft) engine. The same definition holds for Wake Ingestion (WI) where the slower moving wake, caused by a body (fuselage) in front, is ingested in the (aircraft) engine. The moving stream of fluid rubs against a solid body which is slowed down by friction causing drag. This slower moving thin stream of fluid is called a BL. The velocity profile of a BL for a thin plate can be found in Fig. 3-7. The BL has a velocity profile and thickness different from free-stream flow which can cause engine inlet flow distortion. In conventional aircrafts the nacelles are always placed to be free of BL caused by the wing and fuselage since the engine cannot tolerate this flow distortion. In Fig. 2-1 the axial velocity profile over an engine with inlet flow distortion can be found. The consequences of an engine operating in a pressure distorted inflow include performance degradation, vibration due to unsteady blade forces and stall margin reduction which can lead to surge. Surge is a large-scale event involving flow reversal through the entire engine. Surge causes engine flame out and power loss. Thus it is of paramount importance to reduce flow distortion for BLI applications.

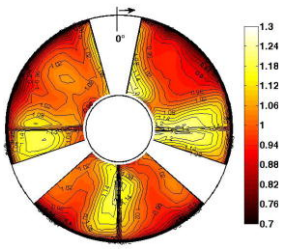

Figure 2-1: Engine Inlet Distortion: Axial Velocity ($^{V}/_{V_{mean}}$) Distribution[13]

There are a couple of flow control methods available to reduce flow distortion. Flow control involves passive or active devices. Passive methods modify a flow without applying energy to the system such as geometric shaping (manipulate the pressure gradient) and vortex generators (separation control). Active Flow Control (AFC) methods modify a flow by adding energy into the flow.[16] Recently National Aeronautics and Space Administration (NASA) conducted experiments in which AFC was proven to reduce distortion from 29% to the acceptable value of 4.6% by using less than 1% of inlet mass-flow.[10] Thus flow distortion is no more a limitation which enables the possibility of using BLI applications in the future. But why use BLI?

2-2 Earlier BLI Studies

The adverse effects of Airframe Propulsion Interaction (API) due to improper propulsor installation could cause extra drag increase or aerodynamic performance distortion such as engine inlet flow distortion treated in the previous section (Sec. 2-1). Nevertheless this interaction effect could also be utilized favorably by WI and BLI. There are many studies on BLI that focused on different aspects such as noise reduction, weight savings, increasing maximum speed and increasing fuel efficiency. The most prominent and clear result of these studies is the increase in propulsive efficiency. Increasing propulsive efficiency by using the slower moving wake or BL has long been known in the field of marine propulsion. Wislicenus and Smith (1952), Wislicenus (1960), Gearhart and Henderson (1966) and Bruce et al. (1974) which are cited in Smith (1991) conducted design studies of propulsors employing WI aimed at the propulsion of submerged bodies such as torpedoes. For aircraft propulsion, BLI and WI appears less beneficial since the wake is spread more by the wings and due to the reduced density and total pressure properties of air compared to water.[26] The increase in efficiency due to BLI was theoretically known for many years because the derivation for it is fairly simple by comparing two cases: BLI propulsor versus free-stream propulsor (see Fig. 2-2).

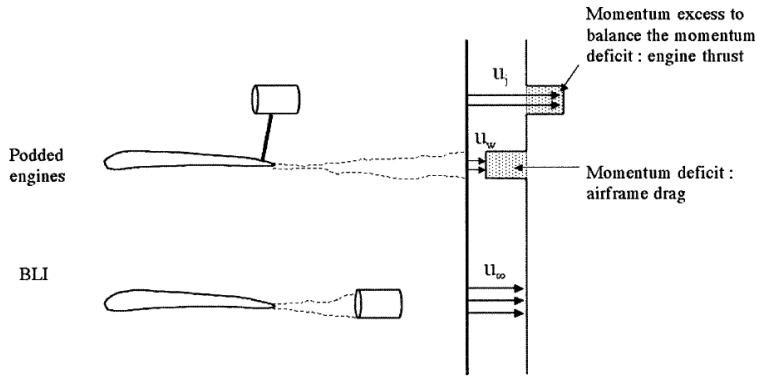

Figure 2-2: The Benefits of BLI: Freestream and 100% BLI Propulsor Case[23]

Observing Figure 2-2 it can be seen that for the free-stream propulsor, like a turbofan in a wing-mounted nacelle, the excess Kinetic Energy (K.E.) generated by the jet is wasted. But when the propulsor is immersed in the slower-moving boundary-layer flow there is no excess K.E., and less energy needs to be added to achieve the same thrust.[23] It might be argued that it is not only the reduction of excess K.E. but the more favorable configuration in terms of drag that is the source of benefit.

One of the first studies about the benefits of BLI for aircraft propulsion was carried out by Smith (1947) which showed that an engine which ingests BL can reduce cruising fuel consumption by 10%. He conducted experiments which resulted in the conclusion that BL ingesting engines reduced fuel consumption by 32% compared to a turbojet engine propelling the same configuration.[23]

NASA conducted wind-tunnel tests of a 1/20-scale airship model with stern propellers (wake propellers) the results of which can be found in McLemore Clyde (1962). The research included tests in different wake characteristics which showed that *stern-mounted propeller can give a much higher propulsive efficiency than that of a conventional-mounted or a fin-mounted-propeller installation.*[17]

Betz (1966), cited in Plas (2006), analyzed a fully wake ingested propeller at ambient static pressure. He concluded that the required power of the wake ingested propeller is reduced because the engine uses wake energy that is left in the wake which reduces the excess energy in propeller slipstream.

Betz (1966), cited in Smith (1991), explains that with WI, the power expended can actually be less than the product of the forward speed and aircraft drag which is later called the drag-power in Drela (2009) and Peijian and G. Rao (2013).

Douglass (1970), cited in Plas (2006), carried out a study in which BL ingesting and non-ingesting case were compared by means of keeping the relative velocity increment given by the engine to the flight speed constant. He found that BLI is beneficial because the K.E. of both the wake and jet is reduced. Douglass calculated that a maximum propulsive efficiency of 16% is possible assuming no losses in the engine inlet.

Smith (1991) developed a method for estimating the amount of propulsive power that can be saved when the viscous wake of a body is used as part of the propulsive fluid. This propulsive power is represented by the axial K.E. flux in the downstream wake. He concluded that power saving with wake ingestion is largest for small propulsors with high thrust-loading coefficients. Smith also found that power saving is largest when the propulsor is positioned such that the wake has no time to be flattened by the fluid shear stresses. For the "wake ingestion ideal case" in which 100% of the wake is ingested, he found that the benefits can be up to 7%.

NASA also conducted a research in 2006 under the Ultra Efficient Technology Program Propulsion Airframe Integration Project in which the potential propulsion airframe integration improvements using BLI inlets with AFC were investigated. The analysis was performed on a Blended Wing Body (BWB) aircraft with turbofan engines mounted atop the aft end of the aircraft. *The greatest potential benefit of up to a 10% reduction in fuel burned was identified as potentially achievable if AFC can be used for boundary layer control to enable a short offset BLI inlet.*[15]

In many of the previous works on BLI the focus was mainly on momentum-equation analysis, giving relations for the aerodynamic lift and drag forces. Drela (2009) has focused on mechanical power and K.E. flow for the control volume analysis of the compressible viscous flow. This approach, according to Drela, *does not require any separate definitions of thrust and drag, and hence it is especially useful for analysis and optimization of aerodynamic configurations which have tightly integrated propulsion and boundary layer control systems.* Drela defined a control volume analysis of the flow about an aircraft focusing on mechanical energy which is called the Power Balance Method (PBM). The results using PBM is a rela-

tion between all the power sources and sinks in a flow-field, in which the quantities which directly influence flight power requirements are identified and are consistent with previous analyses based on momentum.

Hardin et al. (2012) carried out a study in which fuel burn benefits associated with BLI for generation-after-next (N+2) aircraft and propulsion system concepts are identified. Results of the study showed that a 3-5% BLI fuel burn benefit can be achieved for N+2 aircraft relative to baseline high-performance, pylon mounted ultra high bypass propulsion system.

Recently a study is published in Uranga et al. (2014) on the BLI benefit for D8 aircraft which has a Blended Wing Body (BWB) configuration. In this study wind-tunnel experiments are performed using two powered 1:11 scale, 13.4 ft span models, in BLI and non-BLI versions. The tests are conducted at the NASA Langley Subsonic Wind Tunnel. The comparison is made using the propulsor power required to produce a given net stream-wise force on the entire aircraft. The experiment showed that BLI propulsors require 6% less electrical power at the simulated cruise point. It must be noted that this BLI benefit is directly measured raw data since it is defined in terms of electrical power. But the study predicts that this benefit conversed in terms of flow power will remain essentially the same.

It can be seen from the above that all studies agree upon the fact that BLI increases the propulsive efficiency. The magnitude however is quite dispersed. This is acceptable when considering experimental results. But what is striking is the fact that also at theoretical level the BLI benefit is not agreed upon. This is due to a lack of general accepted control volume which describes and quantifies each aspect of the BLI phenomenon. Each individual study defines its own control volume, boundaries and assumptions to generate the BLI benefit compared to a non-BLI model which is also bound by certain predefined assumptions. In order to use BLI in the future it is important to understand and quantify the core elements that cause this increase in propulsive efficiency. Only this way it is possible to really understand the fundamentals behind BLI. This is exactly the goal of this thesis, to understand and quantify the core elements behind the propulsive efficiency increasing phenomenon of BLI. An attempt is made to experimentally quantify these elements to understand its significance.

2-3 Power Balance Method

The power elements that require quantification is based on the PBM developed in Drela (2009). This is the reason why the work of Drela is treated first as a strong and firm introduction for Chaper 3.

The latest method introduced by Drela captures many, if not all, elements in BLI phenomenon. According to Drela, decomposition of complex BLI cases is ambiguous using thrust and drag definitions which is always the case in momentum analysis (see Appendix A for further details regarding momentum analysis). Therefore he proposes to use mechanical energy analysis instead. Using this analysis he identifies all dissipation sources illustrated in Fig. 2-3. He then defines and decomposes the total mechanical wake energy outflow. The total mechanical wake energy outflow is decomposed in multiple components. The result of this is a power balance equation stated in Eqn. 2-1. Note that the left-hand side is the energy which flows in the Control Volume (CV) and the right-hand side represents the energy outflow. What follows now is the interpretation of each parameter in Eqn. 2-1.

$$P_s + P_v + P_k = W\dot{h} + \dot{E}_a + \dot{E}_v + \dot{E}_p + \dot{E}_w + \Phi \tag{2-1}$$

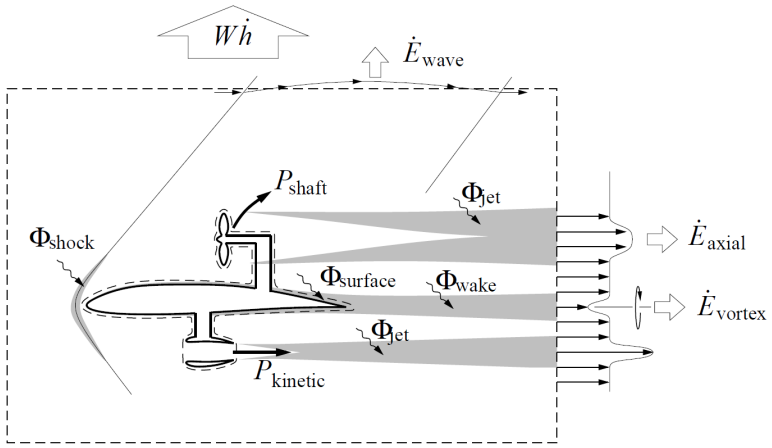

Figure 2-3: 2D cutaway of 3D CV Surrounding an Aerodynamic Body[9]

P_{shaft} or (P_s), net propulsor shaft-power. This is the integrated force times velocity on all moving body surfaces.
P_v, net pressure-volume power. This is a volumetric mechanical power, provided by the fluid expanding against atmospheric pressure.
P_k, net propulsor mechanical energy flow rate into the CV. This is the net pressure-work and K.E. flow rate into the CV.
$W\dot{h}$, potential energy rate. This is the power consumption needed to increase the aircraft's potential energy. However this term becomes an energy source during descent.
$\dot{E}_{\text{axial}}$ or ($\dot{E}_a$), wake streamwise (axial) K.E. deposition rate. This is the rate of stream wise K.E. being deposited in the flow out of the CV, through the Trefftz plane.
$\dot{E}_{\text{vortex}}$ or ($\dot{E}_v$), wake transverse (vortex) K.E. deposition rate.
$\dot{E}_p$, wake pressure-defect work rate. This is the rate of pressure work done on the fluid crossing the Trefftz plane at some pressure different from ambient pressure.
$\dot{E}_{\text{wave}}$ or ($\dot{E}_w$), wave (lateral) pressure-work and K.E. outflow rate. This is the pressure work rate and K.E. deposition rate of the fluid crossing the side cylinder.
Φ, viscous dissipation rate. This measures the rate at which K.E. of the flow is converted into heat inside the CV.

Equation 2-1 is applicable for 3D wings, this can be clearly seen by the vortex contribution. This PBM can be applied to simpler cases to understand the benefit of BLI in energy quantity terms. This is performed by Peijian in the next section to identify the power terms present for different configurations.

Chapter 3

Defining the Power Terms

The Power Balance Method (PBM) introduced by Drela is used by Peijian to investigate Wake Ingestion (WI) and Boundary Layer Ingestion (BLI) phenomena. Using this PBM for WI and BLI Peijian derived an analytical expression. This expression, derived using the Control Volume (CV) in Fig. 3-2, expressed in Eqn. 3-19, is particularly useful in capturing all the relevant elements involved in BLI or WI. The trail of thought in the derivation of this expression stems from analyzing three cases consecutively:

1. Free-stream Propulsor
2. Ideal BLI Propulsor
3. General BLI Propulsor

Peijian compares these different cases using the propulsive efficiency which can be found in Eqn. 3-1. Where the total power in the denominator equals the kinetic energy addition of the propulsor. There exists a difference between propeller efficiency and propulsive efficiency in the sense that the propeller efficiency uses shaft-power in the denominator. The definition for the propeller efficiency can be found in Eqn. 3-2. Here Tor and RPS correspond to torque and rotations per second of the propeller respectively. The difference between both definitions lies in heat, pressure and other viscous losses which are ignored in Eqn. 3-1. For BLI and WI configurations it seems that the propulsive efficiency can exceed 100% which will be seen in Sec. 3-2. Such efficiencies, when referring to BLI or WI, seem to be violating energy conservation laws. The common efficiency definition cannot be used anymore, because the assumptions for its derivation are broken. The possible reasons and further discussion regarding this topic is introduced in this chapter and further treated in Chapter 4.

$$\eta_{propulsive} = \frac{TV_\infty}{P_{total}} = \frac{TV_\infty}{\frac{1}{2}\dot{m}u_{out}^2 - \frac{1}{2}\dot{m}u_{in}^2} \tag{3-1}$$

$$\eta_{propeller} = \frac{TV_\infty}{P_{shaft}} = \frac{TV_\infty}{2\pi \times Tor \times RPS} \tag{3-2}$$

In this chapter, initially the aforementioned three cases are analyzed by applying PBM in Sec. 3-1, 3-2 and 3-3. This is followed by a discussion about the body wake flow (Sec. 3-4) which is an important factor that appears when applying PBM for these cases. In Section 3-5 the propulsor and body are integrated in a single CV in WI configuration. Finally, in Sec. 3-6 the interaction effects between body and propulsor for tightly integrated BLI configurations is treated.

3-1 Free-stream propulsor

Observing Fig. 3-1(a) it can be seen that a 2D classical actuator disc is assumed for the propulsor. A CV encapsulates this propulsor with a Trefftz Plane (TP) as outlet plane. Notice that free-stream velocity (V_∞) flows in the actuator disc and is accelerated to outlet velocity (u) deposited on the TP. Similarly a CV is established to contain the surrounding fluid enclosed by stream surface, the inlet and outlet plane with pressure identical to ambient pressure.
The Kinetic Energy (K.E.) production rate ($\dot{E}_{\text{K.E.}}$) is the only power input. According to Peijian, this momentum excess balances an ideal force opposite to the flow direction which is virtually doing work at the flight speed, called thrust-power (TV_∞). The thrust-power, provided in Eqn. 3-4, is considered as the energy output term. Since there exists a velocity (u) higher than free-stream (V_∞) at TP, there exists a momentum excess. This is captured by the second output term, wake K.E. outflow flux ($\dot{E}_{\text{prop,wake}}$), which dissipates completely downstream outside the CV (Eqn. 3-5).

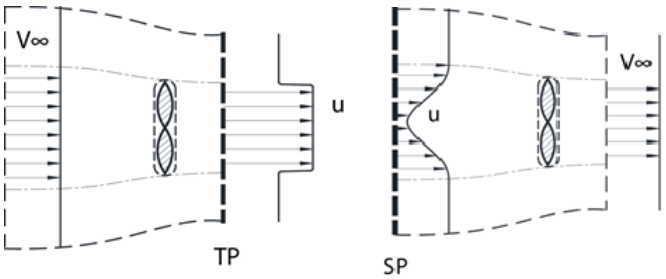

(a) Free-stream Propulsor (b) Ideal BLI Propulsor

Figure 3-1: Controlvolume with Propulsor for Two Configurations[19]

$$\dot{E}_{\text{input}} = \dot{E}_{\text{K.E.}} = \iint_{TP} \rho u \tfrac{1}{2}(u^2 - V_\infty^2) dS \tag{3-3}$$

$$\dot{E}_{\text{output-1}} = TV_\infty = \iint_{\text{TP}} \rho u V_\infty (u - V_\infty) dS \tag{3-4}$$

$$\dot{E}_{\text{output-2}} = \dot{E}_{\text{prop,wake}} = \iint_{\text{TP}} \rho u \tfrac{1}{2}(u - V_\infty)^2 dS \tag{3-5}$$

Adding Eqns. 3-4 and 3-5 gives the total energy output flux given in Eqn. 3-6. By subtracting all output terms (Eqn. 3-6) from the power input (Eqn. 3-3), the power balance equation for this free-stream actuator can be written (Eqn. 3-8). These terms need to be equal, otherwise the mass conservation law for the CV is violated. This can simply be checked by taking the efficiency of the CV (Eqn. 3-9) which needs to equal 1 at all times.

The useful output energy flux equals the thrust-power since the other output energy source (wake K.E.) is wasted and thus unused. Dividing the useful output flux by the total input gives the propulsive efficiency (see Eqn. 3-10). Since the wake K.E. outflow ($\dot{E}_{\text{prop,wake}}$) is always positive, it can be concluded that for the free-stream propulsor case, the propulsive efficiency is always smaller than 1.

$$\dot{E}_{\text{total output}} = TV_\infty + \dot{E}_{\text{prop,wake}} = \int_{\text{tp}} \rho u \tfrac{1}{2}(u^2 - V_\infty^2) dA \tag{3-6}$$

$$\dot{E}_{\text{total input}} = \dot{E}_{\text{K.E.}} = \int_{\text{tp}} \rho u \tfrac{1}{2}(u^2 - V_\infty^2) dA \tag{3-7}$$

$$\dot{E}_{\text{K.E.}} = TV_\infty + \dot{E}_{\text{prop,wake}} \tag{3-8}$$

$$\eta_{\text{total}} = \frac{\dot{E}_{\text{total output}}}{\dot{E}_{\text{total input}}} = 1 \tag{3-9}$$

$$\eta_{\text{propulsive,free}} = \frac{TV_\infty}{\dot{E}_{\text{K.E.}}} = \frac{TV_\infty}{TV_\infty + \dot{E}_{\text{prop,wake}}} < 1 \tag{3-10}$$

3-2 Ideal BLI propulsor

In the ideal BLI case the propulsor is immersed in the slower moving wake. In this case it is assumed that the propulsor restores the slower moving wake to the initial undisturbed velocity of the propulsor (See Fig. 3-1(b)). Thus there is no body or propulsor wake flux left in the downstream flow (after the propulsor). A CV is built in an identical approach as before, with boundary pressure identical to ambient value. In order to capture the inflow velocity profile at the inlet plane, a Survey Plane (SP) is set to coincide with the inlet plane. For this case it is important to note that the body wake flux (defined in Eqn. 3-11) present at SP originates from a body which is not illustrated inside Fig. 3-1(b).

A similar approach can be applied to define the power balance for this ideal wake filling actuator. For this case however there exists two power input terms (body wake K.E. inflow and K.E. production rate) instead of one. Before defining these input power terms it should be noted that free-stream velocity (V_∞) is always larger than wake velocity (u). Although the approach is the same, there exists radical differences w.r.t. the freestream case.

The body wake flux ($\dot{E}_{\text{body,wake}}$) is an energy input source, caused by the presence of a body in front of the SP, defined in Eqn. 3-11. Similar to the previous case, the K.E. flux deposition rate ($\dot{E}_{\text{K.E.}}$) can be calculated. This is shown in Eqn. 3-12. The total energy input flux can be found in Eqn. 3-13. Because there is no wake flow out of the CV, the thrust-power is the only energy output term which can be found in Eqn. 3-14. Since the power terms are identified, the power balance equation for this ideal BLI actuator can be written (see Eqn. 3-15). These terms need to be equal which can again simply be checked by taking the efficiency of the CV (Eqn. 3-9) which needs to equal 1 at all times.

When calculating the propulsive efficiency for this case, Eqn. 3-16 arises. Note the denominator which represents the actual energy flux used by the propulsor as input. The efficiency is expected to be larger w.r.t the free-stream case due to BLI effect but what is

striking is the fact that the efficiency exceeds 1. It seems that there goes more energy out than there flows in, energy creation. This of course can not be true since it does not obey the energy conservation law. This is the main reason why the propulsive efficiency is a figure of merit and cannot be interpreted in terms of efficiency in the classical sense for BLI applications. A discussion about the propulsive efficiency is provided in Chapter 4.

$$\dot{E}_{\text{input-1}} = \dot{E}_{\text{body,wake}} = \iint_{\text{SP}} \rho u \tfrac{1}{2}(u - V_\infty)^2 dS \tag{3-11}$$

$$\dot{E}_{\text{input-2}} = \dot{E}_{\text{K.E.}} = \iint_{SP} \rho u \tfrac{1}{2}(V_\infty^2 - u^2) dS \tag{3-12}$$

$$\dot{E}_{\text{total input}} = \dot{E}_{\text{body,wake}} + \dot{E}_{\text{K.E.}} = \iint_{\text{SP}} \rho u (V_\infty^2 - V_\infty u) dS \tag{3-13}$$

$$\dot{E}_{\text{total output}} = TV_\infty = \iint_{\text{SP}} \rho u V_\infty (V_\infty - u) dS \tag{3-14}$$

$$\dot{E}_{\text{body,wake}} + \dot{E}_{\text{K.E.}} = TV_\infty \tag{3-15}$$

$$\eta_{\text{prop,bli}} = \frac{TV_\infty}{\dot{E}_{\text{K.E.}}} = \frac{\dot{E}_{\text{body,wake}} + \dot{E}_{\text{K.E.}}}{\dot{E}_{\text{K.E.}}} > 1 \tag{3-16}$$

3-3 General BLI Propulsor

Peijian found for the ideal BLI propulsor case, illustrated in Figure 3-1(b), that the propulsive efficiency can be larger than one. This theoretical prediction moved him to conduct a quick experiment to see whether the propulsive increasing effect of BLI can be measured and if so to which degree. He measured a propeller efficiency peak value for free-stream propulsor of 48% while the peak value for BLI is 63% at similar condition, meaning that the theoretical prediction that BLI increases efficiency performance is satisfied. But values higher than 100% looks highly unlikely. During this experiment it was realized by Peijian that only perfect conditions could set the stage for a measurement of efficiency larger than 100%. But since the propeller was an off-the-shelf product it was highly unlikely to get these measurements. This is because the propeller is supposed to be an ideal wake-filling instrument which requires fine-tuning and custom design. From post-processing it is concluded that the uncertainties from his experiment are too large to provide confident conclusions. In order to increase accuracy, the experiment needed to be upgraded to larger dimensions. He also concluded that, in his experiment, the propeller did not fill in the wake ideally which is the main assumption for the ideal BLI case. So he continued to define a general BLI propulsor case in which the assumptions are more relaxed.
The main difference between the ideal and general BLI case is the fact that the propulsor in the general case does not need to fill in the wake perfectly but can also advance free-stream air, shown in Fig. 3-2. A similar CV is constructed to contain the fluid around the surface of actuator, while the external boundary of CV is closed by the stream surface, as well as the inlet and outlet plane perpendicular to V_∞ (see the dashed line). The external boundary is again chosen sufficiently far where pressure is identical to the ambient pressure, leaving no pressure force nor pressure power terms to be involved. With the finite size CV, the internal viscous dissipation is simply ignored.

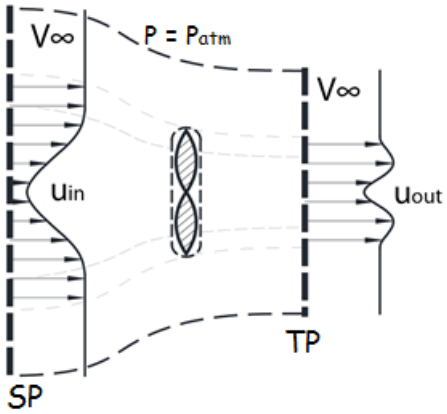

Figure 3-2: Control-volume for Wake-Ingested Propulsor with Corresponding Velocity, Energy and Force Terms[19]

For the CV, inlet is set to coincide with a SP where the free-stream and body wake combined flow come into the CV. After being advanced by the actuator (propeller), the flow leaves the CV crossing the TP. Note that the TP is by definition downstream of the object while SP is a plane upstream the actuator. Continuity equation of this CV should be satisfied (Eqn. 3-17) while momentum gives the thrust generated by the actuator (Eqn. 3-18).

$$\iint_{SP} \rho u_{\text{in}} dS - \iint_{TP} \rho u_{\text{out}} dS = 0 \tag{3-17}$$

$$T = \iint_{TP} \rho u_{\text{out}}^2 dS - \iint_{SP} \rho u_{\text{in}}^2 dS \tag{3-18}$$

Applying PBM for this CV depicted in Fig. 3-2, leads to Eqn. 3-19. This expression is derived according to the same analogy, computing K.E. energy in and out of the CV using PBM. The expression (Eqn. 3-19) simply states that the fresh K.E. deposited on the Trefftz plane ($\dot{E}_{\text{body,wake}}$) plus the K.E. deposited by the propulsor ($\dot{E}_{\text{K.E.}}$) equals the thrust-power (TV_∞) plus the propulsor wake K.E. out flux ($\dot{E}_{\text{propulsor,wake}}$). These individual terms are provided in Eqns. 3-20, 3-21, 3-22 and 3-23 respectively.

$$\dot{E}_{\text{body,wake}} + \dot{E}_{\text{K.E.}} = TV_\infty + \dot{E}_{\text{propulsor,wake}} \tag{3-19}$$

$$\dot{E}_{\text{body,wake}} = \iint_{\text{SP}} \rho u_{\text{in}} \tfrac{1}{2} (u_{\text{in}} - V_\infty)^2 dS \tag{3-20}$$

$$\dot{E}_{\text{K.E.}} = \iint_{TP} \rho u_{\text{out}} \tfrac{1}{2} u_{\text{out}}^2 dS - \iint_{SP} \rho u_{\text{in}} \tfrac{1}{2} u_{\text{in}}^2 dS \tag{3-21}$$

$$TV_\infty = \iint_{TP} \rho u_{\text{out}}^2 V_\infty dS - \iint_{SP} \rho u_{\text{in}}^2 V_\infty dS \tag{3-22}$$

$$\dot{E}_{\text{propulsor,wake}} = \iint_{TP} \rho u_{\text{out}} \tfrac{1}{2} (u_{\text{out}} - V_\infty)^2 dS \tag{3-23}$$

$$\eta_{\text{prop,general}} = \frac{TV_\infty}{\dot{E}_{\text{K.E.}}} = \frac{TV_\infty}{TV_\infty + \dot{E}_{\text{propulsor,wake}} - \dot{E}_{\text{body,wake}}} = \frac{1}{1 + \frac{\dot{E}_{\text{propulsor,wake}} - \dot{E}_{\text{body,wake}}}{TV_\infty}} \tag{3-24}$$

The propulsive efficiency for this general case is provided in Eqn. 3-24. This expression simply shows that utilizing the body wake ($\dot{E}_{\text{body,wake}}$) and saving of the downstream propulsor wake ($\dot{E}_{\text{propulsor,wake}}$) provides the benefit in terms of efficiency. Here it can be seen that the propulsive efficiency exceeds 100% for perfect wake filling cases where the propulsor wake term ($\dot{E}_{\text{propulsor,wake}}$) is zero.

In order to use this benefit the actuator (propeller) needs to be integrated at the position where the body wake K.E. flow ($\dot{E}_{\text{body,wake}}$) can be used as a power source. In order to accomplish this, it would also be sensible to capture the body wake as early as possible, when its value is the largest. The airframe tail is such a place where the flow is reduced and concentrated in the form of a Boundary Layer (BL) or slower moving wake flow. When observing Eqn. 3-16, it can be seen that the efficiency is dependent on the inter-relation between the body wake ($\dot{E}_{\text{body,wake}}$) and the K.E. production rate ($\dot{E}_{\text{K.E.}}$). If these two terms are equal in quantity, the efficiency increases to 200%. However if the K.E. production rate is always 10 times larger than the body wake term, the maximum efficiency simply stagnates at 10%. This is the reason why it is very important to quantify these terms experimentally.

The propulsive efficiency increasing phenomenon is related to the fact that same thrust can be produced with less momentum excess ($u_{\text{out}} - V_\infty$) in the propulsor wake. Meaning that if the wasted wake K.E. flow ($\dot{E}_{\text{propulsor,wake}}$) is lowered while keeping the same thrust-power (TV_∞) and using the body wake ($\dot{E}_{\text{body,wake}}$) as a power source, the power input ($\dot{E}_{\text{K.E.}}$) for the actuator reduces substantially w.r.t. the conventional free-stream propulsion. For the actuator, it is beneficial to capture as much body wake flow as possible because increasing this term in Eqn. 3-19 reduces the K.E. production rate ($\dot{E}_{\text{K.E.}}$) of the propeller (assuming the other terms to stay constant). In the above discussion, K.E. conservation is satisfied for the CV which only contains an isolated actuator. However, when only considering the discussion above, increasing the propulsive efficiency seems fairly simple. Increase the body wake K.E. ($\dot{E}_{\text{body,wake}}$) and decrease the propulsor wake ($\dot{E}_{\text{propulsor,wake}}$) as much as possible. This however is erroneous, especially increasing the body wake term. The body wake as the resultant after an airframe is therefore further discussed in the next section.

3-4 Body Wake Flow

Body wake flow is caused by the presence of a body changing flow properties at the TP (See Fig. 3-3). A CV is built to contain the fluid around a 2D isolated airframe that only experiences profile drag, as shown in Fig. 3-3. The external (top and bottom) boundary is closed by stream surfaces where ambient pressure is imposed. The TP is chosen close enough to the body tail, where the BL flow just leaves the airframe surface. Similar to the previous actuator cases, PBM can be applied to this isolated 2D airfoil inside a CV. Drela applied this for the CV illustrated in Fig. 3-3 where he concluded that "the total dissipation in this case is simply equal to the drag-power DV_∞". The total dissipation in this 2D airfoil case is the summation of viscous BL dissipation and energy dissipated in the wake.[9]

The airframe profile drag is the component of total aerodynamic force parallel to the free-stream by integrating both the pressure and viscous contribution over the entire body surface. It is identical to the momentum flow defect measured at the TP (See Eqn. 3-25), according to

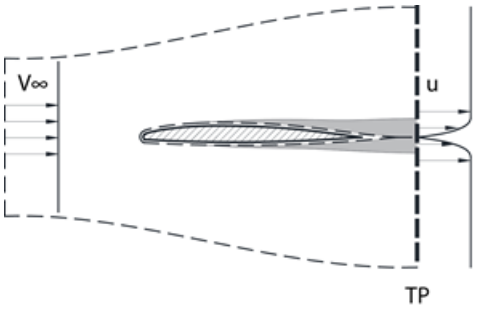

Figure 3-3: Control Volume for the Isolated Airframe[19]

the momentum equation (Eqn. A-1). For an extensive derivation of the profile drag, reference is made to Appendix A. In order to maintain this airframe in its free flight condition, a thrust force (T) which doesn't intrude the flow field should oppose and balance the profile body drag (D). In accordance with the airframe, this force also moves at V_∞ when observed in ground reference. Consequently, the amount of thrust-power involved (TV_∞) is simply identical to the drag-power (DV_∞) and it is considered as the power input term for the CV (Eqn. 3-26).

$$D = \iint_{TP} \rho u(V_\infty - u)dS \tag{3-25}$$

$$DV_\infty = TV_\infty = V_\infty \iint_{TP} \rho u(V_\infty - u)dS \tag{3-26}$$

As for power output terms, the first one is the K.E. loss rate of the CV, quantified as the deficit from the fresh free-stream kinetic energy to the kinetic energy flow measured at TP (See Eqn. 3-27). For the prescribed CV where TP is close to the body tail, this K.E. loss roughly equals the viscous dissipation inside BL (shade region). The second output term is the infamous body wake K.E. outflow (Eqn. 3-28). This term, as discussed in the wake system, flows out of this finite sized CV and would be eventually dissipated in the far field if not utilized. But if utilized, it is a source of propulsive efficiency increase.

Applying PBM, the expression in Eqn. 3-29 can be found which shows that drag-power balances the BL dissipation and body wake K.E. flow. Now it becomes clear that increasing the body wake K.E. flow term ($\dot{E}_{\text{body,wake}}$) to save shaft-power leads to an increase in drag-power. Thus increasing the body wake to increase efficiency seems unwise. If however this approach is pursued it means that drag-power is increased which requires the increase of thrust-power. The increase in thrust-power can be managed by two methods: increasing thrust or increasing free-stream cruise velocity of the aircraft. Increasing thrust means more shaft-power consumption. Increasing cruise velocity of the aircraft to utilize body wake energy can be beneficial if the engine performs more efficient in that particular velocity regime but this is unlikely. Thus increasing the body wake term to save shaft-power seems an unwise design consideration that requires a more rigorous detailed study. Thus the general design philosophy regarding the utilization of body wake flow to increase performance of BL or wake ingested propellers in terms of efficiency can be put as follows:

Utilize the existing body wake energy as much as possible.

$$KE_{\text{Loss}} = \iint_{TP} \tfrac{1}{2}\rho u(V_\infty^2 - u^2)dS \simeq \Phi_{BL} \tag{3-27}$$

$$KE_{\text{body,wake}} = \dot{E}_{\text{body,wake}} = \iint_{\text{TP}} \tfrac{1}{2}\rho u(u - V_\infty)^2 dS \tag{3-28}$$

$$DV_\infty = KE_{\text{Loss}} + KE_{\text{body,wake}} \simeq \Phi_{BL} + KE_{\text{body,wake}} \tag{3-29}$$

3-5 Ideal WI Integrated Body

In this part, the prescribed isolated airframe in Sec. 3-4 and the WI actuator are integrated. For simplicity and clarity, the ideal wake filling actuator is chosen as propulsor, such that the actuator captures all the upstream body wake flow of the airframe and ideally fills-in the flow, as illustrated in Fig. 3-4. Also it is assumed that the body and actuator are in a non-intrusive configuration. This is possible by placing the actuator far enough from the body such that their respective pressure fields don't mutually affect each other. This assumption eliminates the effect of pressure and consequently there is no pressure term. The effect of pressure is treated independently in Section 3-6.

The CV of the current ideal WI integrated body can be formed by combining the CV of the isolated airframe and the ideal wake filling actuator, as shown in Fig. 3-4. The non-intrusive assumption implies the pressure at SP recovers to ambient. The ideal wake filling actuator restores the outflow velocity from u to V_∞. This means that the outlet plane surface area must equal the inlet plane surface area to obey the mass conservation law for the CV. Thus there is no net change in momentum flow from inlet to outlet which means that there is no net force acting on the entire CV. If the net force is zero, the drag of the body is perfectly balanced by the thrust of the actuator. In terms of power, there is no wake flow entering nor leaving the CV. The only power term is the viscous dissipation rate (Φ_{BL}) inside airframe BL which is highlighted as the grey-shaded region in Fig. 3-4. The K.E. loss is caused by BL dissipation which can be quantified as the K.E. loss from free-stream flow at the inlet to wake at the SP (See Eqn. 3-31).

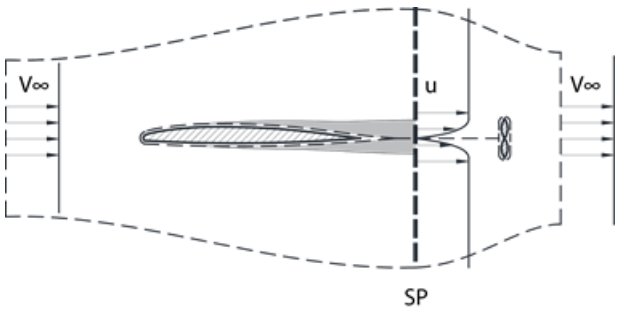

Figure 3-4: Control Volume for 2D WI Integrated Configuration[19]

$$KE_{\text{Loss}} = \iint_{SP} \rho u \tfrac{1}{2}(V_\infty^2 - u^2) dS \simeq \Phi_{BL} \tag{3-30}$$

The power input term is from the actuator which accelerates the slower moving wake back to the initial free-stream value. K.E. production rate ($\dot{E}_{\text{K.E.}}$) is the power term that captures it. Because there is no momentum difference between inlet and outlet, the actuator perfectly balances the BL dissipation caused by the airframe in front of it (See Eqn. 3-31).

$$\dot{E}_{\text{K.E.}} = KE_{\text{Loss}} = \iint_{SP} \rho u \tfrac{1}{2}(V_\infty^2 - u^2) dS \simeq \Phi_{BL} \tag{3-31}$$

As discussed earlier, the net force of the entire integrated body is zero meaning that actuator thrust cancels airframe drag. It should be noted that both forces indeed exist and have finite values that can physically be measured. Applying momentum equation for the actuator thrust and airframe drag separately gives Eqn. 3-32.

$$T = D = \iint_{SP} \rho u(V_\infty - u) dS \tag{3-32}$$

When checking the propulsive efficiency of WI actuator a value more than 100% is derived (See Eqn. 3-33). Because the amount of thrust-power(TV_∞) for this integrated case equals drag-power (DV_∞) of isolated airframe, it can be substituted which also gives an efficiency larger than 100% (See Eqn. 3-34). It is clear that in both derivations, airframe body wake KE flow term ($\dot{E}_{\text{body,wake}}$) causes the value more than 100%.

$$\eta_{\text{WI}} = \frac{TV_\infty}{\dot{E}_{\text{K.E.}}} = \frac{\dot{E}_{\text{K.E.}} + \dot{E}_{\text{body,wake}}}{\dot{E}_{\text{K.E.}}} > 1 \tag{3-33}$$

$$\eta_{\text{WI}} = \frac{DV_\infty}{\dot{E}_{\text{K.E.}}} = \frac{\Phi_{\text{BL}} + \dot{E}_{\text{body,wake}}}{\Phi_{\text{BL}}} > 1 \tag{3-34}$$

The body wake only exists inside the CV generated after the body tail and is immediately captured by the wake filling propulsor. Since there is no body wake flow penetrating the external boundary of the entire CV makes it clear that this term is a transient (temporary by nature) product within the CV, only observed between the body and propulsor. Since the propulsive efficiency includes an intermediate (temporary) power term, the efficiency cannot be interpreted in the classical sense. According to Peijian, for WI and BLI applications, the propulsive efficiency should better be referred as propulsive coefficient since the dimensionless quantity has no physical meaning in the classical sense. Discussion about the theory including efficiencies exceeding unity is extended in Chapter 4.

3-6 Propulsor-Body Interaction Effect for BLI

In the previous section where the body is integrated with a propulsor (WI integration), a non-intrusive assumption of body and propulsor was introduced for simplicity, assuming there is no interaction between the two elements. This assumption is made because in the WI configuration a certain distance exists between the body and propulsor. Within this distance the pressure is assumed to restore to ambient values before penetrating the propulsor. Consequently this assumption leads to the conclusion that body profile drag remains unchanged in the WI case. But in the BLI case, where body and propulsor are closely integrated, this assumption is no longer justified. This section discusses the propulsor interaction effect on the airframe profile drag.

Once a propulsor is mounted at the body tail to ingest the upstream BL flow, some part of the airframe would be immersed in the actuator induced pressure field. In order to capture this effect, the classical actuator theory can be used with suction side upstream and pressure side downstream. In this theory it is assumed that negative pressure gradient is maintained on both sides, except for a pressure jump between suction and pressure face crossing the actuator. The flow is continuously accelerated inside this pressure field. The classical actuator is a reasonable simplification, since the induced pressure field could be observed for a real rotating propeller. The body in this case is only concerned with profile drag. The profile drag of a typical body can be broken down into pressure (form) drag and friction drag. The BLI impact on each drag contribution is discussed respectively.

3-6-1 Body Pressure Drag

In order to demonstrate the interaction effect on body pressure drag, Peijian introduces a 6% thick symmetrical circular-arc airfoil which needs to represent the body. The pressure field for this isolated body, immersed in attached turbulent BL at Reynolds Number (Re) of 0.6 million, is shown in Fig. 3-5(a). The pressure coefficient distribution along the chord is shown as the solid line in Fig. 3-6. That is a typical pattern for an airfoil; the stagnation point and high pressure region located in the front. BL flow accelerated along the frontal surface where the pressure reduces accordingly until the maximum thickness is found where there exists a suction peak.

For this symmetrical arc airfoil, this suction peak is approximately located at 50% chord. Downstream this suction peak, the pressure gradually increases until body tail is reached where the flow encounters high pressure which is recognized as pressure recovery. Further downstream along the axis, BL flow leaves body surface where the pressure coefficient gradually returns to zero. It must be noted that the change of pressure is kept continuous when flow leaves body surface to enter the wake region.

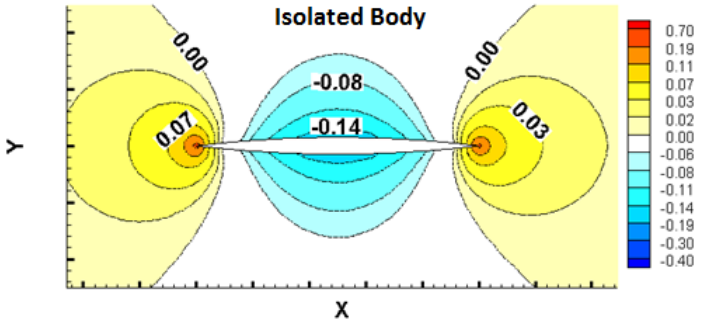

(a) Pressure Field for Isolated Body

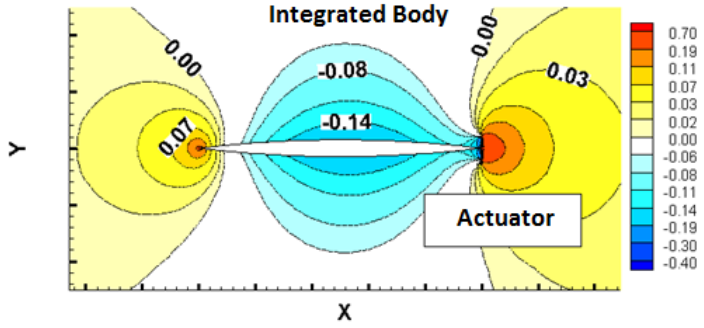

(b) Pressure Field for Integrated Body

Figure 3-5: Pressure Field for Isolated and Integrated Body Configurations[19]

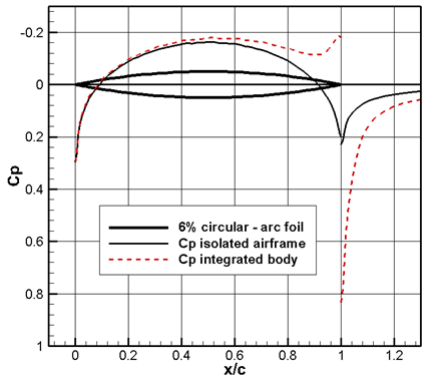

Figure 3-6: Pressure Coefficient for Isolated and Integrated Body[19]

In BLI integrated configuration, an actuator is installed at the body tail. Consequently the pressure contour with same Re is illustrated in Fig. 3-5(b). For demonstration purposes Peijian deliberately sets the actuator higher than required to achieve thrust-drag equilibrium condition. This is done in order to increase the pressure jump for better contrast. Compared with the isolated body in Fig. 3-5(a), the main distinction of pressure contour is located at the aft body close to the actuator. It can be seen that the integrated configuration shows a consistent reduction of the pressure recovery at the body tail which result in pressure drag of the sole body to increase.

Because of the impact of negative pressure caused by the actuator, the pressure on the rear body surface is reduced in general (See Fig. 3-6). The consequence is an increase in pressure drag which grows with the square of velocity. Consequently the pressure recovery of the aft

body is mitigated due to this induced pressure field. Less pressure recovery on the rear of the body must be compensated by the pressure increase on the pressure side of the actuator. In other words, the pressure recovery of the rear body which is spoiled by the suction side of actuator, is taken over by the pressure side of actuator. The pressure recovery shifts from the aft body to the pressure side of actuator which also offers an opportunity to maintain more favorable (negative) pressure gradient almost along the entire body axis. This pressure gradient delays separation (and therefore extra drag). This can be visualized in Fig. 3-6 where the pressure coefficient of the dotted line (representing the integrated configuration) achieves steep pressure recovery without separation. Note that after the discontinuity, the pressure decreases to zero further downstream in the wake region similar to the isolated body case.

3-6-2 Body Friction Drag

The BLI impact on the viscous friction drag is demonstrated by taking a flat plate representing the surface of the body. Since there is no pressure drag for the plate, only skin friction contributes to the profile drag. Assuming a laminar BL for the clean flat plate, the local skin friction is proportional to the velocity gradient at the wall (See Fig. 3-7(a)). Once an actuator disc is mounted at the body tail (thick vertical line in Fig. 3-7(b)), the BL profile cannot remain the same. In the region close to the suction side of actuator, the flow inside the BL is accelerated along the plate due to the negative pressure gradient (or suction) caused by the actuator. Because the non-slip condition holds at the flat surface, the velocity gradient at the wall accrues which increases the viscous shear stress. This means that the body friction drag also increases.

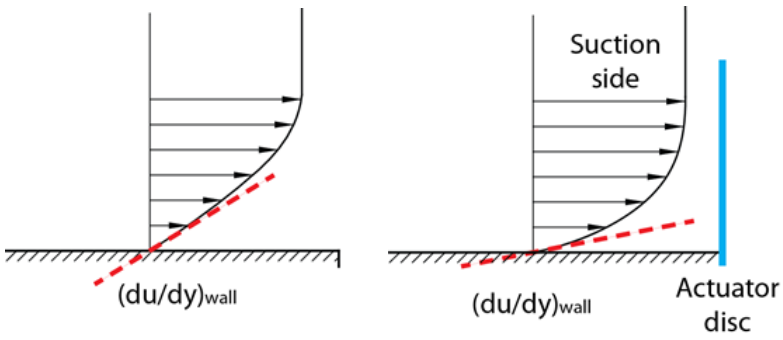

(a) Isolated Plate (b) Integrated Plate

Figure 3-7: Velocity Gradient for Isolated and Integrated Plate Configurations[19]

Chapter 4

Propulsive Efficiency

It could be seen in the previous chapters that the propulsive efficiency increases using Wake Ingestion (WI) and Boundary Layer Ingestion (BLI). Exceeding unity however should be impossible because it means that you generate energy for free which defies the laws of physics. In this chapter, a concise discussion is provided regarding this unity exceeding propulsive efficiency and an attempt is made to re-define it.

4-1 Earlier Propositions

Propulsive efficiency measures the effectiveness of a propulsive device in converting mechanical power input to propulsive power output (thrust-power). The definition of propulsive efficiency (η_p) can be found in Eqn. 4-1. Here V_∞ is the mass-flow velocity penetrating the propulsor inlet plane when the propulsor is taken as reference coordinate system. But according to ground reference, V_∞ can be regarded as the velocity of the propulsor unit itself. The u_{out} is the accelerated exit velocity aft of the propulsor. Rewriting this definition by assuming conservation of mass-flow ($\dot{m}$) and thrust equal to momentum excess (See Eqn. 4-2) leads to the simple expression depicted in Eqn. 4-3. The derivation of propulsive efficiency using momentum theory and actuator disk theory can be found in App. B.

$$\eta_p = \frac{\text{Propulsive Power}}{\text{Production Rate of Propulsive KE}} = \frac{TV_\infty}{\frac{1}{2}\dot{m}_{out}u_{out}^2 - \frac{1}{2}\dot{m}_\infty V_\infty^2} \tag{4-1}$$

$$T \approx \dot{m}(u_{out} - V_\infty) \qquad since \;\; \dot{m}_{out} \approx \dot{m}_{in} \approx \dot{m} \tag{4-2}$$

$$\eta_p = \frac{\dot{m}(u_{out} - V_\infty)V_\infty}{\frac{1}{2}\dot{m}(u_{out}^2 - V_\infty^2)} = \frac{2V_\infty}{V_\infty + u_{out}} = \frac{2}{1 + \frac{u_{out}}{V_\infty}} \tag{4-3}$$

Observing Eqn. 4-3 it can be seen that if the ratio in the denominator shrinks, the efficiency increases accordingly. If the incoming mass-flow velocity (V_∞) equals the outgoing mass-flow velocity (u_{out}) the propulsive efficiency, according to Eqn. 4-3, equals 100%. Meaning a perfect propelling system however if the outgoing mass-flow velocity is unaltered it also means that there is no thrust (See Eqn. 4-2). So the definition provided in Eqn. 4-3 seems to express exactly what it is defined to be, the efficiency.

For the definition provided in Eqn. 4-3 it seems that an efficiency above 100% is possible. This can be visualized when observing Fig. 4-1. In this figure an efficiency above 100% is possible for a velocity-ratio (u_{out}/V_∞) smaller than unity. However, a propeller that meets this condition is not a propelling device anymore. This is because the propeller is not accelerating the flow anymore but decelerating it since u_{out} is lower than V_∞. So the propeller is extracting energy from the free-stream flow, similar to a turbine. This makes sure that efficiencies above one appear in Fig. 4-1. Thus the propulsive efficiency provided in Eqn. 4-3 is perfectly in line with the physics behind the phenomenon. However, for BLI and WI applications this definition poses problems. The definition provided in Eqn. 4-3 cannot be used for BLI and

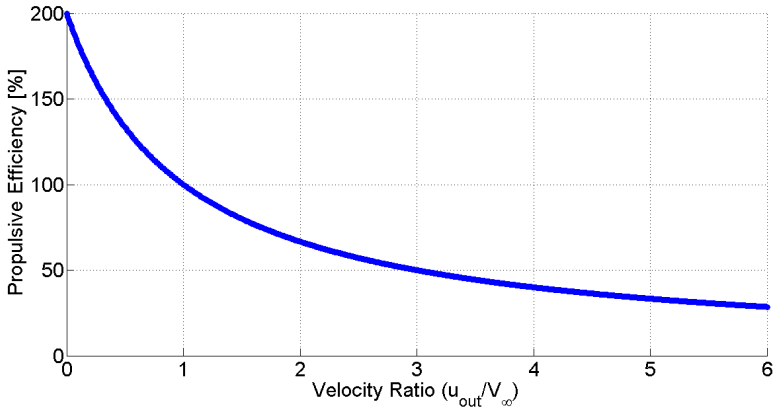

Figure 4-1: Classical Propulsive Efficiency

WI configurations because it does not represent the physics anymore. This originates from the fact that BLI and WI configured propellers require a different derivation than the one depicted in Eqn. 4-1. For these configurations the incoming velocity does not equal free-stream velocity but to a different lower incoming velocity. This needs to be incorporated inside the definition (see Eqn. 4-4). This definition can be worked out in a similar manner (see Eqn. 4-5 and 4-6).

$$\eta_{p_{BLI}} = \frac{\text{Propulsive Power}}{\text{Production Rate of Propulsive KE}} = \frac{TV_\infty}{\frac{1}{2}\dot{m}_{out}u_{out}^2 - \frac{1}{2}\dot{m}_{in}u_{in}^2} \tag{4-4}$$

$$T \approx \dot{m}(u_{out} - u_{in}) \qquad since \;\; \dot{m}_{out} \approx \dot{m}_{in} \approx \dot{m} \tag{4-5}$$

$$\begin{aligned} \eta_{p_{BLI}} &= \frac{\dot{m}(u_{out} - u_{in})V_\infty}{\frac{1}{2}\dot{m}(u_{out}^2 - u_{in}^2)} = \frac{2(u_{out} - u_{in})V_\infty}{u_{out}^2 - u_{in}^2} \\ \eta_{p_{BLI}} &= \frac{2(u_{out} - u_{in})V_\infty}{(u_{out} - u_{in})(u_{out} + uin)} = \frac{2V_\infty}{u_{out} + u_{in}} \end{aligned} \tag{4-6}$$

The propulsive efficiency that is applicable for WI and BLI configurations can be found in Eqn. 4-6. It can be seen that values exceeding 100% are possible for this definition by realizing that the sum in the denominator can be lower than the numerator. This is the case for a perfect wake filling propulsor because in this configuration the propulsor outlet velocity equals V_∞ and ingests incoming wake velocity (u_{in}) smaller than V_∞. The sum of these values are always lower than the numerator which directly results in efficiencies exceeding 100%. This should not be possible. This simply shows that the definition of propulsive efficiency is wrong for BLI and WI configurations!

Propulsive efficiency exceeding 100% was mentioned and discussed earlier by Smith (1991). Also, in McLemore Clyde (1962), it had been experimentally demonstrated that the maximum wake propeller efficiency was 122% in thrust to drag equilibrium condition. This experiment, conducted in National Aeronautics and Space Administration (NASA) Langley full scale wind-tunnel, consisted of a 1/20 airship model with stern mounted wake propeller. In this study it was proposed that the numerator of the propulsive efficiency should be corrected. This correction was needed for the velocity term in the numerator because, if carefully observed, the definition in Eqn. 4-1 defines incoming velocity (V_∞) as the velocity of the propeller/engine or aircraft w.r.t. the ground. This means that the actual decelerated mass-flow is not taken into consideration. It seems reasonable to replace the propulsive power term (TV_∞) by the instantaneous propulsive power (Tu_{wake}) for a propulsor ingested in the slower moving wake. But the replacement couldn't comply with the fact that in the free flight condition when propulsor ingests wake flow, it moves forward at V_∞, instead of the wake velocity u_{wake}, when observed from the ground fixed reference frame.

In earlier works, a correction parameter has been used to quantify the gains in BLI configuration for marine propulsion. This correction parameter, wake fraction which typically exceeds 1, was introduced to correct the"efficiency" gain when the identical propeller without wake ingestion is chosen as reference. A similar correction was suggested by Smith of using a power saving coefficient, that is the relative power saving. He introduced this coefficient using parameters that indicate whether a wake is ingested or not.

There are some other interpretations for this exceptionally high propulsive efficiency, one of them is provided by Peijian using the body wake (See Sec. 3-5). Lex assigns efficiencies above 1 to the body wake which is a transient product within the Control Volume (CV), only observed between the body and propulsor, because it is immediately captured by the wake filling propulsor. According to Peijian, the propulsive efficiency is not power conversion efficiency for WI and BLI conditions. That thrust-power which is canceled by airframe drag-power is not the "true" power output of actuator. More explicitly it includes an intermediate power term. To a large extent, this phenomenon explains the exceptionally high propulsive efficiency more than 100% which was observed in some earlier research. This is the reason why Peijian proposes to replace propulsive efficiency by propulsive coefficient in the context used for BLI and WI applications.

Recently, Prof. G. Eitelberg introduced an additional pressure term to make sure that efficiencies do not exceed 100%. According to Eitelberg, the loss of total pressure, which is the result of the momentum loss, has to be compensated by the propulsor. In order to accomplish this, more power needs to be used by the propulsor. This means that the power consumed by the propulsor equals the added kinetic energy flux and work done for the increase in pressure (see Eqn. 4-7).

$$P_{total} = \frac{1}{2}\dot{m}\left(u_{out}^2 - u_{in}^2\right) + \frac{\dot{m}\Delta p}{\rho} \tag{4-7}$$

The propulsive efficiency can be derived using this newly defined propeller power consumption:

$$\begin{aligned} \eta = \frac{P_{\text{useful}}}{P_{\text{total}}} = \frac{T \times u_\infty}{P_{\text{total}}} = \frac{2\dot{m}(u_{out} - u_{in})u_\infty}{\dot{m}\left(u_{out}^2 - u_{\text{in}}^2\right) + \frac{\dot{m}\Delta p}{\rho}} \\ \eta = \frac{2(u_{out} - u_{in})u_\infty}{(u_{out}^2 - u_{\text{in}}^2) + \frac{\Delta p}{\rho}} = \frac{2(u_{out} - u_{in})u_\infty}{(u_{out}^2 - u_{\text{in}}^2) + u_\infty^2} \\ \eta = \frac{2(u_{out} - u_{in})u_\infty}{(u_{out} - u_{in})(u_{out} + u_{in}) + u_\infty^2} \end{aligned} \tag{4-8}$$

For the perfect wake filling case, the inlet velocity is set to zero because it coincides with zero wake velocity. The propulsor in this configuration restores the momentum loss by accelerating this flow to u_∞. Substituting these values in Eqn. 4-8 gives a value of 100%. This result is perfectly in line with the expectations, meaning that the ideal wake filling propulsor uses power to simply restore the momentum loss and pressure difference. This case however assumes no frictional losses and consequently does not take the difference that exists between displacement thickness and momentum thickness into account. Also, it must be noted that the wake ingesting propulsor increases the drag of the body and will not fill the wake perfectly either. These considerations make sure that the efficiency is always lower than 100%.

4-2 Attempt in Defining a New Propulsive Efficiency

The propulsive efficiency which has physical significance is found in Eqn. 4-6. It was concluded in Sec. 4-1 that this efficiency exceeds 100% when the propulsor accelerates the slower moving wake flow to free-stream values. This condition is the perfect wake filling case. When the definition depicted in Eqn. 4-6 is observed carefully it can be noticed that the efficiency exceeds unity simply because the denominator misses a free-stream velocity term (V_∞). If this term is included in the denominator the following expression can be found in Eqn. 4-9.

$$\eta_{p_{NEW}} = \frac{2V_\infty}{u_{out} + u_{in} + \mathbf{V}_\infty} \tag{4-9}$$

If the derivation for BLI and WI configurations simply resulted in this expression (Eqn. 4-9) then no problems would occur in terms of efficiencies increasing unity. This can be simply shown by substituting values inside the expression. For example, for the perfect wake filling case, which is regarded as the limiting theoretical condition, the propulsor outlet velocity (u_{out}) equals free-stream velocity (V_∞). The ingested flow velocity (u_{in}) for this limiting case equals zero. When these conditions are substituted in Eqn. 4-9 a value of 100% can be found. This value corresponds with the expectation that the propulsor is simply restoring the lost momentum. For WI configurations where the ingested flow velocity (u_{in}) is larger than zero (a more realistic representation) and is accelerated perfectly to free-stream velocity (V_∞), the efficiency is always smaller than 100%. Needless to say, for the case where the propulsor accelerates the flow to values larger than free-stream velocity the efficiency also drops below 100%.

It is clear that this velocity term needs to be present in order to generate sensible efficiency results. What follows now is the application of mathematically tracing back the velocity term. The author decided to derive, in the direction to the source, the term that needs to be present in the definition to get V_∞ in the denominator. In Eqn. 4-10 this approach is shown in detail. Note that the extra velocity term (V_∞) is deliberately highlighted throughout the back tracing derivation.

$$\begin{aligned}
\eta_{NEW} = \frac{2V_\infty}{u_{out} + u_{in} + \mathbf{V}_\infty} = \frac{2(u_{out} - u_{in})V_\infty}{(u_{out} + u_{in})(u_{out} - u_{in}) + \mathbf{V}_\infty(\mathbf{u_{out}} - \mathbf{u_{in}})} \\
\eta_{NEW} = \frac{2(u_{out} - u_{in})V_\infty}{(u_{out}^2 - u_{in}^2) + \mathbf{V}_\infty(\mathbf{u_{out}} - \mathbf{u_{in}})} \\
\eta_{NEW} = \frac{\dot{m}(u_{out} - u_{in})V_\infty}{(\frac{1}{2}\dot{m}u_{out}^2 - \frac{1}{2}\dot{m}u_{in}^2) + \mathbf{\frac{1}{2}\dot{m}}\mathbf{V}_\infty(\mathbf{u_{out}} - \mathbf{u_{in}})} \\
\eta_{NEW} = \frac{TV_\infty}{(\frac{1}{2}\dot{m}u_{out}^2 - \frac{1}{2}\dot{m}u_{in}^2) + \mathbf{\frac{1}{2}}\mathbf{T}\mathbf{V}_\infty} = \frac{T \times V_\infty}{P_{\text{total}}}
\end{aligned} \tag{4-10}$$

In Eqn. 4-10 it can be seen that half of the thrust-power needs to be present in order to generate an efficiency that makes sense for BLI and WI configurations. Assuming that the new efficiency is correct, it can be seen that the total power required by the propulsor requires an extra thrust-power term ($^1/_2TV_\infty$). This thrust-power term is equal to drag-power for drag equal to thrust configurations. Here we can also see the effect of the body which is placed in front of propulsor. This effect is simply that the momentum defect needs to be overcome by the propulsor accompanied by an extra power source equal to half of the drag-power. This value, $^1/_2DV_\infty$, can also be assigned to the energy of the wake which needs to be overcome by the propulsor.

In Eqn. 4-11 the propulsive efficiency, applicable to both free-stream and BLI configurations can be found. A step function is introduced in order to cope with the difference that exists between both configurations.

$$\eta_{NEW} = \frac{TV_\infty}{(\frac{1}{2}\dot{m}u_{out}^2 - \frac{1}{2}\dot{m}u_{in}^2) + w(\frac{1}{2}TV_\infty)} = \frac{2V_\infty}{u_{out} + u_{in} + w(V_\infty)} \tag{4-11}$$

where,

$$w = \begin{cases} 1 & u_{in} < V_\infty \\ 0 & u_{in} \geq V_\infty \end{cases}$$

Chapter 5

Particle Image Velocimetry

In this chapter the wake field measurement technique, Particle Image Velocimetry (PIV), used in the experiment is introduced. PIV is needed to capture the velocity fields before and after the propulsor in order to close the momentum equation. The wake power terms ($\dot{E}_{\text{body,wake}}$) and ($\dot{E}_{\text{propulsor,wake}}$) present in Eqn. 3-19, can be derived from the velocity measurements using PIV. These results, combined with thrust, torque and Rotations Per Minute (RPM) measurements makes sure that all the power elements can be captured independently.

PIV is a measurement technique which records the displacement of small tracer particles, which travel along with the flow. The displacement between the particles is found by taking two sequential snapshots of tracer particles separated by a predefined time delay. Using the displacement of the particles and the known separation time the velocity component can be obtained along the desired illuminated sheet of flow. This measurement technique consists of seeding, illumination and imaging.[25] A typical PIV setup can be found in Fig. 5-1.

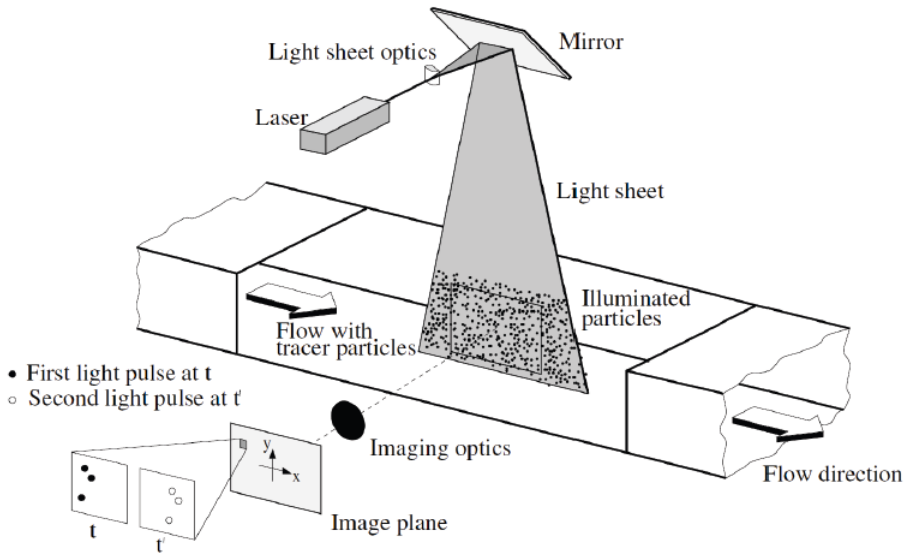

Figure 5-1: Schematic of a Typical PIV Measurement System[8]

5-1 Seeding, Illumination and Imaging

There are three main requirements for a seeding particle. Firstly, the particles should not affect the flow properties of the fluid that is being observed. This means that seeding concentration needs to be limited. A usual seeding concentration from 109 to 1012 particles/m^3 is demonstrated to have no effect on the flow. The parameter that captures this property is the ratio of mass of the fluid to the mass of the particles. Secondly, the particles should follow the flow trajectory. This property can be captured using Stokes Number (St) defined in Eqn. 5-1. If the Stokes number is small, that is much less than 1, it means that particles follow the flow trajectory. Third, the ability to scatter enough intensity to be recorded by the cameras.

$$St = \frac{\text{particle response time}}{\text{flow characteristic time}} \tag{5-1}$$

Illumination of the seeded particles is another important aspect in PIV which is performed using a laser. Laser pulses are used to illuminate the particles because of twofold reasons. Laser pulses are only 6-10 nanoseconds long thus freeze any motion and laser light can be focused into a thin enough light sheet so that only the desired seeded particles in that particular plane are imaged. The light scattered by the particles gets captured by the imaging device. The imaging system is usually defined by its focal length, aperture number and image magnification. The time between the frames when the camera is not recording is very short, down to 100 nanoseconds.

5-2 Stereoscopic PIV

For the actual experiment a modified version of PIV is performed, called the stereoscopic PIV. Stereo PIV is a method to capture the velocities in all three dimensions on a plane instead of two. The working principle remains the same as that of the conventional PIV. However by using stereo PIV, the third velocity component perpendicular to the plane can be obtained by using an additional camera. Stereo PIV is chosen for the experiment in order to be able to capture 3D components such as vortices present in the wake. This third perpendicular velocity component is obtained by the same principles that govern human eye sight. Human eyes are separated by a distance which enables the perception of depth because both eyes have the same field of view from different angles. The brain processes both two dimensional views into a single three dimensional one. In order to get the same effect for PIV, two inclined cameras observe the same plane from a different angle. In Fig. 5-2 a photograph of the stereo PIV setup can be found.

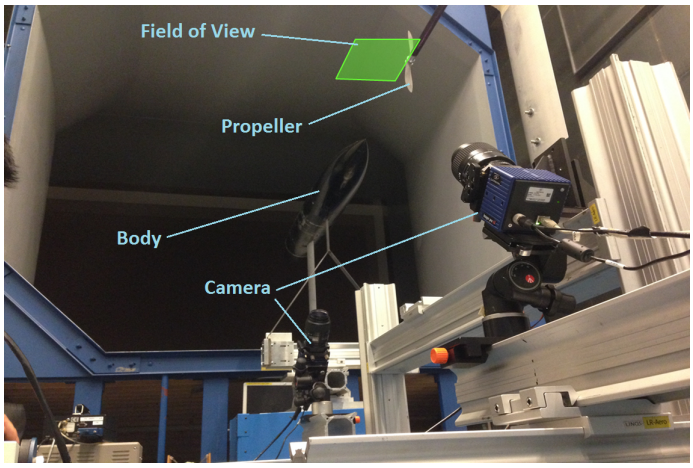

Figure 5-2: Stereo PIV Setup for the Experiment

In Fig. 5-2 it can be seen that two cameras which are non-parallel with their axis intersect at the image plane. The rotated cameras form an angle with respect to the image plane (green rectangle). An increase in the angle of rotation results in a greater accuracy in the out of the plane component. However the magnification obtained may no longer be uniform over the field of view. Since the cameras are inclined, the object plane is no longer parallel to the lens plane, it is therefore required to rotate the image plane by a certain angle so that the object plane, lens plane and the image plane lie along the same line. This condition is called as the Scheimpflug condition. This condition is achieved by rotating the lens with respect of the cameras (See Fig. 5-3).

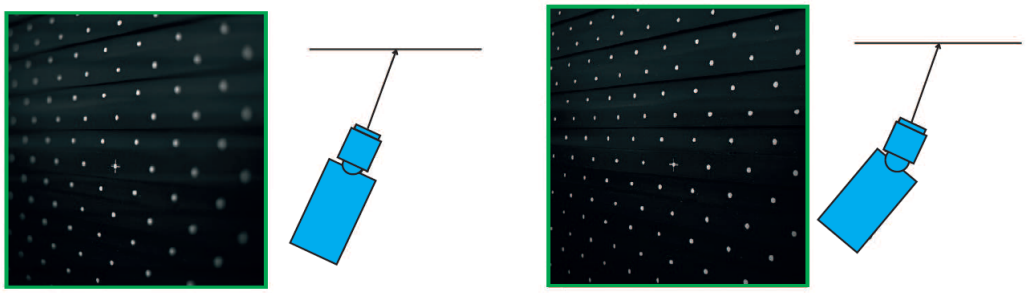

(a) Image Without Scheimpflug Condition (b) Image With Scheimpflug Condition

Figure 5-3: Scheimpflug Effect for Calibration Plate Image[8]

5-3 Image Processing

This section shortly discusses the main elements that need to be dealt with in evaluating the obtained PIV images. The obtained images are evaluated by means of dividing it into smaller interrogation windows on which cross correlation analysis is performed. This is required to quantify the distance of the seeded particles in order to derive the velocity field. Cross-correlation analysis is a method that finds similarity between two different measurements by generating a cross-correlation peak. The final velocity field is obtained by using the average displacement and separation time between the images. This procedure is illustrated in Fig. 5-4. Note that if the interrogation window is too large, it may be unable to capture flow details due to low spatial resolution. And if the window size is too small unphysical velocity vectors may be produced. In order to deal with the window size, overlapping is applied. For example, see Fig. 5-5 where particles from two consecutive frames are at different interrogation windows. The particles which are lost near the edge are recaptured using overlap. A 50% overlap is commonly used in practice in order to improve spatial resolution.[8]

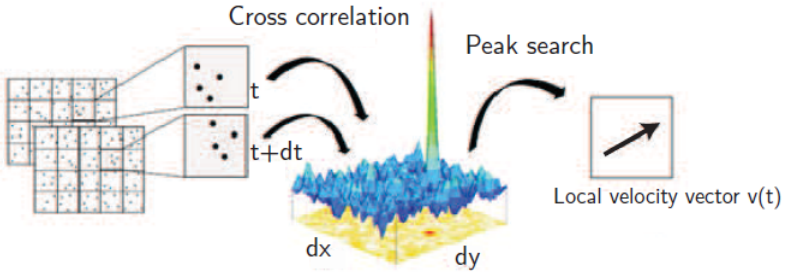

Figure 5-4: PIV Image Processing using Cross Correlation[8]

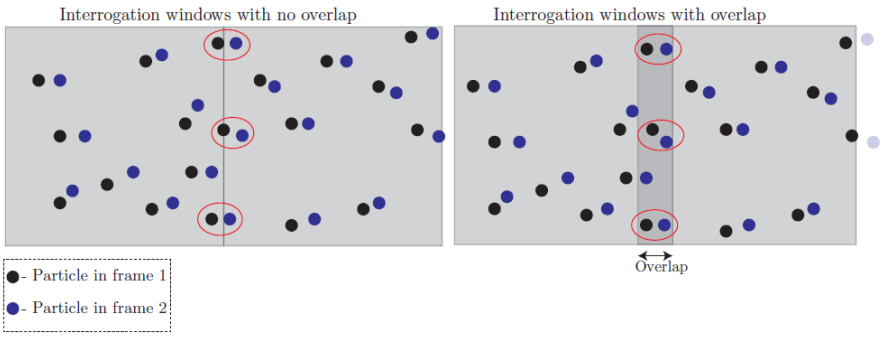

Figure 5-5: Overlap of Interrogation Windows[8]

5-4 PIV Calibration

Every rigorously applied measurement technique needs a proper calibration. The calibration for stereo PIV is based on acquiring coefficients for a polynomial mapping function. First a calibration plate is positioned in the plane of the object. This plate contains two matrices of white dots on a Cartesian grid. These matrices are separated by a small distance in depth caused by the geometry of the plate itself. Images of the plate are acquired using the two cameras. The image plane is mapped to the object plane by a mapping function. The location of these white dots is matched with a known template, this helps in determining the unknown coefficients of the mapping function. Figure 5-6 shows the calibration procedure for the stereo PIV.

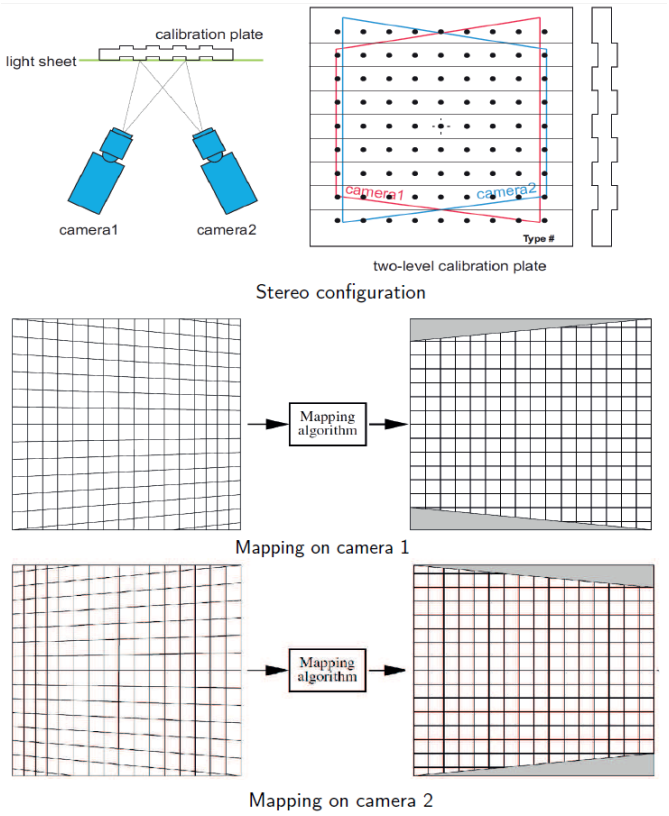

Figure 5-6: Calibration Procedure for Stereo PIV[8]

Part II

Experiment

Chapter 6

Experimental Setup

This chapter deals with the experimental setup required in answering the research question defined in Sec. 2-3. The chapter is roughly divided into four sections. In Sec. 6-1, the research question is translated into a hypothesis. This is followed by the used test-configurations in Sec. 6-2. Then the chosen body and propulsor for these configurations are treated in Sec. 6-3 and 6-4 respectively. The purpose of this chapter is to provide not only the experimental configuration but also the reasoning behind it.

6-1 Hypothesis

This thesis consists of a theory about Boundary Layer Ingestion (BLI) and Wake Ingestion (WI) in the form of an equation originated from applying the Power Balance Method (PBM) introduced earlier in Section 2-3. The research question for this thesis is defined in Sec. 1-2. A hypothesis is required in order to answer this research question experimentally. The power terms, built using PBM and mentioned in the research question, are repeated in Eqn. 6-1.

$$\dot{E}_{\text{wake,body}} + \dot{E}_{\text{kinetic energy}} = TV_{\infty} + \dot{E}_{\text{wake, propulsor}} \tag{6-1}$$

There is a clear hypothesis to be tested since the purpose of the thesis is based on experimentally testing a scientific theory. The null-hypothesis can be formulated as follows:

"All the power elements in Eqn. 6-1, built using the PBM for BLI and WI configurations, are quantified properly. These configurations are compared for performance which shows that BLI is an efficiency increasing phenomenon."

A wind-tunnel experiment is required to test this hypothesis. Preferably a low-speed wind-tunnel with little or no wall interference effects. The best option suitable for this purpose is the Open Jet Facility (OJF) of Delft University of Technology (DUT). The OJF has an open jet and a 2850 x 2850 mm octagonal cross section which eliminates wall interference effects. The large tunnel test section area w.r.t. test rig makes sure that the blockage effect is negligible. The dimensions of OJF are impressive; fan powered by 500 kilowatt electric motor enables a speed of 33m/s. Air is turned 180 degrees through a long diffuser and two rows of corner vanes (see Fig.6-1). It then passes through a short diffuser before entering the

settling chamber. Here, 5 fine-mesh screens reduce the turbulence and velocity deviations in the airflow. Via a contraction the air is then blown into the test section as an even jet stream and cooled at the end by an enormous cooling radiator and guided back to the fan.[4]

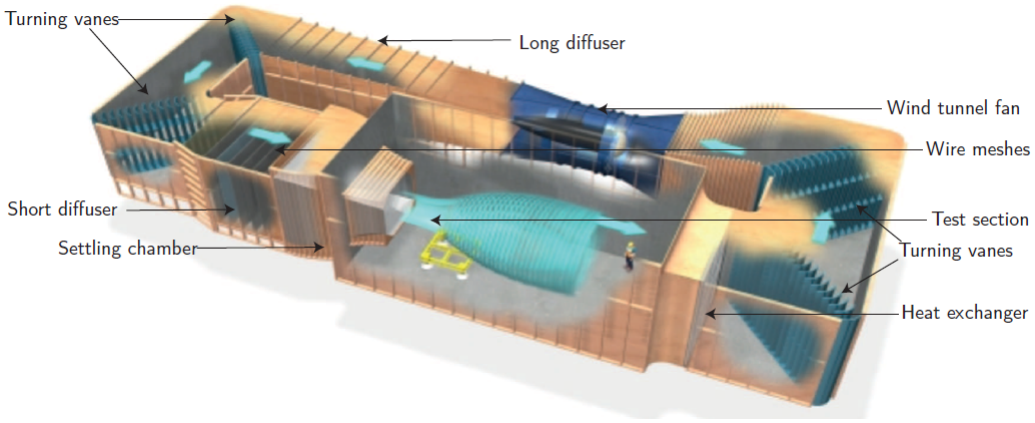

Figure 6-1: Open Jet Facility of Delft University of Technology[4]

Another consideration for testing the hypothesis is about the wake generating body and how to measure its drag and wake. Equally important, a propulsor needs to be used which is able to generate an equal amount of thrust and refills the wake accordingly. The following general approach needs to be performed to be able to test the hypothesis.

- Define suitable instruments which can be used to derive the power elements.
- Design an experiment which eliminates or quantifies the external factors.
- Properly conduct the experiment in a repeatable and unbiased manner.
- Apply a rigorous uncertainty analysis to the measured data.
- Attach conclusions to the obtained experimental results.

6-2 Test Configuration

There are 4 configurations which can be visualized in Fig. 6-2. For the WI case, the distance between the spinner tip and body tail is 400 mm. This distance is determined using a rigorous pressure survey where it is found that the static pressure is negligible. These static pressure measurements can be found in Fig. 7-3. This is required in order to eliminate any pressure factors that influence the flow and power terms.
These configurations are chosen such that the body drag is measured first. Then the undisturbed free propeller performance is captured. Finally, the integration of the body in WI and BLI configuration can be measured for comparison. Using this particular sequence the performance of different configurations can be compared properly using for example the propeller efficiency. For these configurations, two different wind-tunnel settings are practiced which are highlighted in Ch. 7.

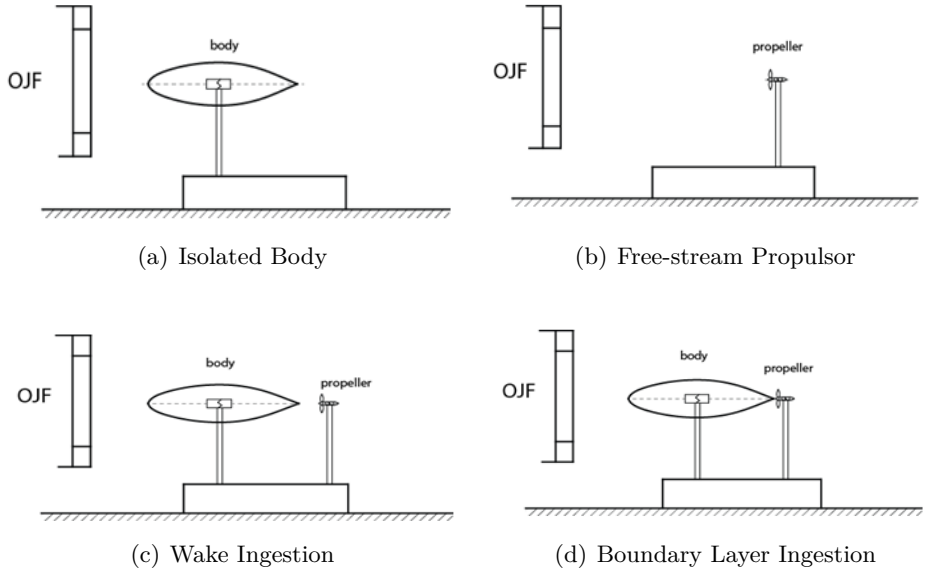

(a) Isolated Body (b) Free-stream Propulsor

(c) Wake Ingestion (d) Boundary Layer Ingestion

Figure 6-2: Configurations Practiced for the Experiment

6-3 The Body

Certain requirements exist for a body in an experimental setup. The basic principle is that a wake generating body is needed with a propulsor positioned in its wake. The wake needs to be large such that its properties can be measured more clear. Ideally a wake needs to be formed which has a constant large width and minimal turbulence without the existence of three dimensional components such as vortex formation. Also, a symmetry is preferred in order to make sure that no resultant forces or gust winds are formed which corrupt the wake formation. The best object which complies with these requirements and is available at DUT is provided in Figure 6-3.
The axial symmetrical body has a chord length of 1340 mm and a maximal diameter of around 300 mm. A zigzag tape is positioned at 20% of body length such that turbulent Boundary Layer (BL) is tripped. This BL is needed to create a larger wake behind the body that complies with propeller diameter width. There exists some practical difficulties when placing the body in the OJF. For example, when the body is placed in the OJF, it gives no possibilities to hang it. This requires the body to be rested on struts fixed to a plate or balance. This can pose problems under high velocity airflow in terms of flutter and vibrations depending on the strut design because the body weighs around 100 N. Thus it is important to choose a strut design fixed to the body with high stiffness. Due to practical reasons the drag of the isolated body cannot be measured. This is because no load cell or measurement device can be placed inside the body. This only leaves the option for the body with supporting struts to be placed on a platform where the total drag is being measured. Using this approach the drag of the body is deduced. Meaning that the measured drag is the drag of the body + strut drag. Thus a setup is required which has minimal strut drag. The body depicted in Fig. 6-3 was used earlier in another study. In that study, it was found that the drag generated by the isolated body is around 1.5 N for wind speeds ranging between 20-30 m/s. A body drag of 1.5 N is very small compared to a body weight of 100 N. This means that a very small drag force needs to be measured using a relatively heavy body. This requires very stiff struts that induce minimal strut-drag and very accurate drag measurements.

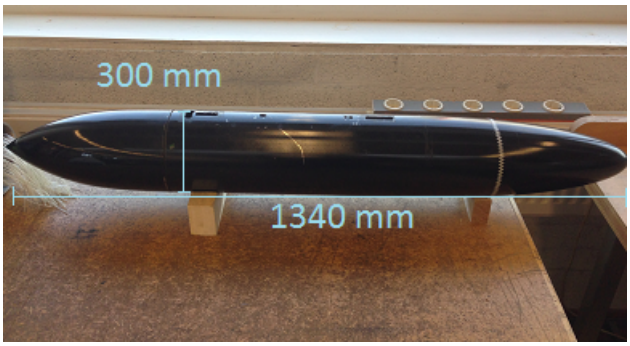

Figure 6-3: Photograph of the Body to be Used for the Wind-tunnel Experiment

Before designing any customized struts it was decided to first test the existing struts. These struts were used in a hanging configuration for an earlier study because the body was positioned in a closed test section where it was possible to hang the body conveniently. However, for this particular setup in the OJF these struts need to carry the weight of the body. In order to see whether these struts are capable of carrying the weight, a simple test was conducted. The strut properties, in terms of vibrations, was observed. This is performed by simply tapping on the body (see Fig. 6-4). This rather primitive test was convincing enough to conclude that the body needs at least one strut that is more stiff. The y-shaped strut depicted in Fig. 6-4 is concluded to be usable for the experiment for its shape causing good vibration resistant and stiffness properties.

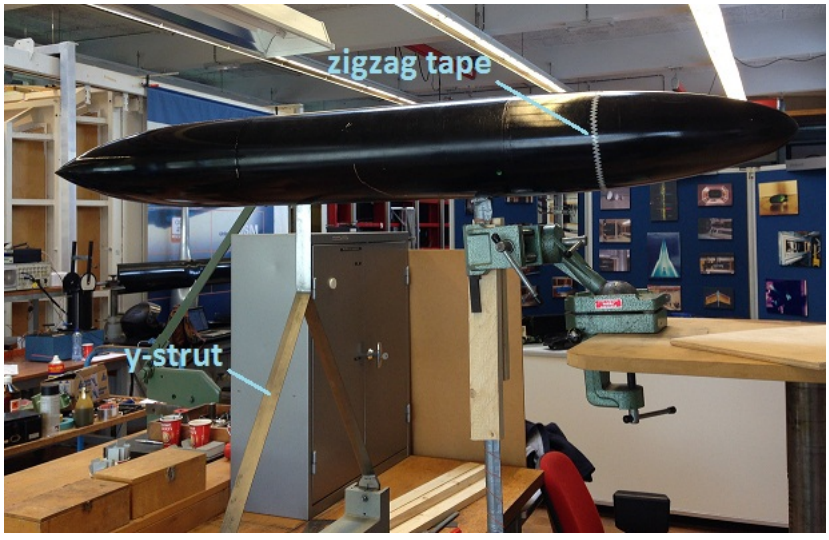

Figure 6-4: Photograph of the Body with Struts in Vibration Test Configuration

To improve strut design, the National Advisory Committee for Aeronautics (NACA) 0008 profile cross section strut was chosen due to its high stiffness, availability and low drag properties at low speeds. It is preferred to have a strut as long as possible in order to increase the distance between the body and the platform where it is attached. This is applied in order to make sure that the shear layer and ground effect are minimized. The length of the strut is usually bound by its stiffness but in this case the length is fixed to the height of the usable y-shaped strut. In order to see whether the NACA strut is able to perform well for the chosen length, simple experiments were conducted. In order to mimic a body

of 100 N resting on the strut, a dummy weight was placed (see Fig. 6-5(a)). By tapping on the dummy weight a vibration through the strut could be felt that lasted for a couple of seconds. This motivated the author into an attempt to increase the stiffness of the strut for the given length. Two methods are applied to stiffen the NACA strut, the first one is by pouring a stiffening resin (Fig. 6-5(b)) and the second one by placing an internal steel bar (Fig. 6-5(c)). It was concluded from the tests that the resin is not effective enough however an internal steel bar does increase the stiffness. The major downside of the internal steel bar reinforcement is the added weight. It might be argued that this additional weight is mainly the cause for the stiffness to increase.

(a) Strut in Testing Configuration (b) Strut Filled with Resin (c) Strut with Steel Bar

Figure 6-5: Photograph of NACA Struts

The platform which is used to attach the body with struts, is the so called 'flexure-balance'. This balance is chosen due to its rigidity which is able to support heavy objects and still is able to capture small scale displacements in axial direction. This is managed with the help of flexures that support the object and are simultaneously free to deflect in axial direction with negligible friction. For this 'flexure-balance' a load cell is required to be attached in such a manner that axial displacement is captured by it such that the drag is transduced. The author uses the word 'transduced' on purpose because drag is not measured, displacement is. This displacement is measured by a load cell. A load cell simply is a device which has thin strain gages which elongate if a force is applied to it. The strain gages, usually four or a multiple of four, are connected into a Wheatstone bridge configuration in order to convert the very small change in resistance into a usable electrical signal. The change in resistance by means of measuring the current results in a relative force. The relationship between strain and change in resistance is almost perfectly linear. Accuracy of 0.01% are not uncommon for a high accuracy load cell. Calibrating this sensor provides the direct force applied to the instrument. There exists many types of load cells; Shear beam, S-type, pancake, bending beam and single point load cells. The single point load cell is chosen due to its bending free measurement capability. Single point load cells probably account for the largest percentage of all load cells in existence world wide. Single point load cells use bending as a measuring principle. "single point" is really a bad name for these load cells. "platform" load cells would be far more applicable. What makes them different from all the load cells, is that the load does not need to be applied through a single mounting point on the load cell. Instead, a single point load cell will accept a platform of specified dimensions that can be bolted directly to the load cell. The load can then be applied to any point on that platform and the load cell will measure it accurately.[24]

The single point load cell must comply with a measurement range between 0-3 N. The load cell that meets this requirement is the BCM model 1668(S) illustrated in Figure 6-6.

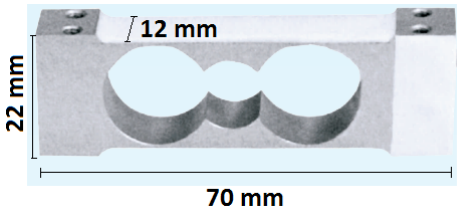

Figure 6-6: Fotograph of the BCM Single Point Load Cell[1]

This load cell is attached to the flexure on the balance such that forces that exist on the body are transferred from the body through the deformation of the flexure to this load cell. Because of the oblong shape of the load cell and the narrow distance of contact possible for the flexure, a L-shaped hook is designed (see Fig. 6-10(b)). In this figure it can be seen that point contact between the flexure and load cell is designed by using a marble.

A calibration test is conducted in order to measure the load cell performance and prepare it for the experiment. First the load cell is calibrated independently by placing different weights on top of it (Fig. 6-7(a)). Then the L-shaped hook is included in order to see whether it has an effect on the measured values (Fig. 6-7(b)). Both configurations are plotted in Fig. 6-8. Observing Fig. 6-8 it can be seen clearly that the load-cell performs satisfying for both configurations. This means that the L-shaped hook for the integrated load-cell configuration does not have a significant effect on load-cell performance. It seems that the integrated load-cell performs exactly the same as the isolated load-cell. During the calibration measurements however, a difference could be observed for the integrated load-cell configuration. For example, the load-cell required a longer time to converge to a single value. These effects are not visible in Fig. 6-8. These minor effects can be visualized when individual graphs are plotted for different weights. This has been done for both isolated and integrated load-cell configurations which can be found in App. C.

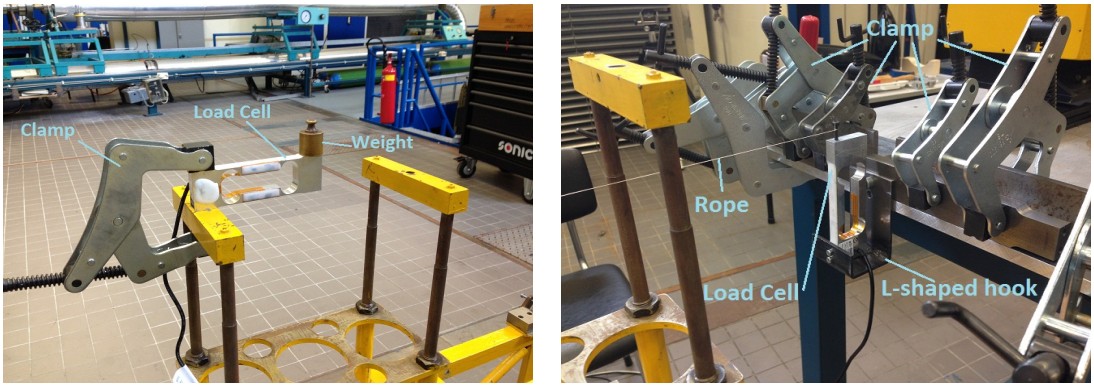

(a) Weight Presses on the Isolated Load Cell (b) Weight Pulls on the Integrated Load Cell

Figure 6-7: Calibration of Single Point Load Cell

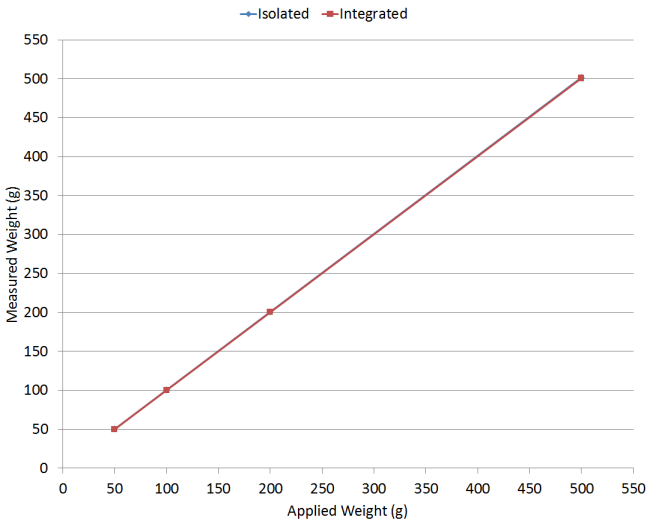

Figure 6-8: Calibration Results for Isolated and Integrated Load-Cell Configurations

The 'flexure-balance' seems too rigid and clumsy when compared to the delicate load cell attached to it. This observation initiated the author to conduct an experiment in the wind-tunnel to capture the behavior of this balance along with calibrating it. The setup of this experiment can be found in Fig. 6-9(a). Here it can be seen that a force is applied through the center of the object which is attached to the 'flexure-balance'. The NACA strut is reinforced, not only by an internal steel bar placed along the entire length but also by applying side reinforcements to better cope with vibrations (see Fig. 6-10(a)). Initial tests showed that when a force is applied to the body, the measured value of the load cell fluctuated continuously without converging to a single value. It was thought that this continuous vibration was due to the vibration of the L-shaped hook which held the load cell in its place. In order to eliminate these vibrations, the L-shaped hook was fixed to the ground using thick bolts (see Fig. 6-10(b)), unfortunately without result. The second (ineffective) idea to overcome this problem was by taking average results over long time spans. Please note that the single point load cell and the flexure are in point contact established using a marble (see Fig. 6-10(b)).

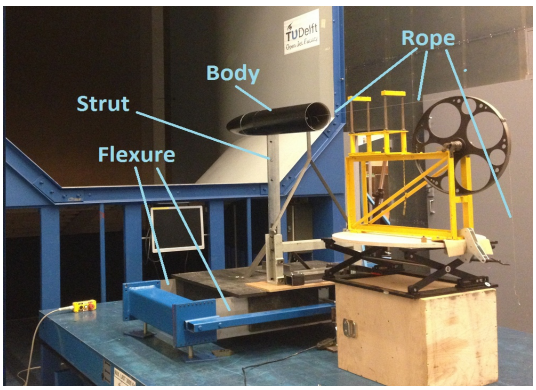

(a) Photograph of the Calibration Setup

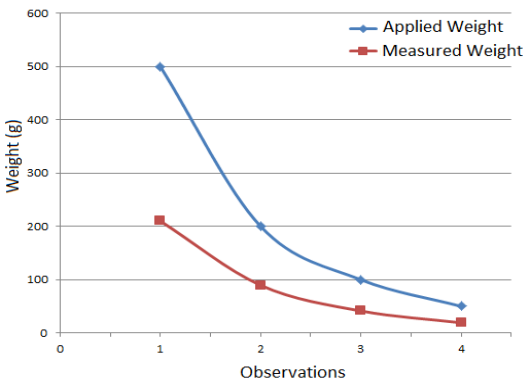

(b) Calibration Results

Figure 6-9: Wind-tunnel Calibration Test

This wind-tunnel calibration test (Fig. 6-9(a)), which was an initiative of the author, showed unsatisfying results. These results can be found in Fig. 6-9(b). It can be concluded from Fig. 6-9(b), that 50% of the loads are absorbed by the flexures due to friction! Because a lot of preparation and work was conducted in using this balance, the linearity was investigated with the intention that if the behavior of this friction is linear, the 'flexure-balance' can still be used by correcting for it. Unfortunately, the 'flexure-balance' was nonlinearly absorbing around 50% of the applied forces. Since also the vibrational issue could not be solved, it was concluded that this 'flexure-balance' is useless for the experiment. The search for another balance started.

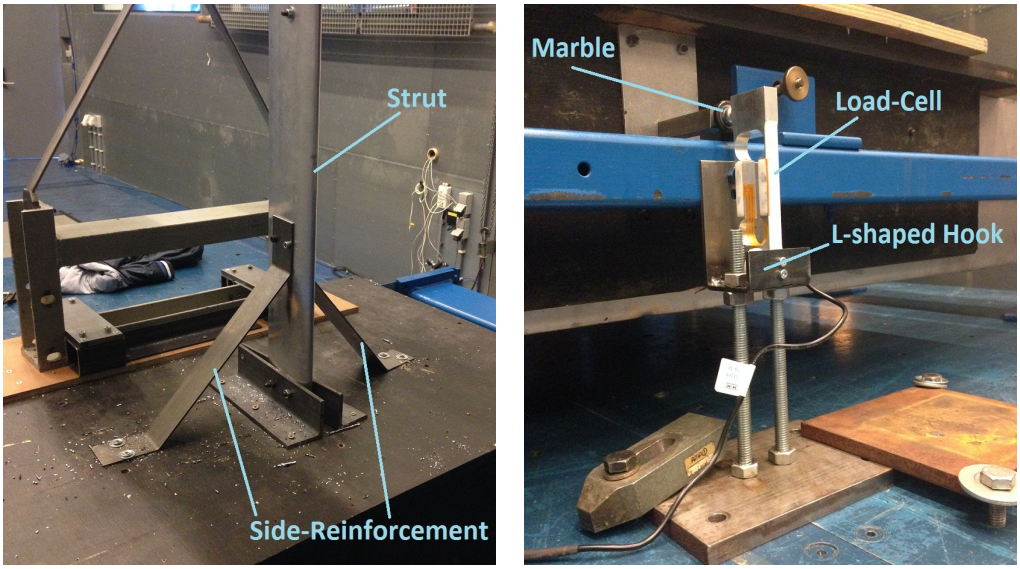

(a) Side Reinforcements for NACA Strut (b) Ground Reinforcements for the Load Cell

Figure 6-10: Reinforcements Applied for the Calibration Test

The only available option for replacing the flexure balance was the 6-component balance. This new balance was immediately tested and calibrated to capture its performance (see Fig. 6-11(a)). The calibration process is performed such that a dummy weight of 15 kg is placed on the balance to mimic the body with struts on top of it. The results of this process can be found in Fig. 6-11(b). The balance performance has a deviation from the true value of around 1%. The performance of this balance is better than expected for this low force regime because the 6-component balance is designed for forces way beyond this low regime, 250 N axially. Note that this balance is able to measure forces in 3 axial directions and 3 moments. This means that there is no need for a load cell to be attached to the platform.

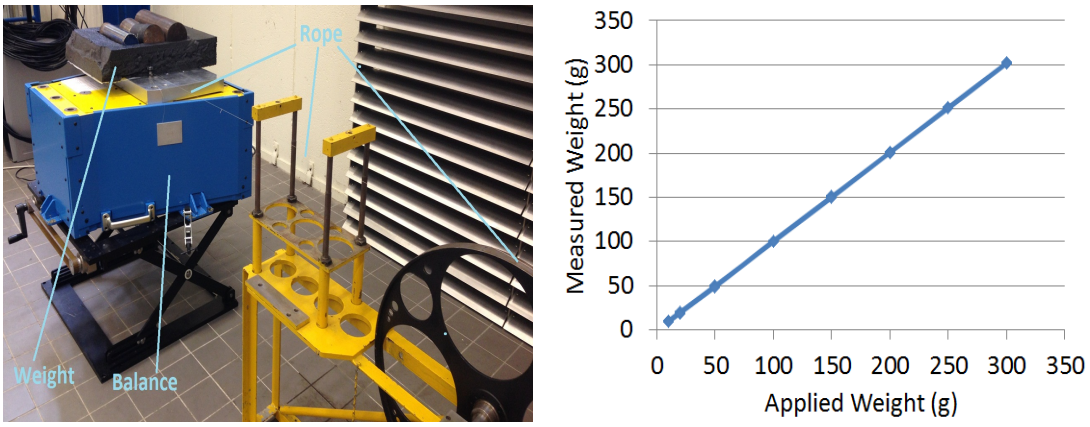

(a) Photograph of the Calibration Setup

(b) Calibration Results

Figure 6-11: Calibration of the Six-Component Balance

6-4 The Propulsor Unit

In this section, the decisions regarding the design of the propulsor are treated. A suitable propulsor for this experiment could not be found in the facilities of DUT. This is mainly because the forces which need to be generated and measured by the propulsor are small scale, less than what is usually accustomed.
The main purpose of the propulsor is to generate a thrust which is at least equal to the drag generated by the body. This way a cruise flight condition can be mimicked. The propulsor however needs to ingest a wake when put in WI or BLI configurations. This means that information is needed about wake diameter generated by the body depicted in Fig. 6-3. The wake depends on body properties but also on wind-speed conditions generated inside the OJF. Since the working conditions of OJF and body geometry is known, a Computational Fluid Dynamics (CFD) analysis can be applied. The result of this CFD analysis can be found in Fig. 6-12 where it can be seen that the diameter of the wake does not exceed body diameter. The quantitative data generated using CFD can be found in Table 6-1.

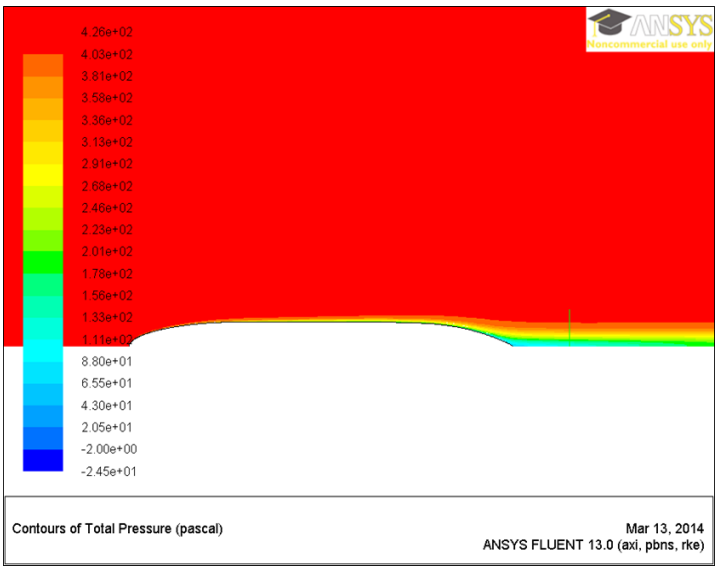

Figure 6-12: CFD Results for a Body in OJF Conditions

Table 6-1: CFD Results for a Body Immersed in OJF Condition

Parameter	Quantity	Dimension
Velocity	26	$^m/_s$
Reynold Number	2,39E+06	-
Wake Energy	3.85	W
Drag	1.475	N
Drag-Power	38.4	W
Wake Diameter	0.2	m

The required propeller can be found using CFD results. The CFD results provide an indication about the width of the wake and the drag generated by the body. This poses limitations on the propulsor. A propeller diameter (D) of 0.2 m is required in order to capture wake properties (see Table 6-1). Since the CFD also provides the drag generated by the body, an indication about the thrust range requirement of the propulsor is also set which is between 1.5 N and 3 N. Using the calculated indicative parameters propeller diameter and thrust, and knowing the wind-speed generated by the OJF gives a limited amount of propellers. These can be found in Table 6-2. These propellers are chosen such that the diameter (0.2 m) at the wind-speed of OJF (26 $^m/_s$) provides a thrust slightly higher than the drag of 1.475 N which was found using CFD. Note that propeller diameter and pitch are expressed in inch.

Table 6-2: Propellers Suitable for the Wind-tunnel Experiment

Propeller Brand (diameter" x pitch")	Velocity ($^m/_s$)	Thrust (N)	Torque (Nmm)	RPM
APC 8x7 (D = 0.2 m)	23.74	2.06	70.79	9000
APC 8x8	23.78	1.87	70.00	8000
APC 8x9	23.78	2.50	95.22	8000
APC 9x6 (D = 0.23 m)	24.18	2.11	75.09	9000
APC 9x8	24.14	1.74	74.18	7000
APC 9x9	24.05	2.44	104.49	7000
APC 10x9 (D = 0.25 m)	24.54	1.81	88.77	6000

The propeller performance can be used to choose the motor. In Table 6-2, the torque and Rotations Per Minute (RPM) range can be found. This poses requirements on the motor which needs to provide the rotations. Two main requirements exist; RPM range and torque range. The best suitable and reliable motor that meets the torque and rpm range can be found in Fig. 6-13. Observing Fig. 6-13(b) it can be seen that torque range between 70 and 104 Nmm and RPM range between 6000 and 9000 are fully satisfied.

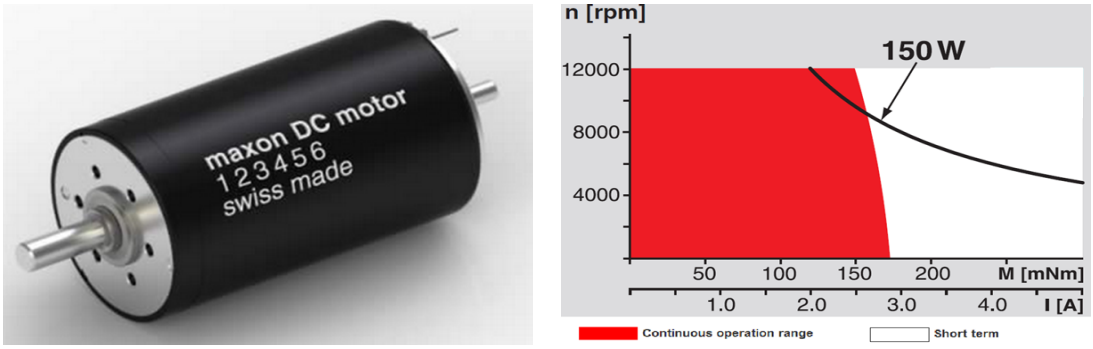

(a) Photograph of the Maxon D/C motor (b) Performance Range of the Maxon D/C motor

Figure 6-13: Maxon D/C Motor

Different methods can be applied to count the RPM of the propeller driven by the motor. For example, placing a laser which detects each passing of a propeller blade is possible. Another method is using a magnetic hub for the propeller that induces a magnetic flux for each rotation. A sensor can be placed such that these magnetic fluxes are counted. These methods require a sensor to be placed detached from the propulsor setup. This can generate interference effects in the OJF. The best integrated solution is to use a decoder attached behind the motor. The encoder suitable for the Maxon motor can be found in Fig. 6-14.

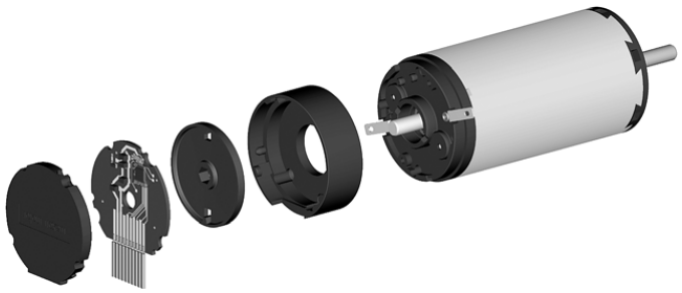

Figure 6-14: Encoder for Motor RPM Count

Since the setup involves small scale changes in force and torque (see Table 6-2), deriving the torque and force using RPM, power consumption and velocity changes can pose large errors. This is the main reason to directly measure the parameters thrust and torque. These parameters are needed, not only to assist the quantification of the power elements, but also to monitor the propeller efficiency in BLI conditions. The torque meter must have a measurement range that lies between 70 and 104 Nmm. Before the instrument that complies with this range is provided, an introduction to torque in general is required.
For a rotating object (e.g. a shaft), torque consists in two forms: static and dynamic. If the shaft is accelerating or decelerating the dynamic torque is dominant. If the shaft is non-rotating or rotating with constant RPM, thus without acceleration, static torque is dominant. Since the experiment aims at a constant RPM, static torque measurement is required. The static torque can be measured both by the rotating torque sensor and reaction torque sensor. The rotating torque sensor is straight forward, it senses the elongations in the strain gages, or difference in current (depending on the type of rotating torque sensor) due to the existing static torque in the shaft. Since coupling inside the shaft and the added weight to the shaft can pose problems this sensor type is not attractive for small scale wind-tunnel setup. The reaction torque sensor, non-rotating type, is more feasible. But how can this sensor measure

the torque inside a shaft is the next question. This is fairly easy using Newton's third law; action equals reaction. When a motor provides shaft-power to create torque, this can be sensed by placing a reaction torque sensor in the back of the motor. Instead of measuring the directional torque applied by the motor to the propeller, the reaction torque sensor can be placed such that the counter directional torque from the propeller to the motor can be sensed. This can be understood properly using Figure 6-15. The thrust generated by the propulsor needs to be measured too. This can be accomplished using the single point load cell depicted in Fig. 6-6. The data regarding the calibration and performance of this single point load cell can be found in Fig. C-1 and C-2.

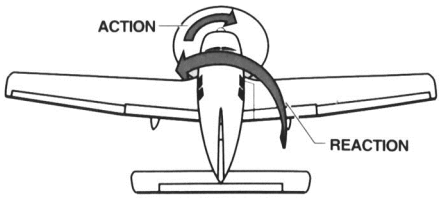

Figure 6-15: Visualization of Action and Reaction in Terms of Torque[2]

The propulsor is fully designed by Peijian using Catia software which can be observed in Fig. 6-16. In Figure 6-17(a) from left to right the following instruments can be detected; propeller, shaft, D/C motor, reaction torque sensor and single point load cell. Also an extension bar can be found for shifting the center of gravity towards the torque sensor to minimize additional torque measurement errors. A relative large distance can be observed between the propeller and the driver, this is to reduce the interference drag by the presence of the instruments behind the propeller. Every part for the propulsor is designed and/or purchased. The external aerodynamic casing is 3D printed. A photograph of the propulsor can be found in Fig. 6-17(a). Here the casing on the back is omitted on purpose to be able to view the internal components.

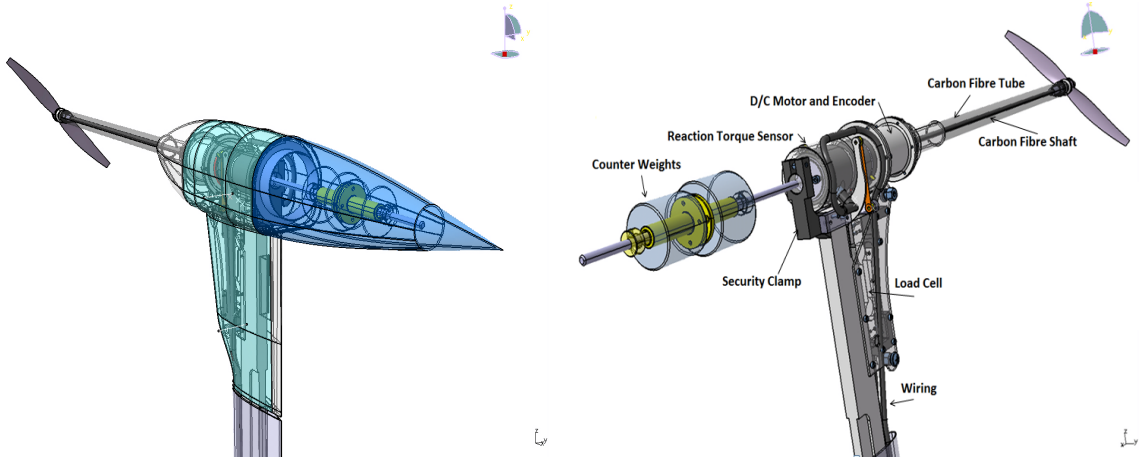

(a) Propulsor Side View with Casing

(b) Propulsor Side View Omitted Casing

Figure 6-16: Propulsor Design using Catia Software (Courtesy of Peijian)

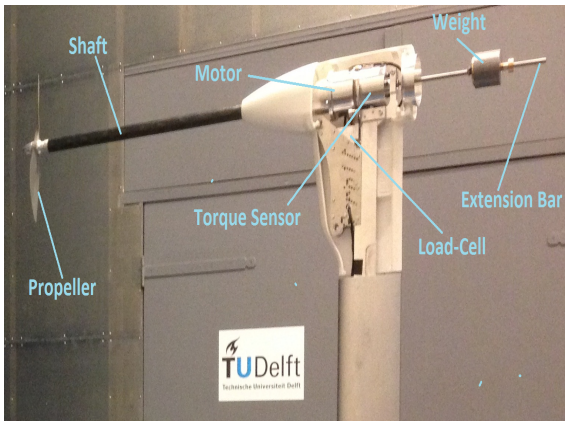

(a) Photograph of the Propulsor with Semi-Casing

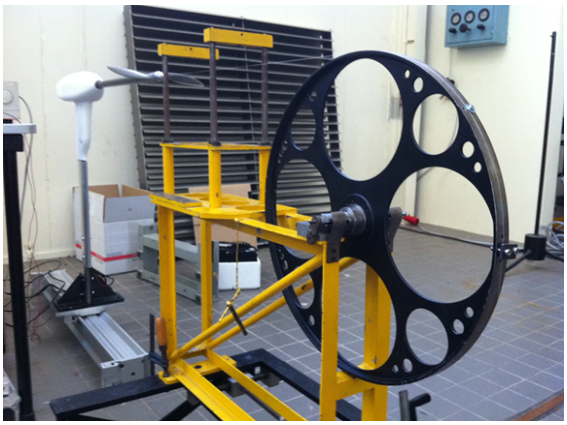

(b) Propulsor Integrated Load Cell Calibration Setup

Figure 6-17: Propulsor Photograph and Thrust Calibration Setup

In order to use this propulsor, calibration is required. The load cell used for the propulsor is identical to the one intended to be used for the balance in Sec. 6-3. It was concluded that this load cell performs well for this experimental setup where low drag forces are dominant. The load cell performance does change for different configurations but not very significant. This could be seen when observing the isolated and integrated load cell calibration results depicted in Fig. 6-8. However, a small-scale performance change could be observed for the integrated load cell calibration. These small-scale differences can be visualized in Fig. C-1 and C-2.

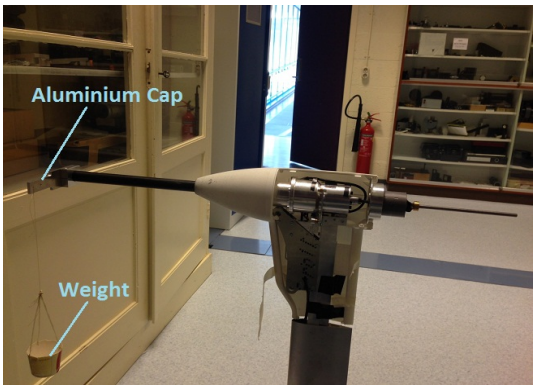

(a) Torque Calibration Setup

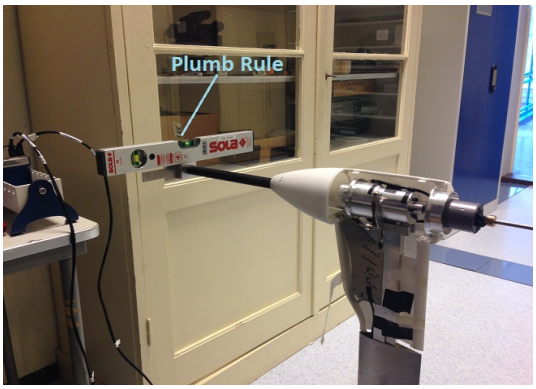

(b) Plumb Rule on the External Propulsor Shaft

Figure 6-18: Torque Calibration Setup for Propulsor

The load cell integrated with the propulsor unit requires a calibration because there exists a small change in performance for different configurations. The calibration is accomplished by pulling with a force to the shaft of the propeller. The pulling force is, similar to earlier calibrations treated in Sec. 6-3, modulated by weights attached to a pulley (See Fig. 6-17(b)). The calibration curve for the force can be found in Fig. 6-19(a).
The torque sensor, similar to the load cell, also requires calibration. The torque sensor is calibrated by simply applying a torque to the external shaft using small scale weights separated by a distance of 10 cm from the shaft centerline.

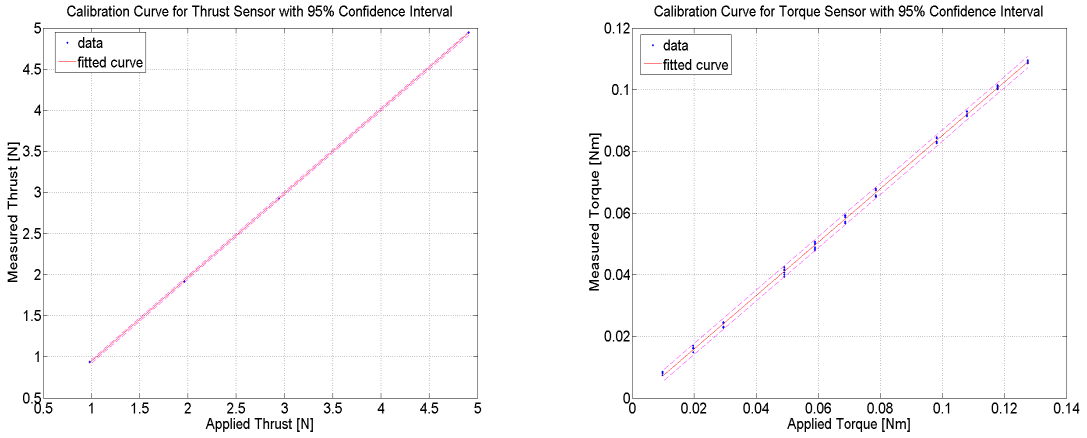

(a) Thrust Calibration Result

(b) Torque Calibration Result

Figure 6-19: Calibration Results for Propulsor

In Fig. 6-18(a) the external shaft with an aluminum cap fixed to the end can be visualized. Weights are applied to the edge of this aluminum cap which is a torque w.r.t. the sensor positioned at the shaft centerline. A plumb rule is positioned from time to time during the calibration on top of this aluminum cap to make sure that the force applied by the weight is perpendicular to the centerline (See Fig. 6-18(b)). The obtained data regarding this calibration can be found in Fig. 6-19(b).

Chapter 7

Experimental Implementation

This chapter deals with the experiment carried out in the Open Jet Facility (OJF) of Delft University of Technology (DUT). Initially, the two wind-tunnel settings used in the OJF are highlighted in Sec. 7-1. This is followed by the considerations regarding the implementation of these wind-tunnel settings for isolated body, free-stream propulsor and Wake Ingestion (WI) and Boundary Layer Ingestion (BLI) configurations in Sec. 7-2, 7-3 and 7-4 respectively. Finally, Particle Image Velocimetry (PIV) which is needed to capture the wake terms in Eqn. 6-1, is treated in Sec. 7-5.

7-1 Conditional Settings for the OJF

In order to capture the power elements in Eqn. 6-1 and compare different configuration settings using propeller efficiency, a plan of approach is required. The plan of approach is based on two conditional settings applied throughout these wind-tunnel experiments; 'Equilibrium' and 'Constant Speed'.
In the equilibrium setting the pure body drag is set equal to the thrust generated by the propulsor for a range of wind-speed settings in order to impose cruise conditions. These wind-speed settings can be found in Table 7-1. Note that 20 m/s is not used because that wind-speed range of the wind-tunnel coincides with a rotational velocity of the wind-tunnel fan that causes disturbing vibrations (eigenfrequency). For the constant speed setting the wind-tunnel speed is set to a predefined value where the propulsor setting is changed such that the generated thrust increases and decreases w.r.t. the body drag (see Table 7-1). This predefined value is chosen as high as possible to be able to capture distinct changes in forces. The tested configurations can be found in Fig. 6-2. Both conditional settings are carried out for WI and BLI configurations depicted in Fig. 6-2(c) and 6-2(d) respectively. These configurations are tested in the exact order as depicted in this figure. This is the reason why the isolated body configuration (see Fig. 6-2(a)) is treated first in this section.

Table 7-1: Conditional Settings applied in the OJF

Conditional Setting									
Equilibrium [m/s]	5	10	12	14	16	18	22	24	26
Constant Speed [m/s]	26								

7-2 Isolated Body Configuration

A photograph of the isolated body configuration can be found in Fig. 7-1(a). In order to capture the pure body drag (without struts), the strut drag needs to be quantified too. Thus the following approach is performed using the 'Equilibrium' setting: First the configuration depicted in Fig. 7-1(a) is measured where the values for the body drag with struts is captured. Then the body is detached from the setup to purely capture the strut drag in similar wind-speed conditions, this setup can be found in Fig. 7-1(b). Then a simple subtraction between the isolated body configuration and the pure strut configuration results in a fictitious pure body configuration. However, it is not that simple. These two configurations, although measured at similar varying wind-speed conditions, can not be subtracted using the measured drag values. Because it is impossible to measure both configurations in the exact same conditions. In order to cope with this, the Drag Coefficient (Cd) is calculated at each wind-tunnel setting captured in the form of Reynolds Number (Re). The Cd versus Re curve is generated for both configurations depicted in Fig. 7-1. These two Cd curves are then subtracted from each other which gives the Cd of the pure body at each wind-speed setting. This makes sure that for a given wind-speed setting, captured in the form of Re, the pure body drag can be derived accordingly. The specific calculations used to capture the body drag can be found in Sec. 8-1.

(a) Isolated Body Configuration with Struts (b) Configuration with only Struts

Figure 7-1: Photograph of Isolated Body Configuration

7-3 Free-stream Propulsor Configuration

The free-stream propulsor configuration can be found in Fig. 7-2. For this configuration both settings are practiced; 'Equilibrium' and 'Constant Speed'. For the equilibrium setting, wind-speed settings of the wind-tunnel are set according to the values defined in Table 7-1. The propulsor thrust setting is tuned to values equal to the body drag at each wind-speed condition. This is accomplished using automatic real time calculations in the wind-tunnel using Labview software. Without going too much into detail this software uses wind-tunnel parameters to compute the Re which is the input required to compute the Cd of the body at that particular condition. This Cd is then used to compute the drag of the body. Note that the relation between Cd and Re is already programmed in Labview in this stage because

it is found earlier during the isolated body configuration. The propulsor is then manually tuned by varying the Rotations Per Minute (RPM) to generate the amount of thrust equal to the body drag which is a requirement for the equilibrium setting. The amount of thrust generated by the propulsor is real time measured by the integrated load cell.
The constant speed setting is managed by simply setting the wind-speed to 26 m/s and varying the thrust from values below the body drag to values above it. Note that thrust values below the body drag can be interpreted to descent and thrust values higher than body drag to ascending of an aircraft. But this interpretation is purely based on positive and negative net-force values.
Note that the positioning of the propulsor is rigorously carried out by preventing the shear layer, generated by the wind-tunnel test section, from striking the propulsor unit. This is managed by attaching tufts to a stick and watch its behavior at different locations. The tufts radically vibrate and occasionally reverse its direction w.r.t. wind-direction when immersed in turbulent flow. Using these tufts the shear layer growth is observed and accounted for.
Also note that in this configuration the torque is measured along with thrust and RPM which are needed to compute the shaft-power required to calculate the propeller efficiency. This free-stream efficiency can be used as a baseline for WI and BLI configurations.

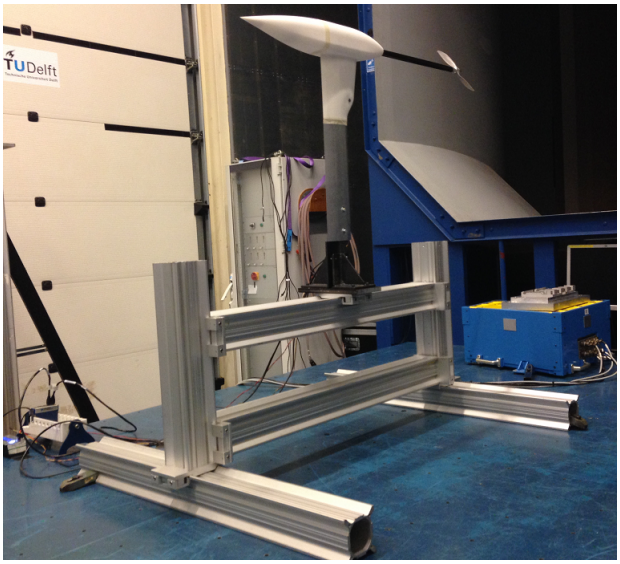

Figure 7-2: Photograph of the Free-stream Propulsor Configuration

7-4 Wake- and Boundary Layer Ingestion Configuration

The WI configuration can be found in Fig. 7-4(a). In this figure, the body and propulsor can be seen with a pitot-static tube behind the propulsor. This photograph is taken during the mapping of the pressure field around an operational propulsor in WI configuration. For this WI case the distance between propulsor and body is set to 400 mm. This distance is required for the theory because Power Balance Method (PBM) applied to WI configurations assume that no pressure effects exist on the propulsor (see Sec. 3-5). This non-intrusive configuration between the body and propulsor is only possible by placing the propulsor far enough such that their respective pressure fields don't mutually affect each other. This distance is found by performing pressure measurements that start directly from the body trailing edge backwards until a distance is found where the static pressure is unchanging.

The result of this pressure survey can be found in Fig. 7-3. Here the black lines denote the objects in side-view; left is the semi-cut of airframe trailing edge and right is a semi-cut of the propeller. The green dotted line gives the actual position of these pressure measurements, so where the pitot-static probe is traversed in 2D space. The blue curve gives the total pressure where the red curve gives the static pressure. The total pressure along the axis is increasing. The total pressure is an indicator of energy for a point inside the flow flied. From the energy point of view, the increase in total pressure is because the flow in this stream is energized by the adjacent stream even if it has not been energized by the propeller yet. The average difference in static pressure between the two sides of the propeller is 5 Pa. It looks negligible in the figure due to axis scaling effects. We can also see that behind the propeller (x = 100 mm), the static pressure increases gradually. This is because the flow is decelerating due to the presence of the fairing in the back. The total pressure drop between x = -100 mm and x = 50 mm can be explained by the friction and shear stress by the spinner, blade and tube. The most important criteria was to eliminate the static pressure term. In Fig. 7-3, it can be seen clearly that the static pressure is stabilized at x-coordinate x = -100 mm. This means that the pressure changing effect caused by the body is minimized at this distance. Which makes it a suitable coordinate to position the propulsor.

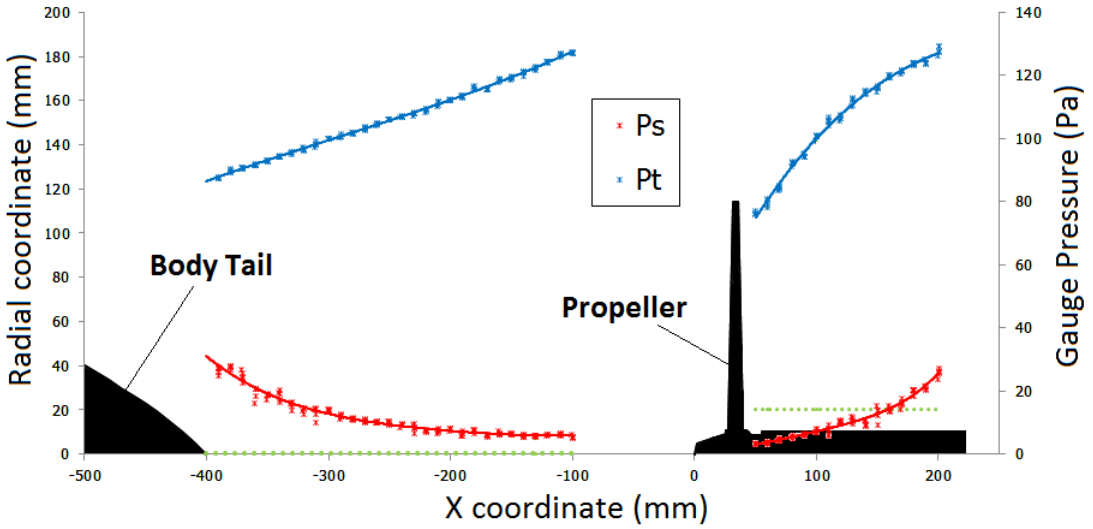

Figure 7-3: Pressure Survey Before and After Propulsor in WI Configuration

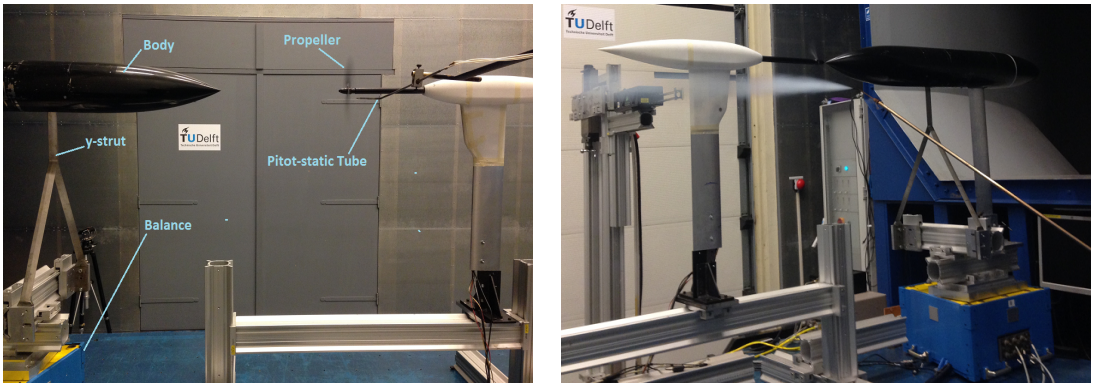

(a) WI Configuration with Pitot-Static Tube (b) BLI Configuration with Smoke Tube

Figure 7-4: Photograph of WI and BLI Configuration

For the BLI configuration depicted in Fig. 7-4(b) the propulsor is placed as close as possible to the trailing edge of the body in order to capture the Boundary Layer (BL). The photograph illustrated in Fig. 7-4(b) is taken during a visualization procedure of the flow around the body using smoke.
For both configurations, WI and BLI, 'Equilibrium' and 'Constant Speed' settings are practiced. In this prospect, free-stream, WI and BLI configurations are equal. However, there exists a major difference in the calculation of the body drag. For the free-stream propulsor case, explained in Sec. 7-3, the drag of the (fictitious) body is calculated using the relation between Re and Cd found in the isolated body configuration. But since the body is present for WI and BLI configurations, the actual real time total drag (body + strut) can be measured. However, the problem exists that the strut drag needs to be subtracted in order to get the body drag. Thus for these configurations (WI and BLI) it is chosen to measure the real time total drag of the body and subtract the calculated strut drag derived using the isolated body configuration.

7-5 PIV Implementation

The tracer particles were produced by a SAFEX twin fog generator placed downstream of the rotor. This generator produces Diethyl glycol-based seeding particles of 1 μm median diameter with a relaxation time of less than 1 μs. Uniform mixing in the test section was ensured by the wind-tunnel closed loop.
A Quantel Evergreen double pulsed Nd:YAG laser system was used as the light source. With the emitting power of 200 mJ per pulse, this system provides green light of wavelength 532 nm creating laser sheet of approximately 2 mm width and 40×30 cm^2 illuminating area. The pulsed laser energy, repetition rate and time delay between pulses were controlled by a Processing Time Unit (PTU) and a synchronization box called the Standford box.
Two LaVision Imager pro LX 16M cameras were used for image acquisition. The cameras have a resolution of 4870×3246 pixels with the pixel size of 7.4×7.4 μm^2. Each camera was equipped with a Nikon lens with focal length varying with desired Field of View (FOV) and image resolution. Camera acquisition was synchronized to the laser shooting using the DaVis acquisition software.[12]

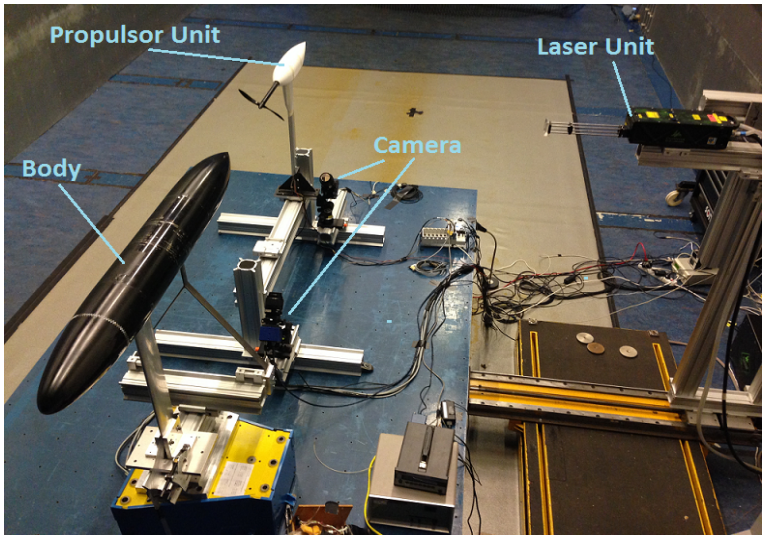

Figure 7-5: Photograph of the PIV Setup for WI Configuration

7-5-1 PIV Setup

To keep this section concise PIV setup for WI configuration is treated only. Remember that PIV is applied for WI as well as freestream and BLI configurations. For all of these configurations, the same plane (illustrated in Fig. 5-2) is measured under identical 'constant speed' setting. This plane is chosen such that the momentum in front of the propeller and aft of the propeller is captured. Only half of the propeller plane is scanned because symmetric flow properties is assumed. This can be assumed because the body is symmetrical and the struts have negligible effect on disturbing symmetric flow properties. This is checked using a visualization of the shear layer after the body using tufts.
Note that scanning half of the propeller plane requires integration over 360 degrees rotation to capture the entire propeller performance. In Fig. 7-5, the PIV setup for WI configuration can be found. Two 16M cameras aimed at the propeller can be seen. The actual plane that is captured by these cameras can be found in Fig. 5-2. Also, the Quantel laser (far right) positioned on top of a beam aimed to the measurement plane can be observed.

Chapter 8

Data Processing

Data obtained from the experiment requires processing. Processing the data started early during the experiment for computing the pure body drag for the isolated body configuration. These on-site computations of the airframe drag was unfortunately subject to errors. These errors were discovered during post-processing. The origin and consequences of these mistakes are explained in Sec. 8-1. This is followed by an error analysis mainly focused on deleting outliers (Sec. 8-2) and an uncertainty analysis (Sec. 8-3) as part of the post-processing. It is important not to confuse error with uncertainty in this stage. Error is the difference between the measured value and the 'true value' of the thing being measured. Uncertainty is a quantification of the doubt about the measurement result.[7]

8-1 Airframe Drag

The sole purpose of the isolated body configuration, introduced in Sec. 7-2, is obtaining the pure body drag. This body drag is required to tune the propulsor thrust into equilibrium setting, meaning that the propulsor needs to generate a thrust equal to the pure body drag. This section deals with the approach of obtaining this pure body drag and the mistakes accompanied with it.

First, the isolated body with struts is placed in the wind-tunnel. For the 'equilibrium' setting, introduced in Sec. 7-1, it is required to vary wind-tunnel settings ranging from 5 to 26 m/s. For this entire wind-speed range, the drag is measured and stored (See Fig. 8-1(a)). Then, the body is detached leaving only the struts (See Fig. 7-1(b)). This strut-only configuration is measured in identical wind-tunnel settings (See Fig. 8-1(b)).
Observing Fig. 8-1 it can be seen that the obtained drag measurements show an increase in drag for increasing Reynolds Number (Re). Note that the data is grouped around certain Re ranges. This is because the measurements are conducted at predefined wind-speed settings highlighted earlier in Table 7-1. In the graphs a polynomial fitting curve can be found with the accompanying formula. The x parameter is automatically generated inside Excel which needs to be interpreted according to the x-axis parameter which is the Re in this case. The same holds for the y-parameter which corresponds to the y-axis parameter, C_d in this case. These fitting curves are accompanied by a new parameter called coefficient of determination (R^2). This parameter describes the goodness of fit of a statistical model meaning that it shows how 'good' the data is represented by the curve. Or differently put, how well this

curve explains the measured scattered data. The coefficient of determination is a commonly used parameter in statistics and financial models. In this stage it is sufficient to understand that R^2 equal to 1 means that every observed/measured point is perfectly described by the estimated fitted curve and that R^2 equal to 0 means that the fitted curve is useless. Thus it is desired to have a coefficient of determination close to unity which is the case for the polynomials illustrated in Fig. 8-1.

Although the wind-tunnel setting is identical for both configurations (body+strut and strut-only) a difference in velocity, temperature and pressure still remains. In order to capture the differences that exist in dynamic pressure (q), the dimensionless drag coefficient (C_d) is used instead of the measured drag (Eqn. 8-1). To capture the differences that exist between the measurements in wind-speed (v), density (ρ) and dynamic viscosity (μ) the Re is used (Eqn. 8-2). In order to compute the pure body drag a subtraction operation is required between body+strut and strut-only configured C_d functions.

$$C_d = \frac{D}{q \times s} \tag{8-1}$$

$$R_e = \frac{\rho \times v \times L}{\mu} \tag{8-2}$$

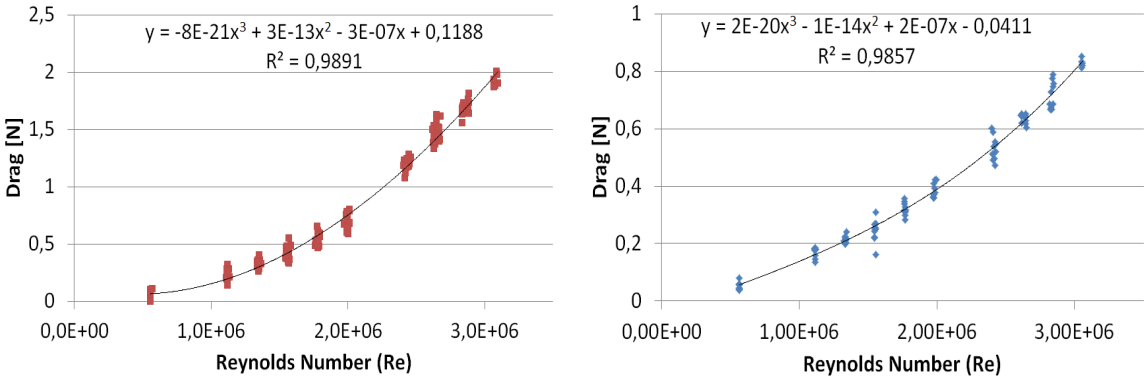

(a) Body + Strut Drag Measurement Result

(b) Strut Drag Measurement Result

Figure 8-1: Drag Measurement Results for Isolated Body Configuration

For both configurations, illustrated in Fig. 7-1, the C_d versus Re is computed. First these curves are generated separately and then subtracted using Eqn. 8-3. Two general methods exist in applying Eqn. 8-3; cloud based- and cycle based subtraction. The cloud based computation method is simply generating one C_d-function for both configurations using the entire data cloud. This method uses the entire data cloud without filtering or assessing the quality of the obtained measurements. This approach poses problems which can be clearly seen in Fig. 8-2(a). Simply by observing the data a large scatter can be noticed for Re values around 500,000 representing a wind-speed of 5m/s. This scatter is caused by the uncertainty that exists for the dynamic pressure (q) at that Re range. This can be understood when realizing that the scatter in drag is constant for the entire Re range (See Fig. 8-1). Observing a R^2 value of 0.1644 in Fig. 8-2(a) gives a more quantitative grip on this matter. Because it actually means that the generated fitting curve very poorly predicts/describes the data. Thus it would be very ignorant to subtract the fitted curve found in Fig. 8-2(b) from the

poorly fitted curve in Fig. 8-2(a). This is the main reason why the cloud based subtraction is not applied. Instead a more rigorous method is used, the cycle based subtraction.

$$C_{d_{(Body)}} = C_{d_{(Body+Strut)}} - C_{d_{(Strut)}} \qquad \text{where} \qquad C_d = f(R_e) \tag{8-3}$$

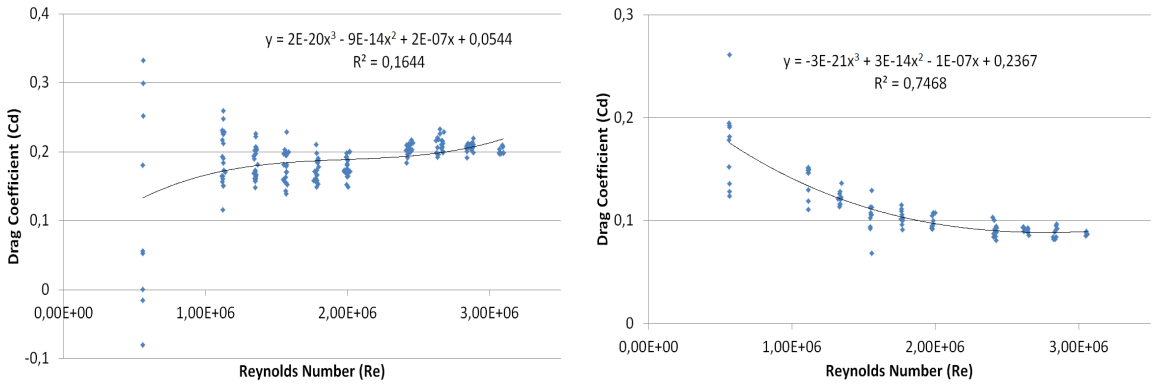

(a) Body + Strut Drag Coefficient

(b) Strut Drag Coefficient

Figure 8-2: Drag Coefficient vs. Reynolds Number for Isolated Body Configuration

The cycle based subtraction is, as the name might suggest, assessing a curve for each cycle. One cycle consists of the wind-tunnel speed varying from 5 to 26 m/s and back. Each cycle curve is generated and then evaluated using its R^2 value. If this value is higher than 0.8 the fitted curve is regarded as sufficiently describing the data. The fitted curves that have values below 0.8 are disregarded. These fitted curves can be found in the Appendix, specifically in Ch. E where these are plotted in Fig. E-2. Using the R^2 requirement, Fig. E-2(b), E-2(d), E-2(e) and E-2(f) are omitted. Using this method the properly conducted cycles are used and poorly executed cycles omitted from the body drag calculation. After this filtering process, the usable fitted curves are averaged. This is implemented by taking the average of each parameter inside the fitted curve (see Eqn. 8-4 and 8-5).
This process is also applied for the strut-only configuration. The results for the strut-only configuration and accompanied fitting curves with their coefficient of determination values can be found in Fig. E-1. It can be seen that fitted curves in Fig. E-1(c) and E-1(d) have R^2 values below 0.8 which are therefore omitted from the calculation process. The same averaging process (similar to Eqn. 8-5) is applied for the three remaining curves corresponding to the strut-only configuration.

$$\begin{aligned}
C_{d_{(Cycle-1)}} &= A_1x^3 + B_1x^2 + C_1x + D_1 \\
C_{d_{(Cycle-3)}} &= A_3x^3 + B_3x^2 + C_3x + D_3 \\
C_{d_{(Cycle-6)}} &= A_6x^3 + B_6x^2 + C_6x + D_6 \\
C_{d_{(Cycle-8)}} &= A_8x^3 + B_8x^2 + C_8x + D_8 \\
C_{d_{(Cycle-9)}} &= A_9x^3 + B_9x^2 + C_9x + D_9 \\
C_{d_{(Cycle-10)}} &= A_{10}x^3 + B_{10}x^2 + C_{10}x + D_{10}
\end{aligned} \tag{8-4}$$

$$\begin{aligned}
C_{d_{(Average)}} = &\left(\frac{A_1 + A_3 + A_6 + A_8 + A_9 + A_{10}}{6}\right)x^3 + \left(\frac{B_1 + B_3 + B_6 + B_8 + B_9 + B_{10}}{6}\right)x^2 \\
&+ \left(\frac{C_1 + C_3 + C_6 + C_8 + C_9 + C_{10}}{6}\right)x + \frac{D_1 + D_3 + D_6 + D_8 + D_9 + D_{10}}{6}
\end{aligned} \tag{8-5}$$

This averaging process results in Eqn. 8-6a and 8-6b for strut+body and strut-only configuration respectively. These equations are subtracted in the manner depicted in Eqn. 8-3 to get the final equation that purely describes the body drag without the struts. The result of this subtraction can be found in Eqn. 8-7. Note that this equation describes the pure body drag as a function of the Re.

$$C_{d_{(Body+Strut)}} = -7.5 \times 10^{-20} Re^3 + 4 \times 10^{-13} Re^2 - 6.5 \times 10^{-7} Re + 0.5049 \tag{8-6a}$$

$$C_{d_{(Strut)}} = -1.02333 \times 10^{-20} Re^3 + 6.66667 \times 10^{-14} Re^2 - 2 \times 10^{-7} Re + 0.2996667 \tag{8-6b}$$

The $C_{d_{(Body)}}$ function in Eqn. 8-7 is used to establish the 'equilibrium' setting. This is performed by integrating this function inside the Labview software. It is integrated in such a way that the pure body drag is calculated in real-time with wind-tunnel settings as input. This enables the adjustment of propulsor thrust to the body drag without the body being present. Meaning that the monitor in the wind-tunnel provides the drag of the body as if the body is present in that wind-tunnel environment. The thrust can then be adjusted, by changing the Rotations Per Minute (RPM) setting, to the 'fictitious' body drag. This approach is taken for the free-stream propulsor configuration (See Fig. 7-2) because here the body is not present.

$$C_{d_{(Body)}} = -6.476667 \times 10^{-20} Re^3 + 3.333333 \times 10^{-13} Re^2 - 4.5 \times 10^{-7} Re + 0.205233 \tag{8-7}$$

For the remaining configurations, Wake Ingestion (WI) and Boundary Layer Ingestion (BLI), a slightly different approach is taken. Since in these configurations the body is actually present and measurable, the total real-time drag measurements are used. Because the strut drag needs to be subtracted from these measurements (to get the pure body drag), the $C_{d_{(Strut)}}$ is used. Thus the main difference that exists is the fact that instead of the $C_{d_{(Body)}}$, the $C_{d_{(Strut)}}$ is used. For clarification purposes the real-time equation used to compute the pure body drag is provided for free-stream (Eqn. 8-8), WI and BLI configuration (Eqn. 8-9). Note that the $D_{Body+Strut}$ term is real time measured by the presence of the body for WI and BLI configurations and that the C_d values are calculated using the Re which is directly computed from wind-tunnel settings.

$$D_{Body} = C_{d_{Body}} \times q \times S \tag{8-8}$$

$$D_{Body} = (D_{Body+Strut}) - (C_{d_{Strut}} \times q \times S) \tag{8-9}$$

Remember that the entire purpose of obtaining the pure body drag is to aim for an 'equilibrium' setting where the propulsor thrust equals the pure body drag. So when plotting the pure body drag of the isolated body and plotting the free-stream propulsor thrust they need to be equal. In order to check this requirement Fig. 8-3 is plotted. Observing the figure it can be seen that the thrust setting for free-stream, WI and BLI differs significantly from the drag of the isolated body. It seems that the thrust setting for free-stream, WI and BLI is too large compared to the isolated drag configuration. Thus Fig. 8-3 shows clearly that 'equilibrium' setting is unfortunately not satisfied.

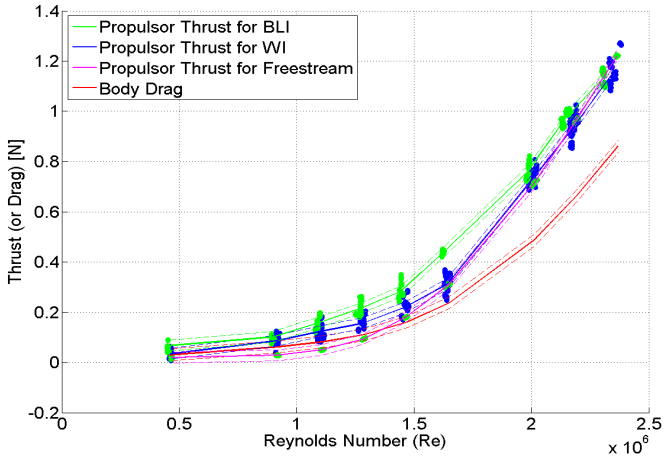

Figure 8-3: Thrust and Drag vs. Re for Every Configuration

The reason for this is found in rounding errors originated from the fitted curves for $C_{d_{(Body+Strut)}}$ and $C_{d_{(Strut)}}$ generated in Excel software. During post-processing the same calculations are reapplied to obtain the $C_{d_{(Body)}}$ curve. By doing so, the curves for $C_{d_{(Body+Strut)}}$ and $C_{d_{(Strut)}}$ are found to be different than the ones that are used during the experiments. This difference is illustrated in Fig. 8-4(a) and 8-4(b).

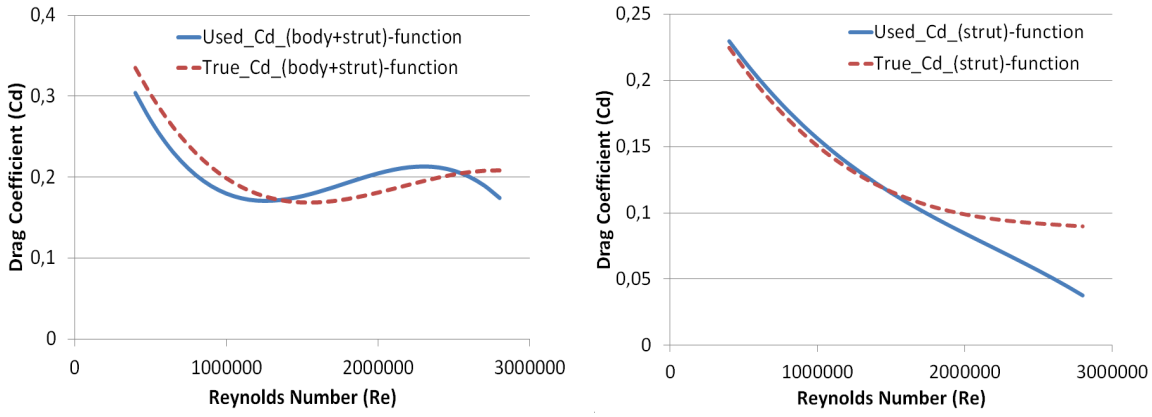

(a) Body + Strut Drag Coefficient

(b) Strut Drag Coefficient

Figure 8-4: Used- and True Drag Coefficient Curve for Isolated Body Configuration

The consequence of using the wrong $C_{d_{(Body+Strut)}}$ and $C_{d_{(Strut)}}$ curve is directly magnified for the $C_{d_{(Body)}}$ curve due to the subtraction operation. Figure 8-5 illustrates the difference between the used (wrong) $C_{d_{(Body)}}$ curve and the true curve computed during post-processing.

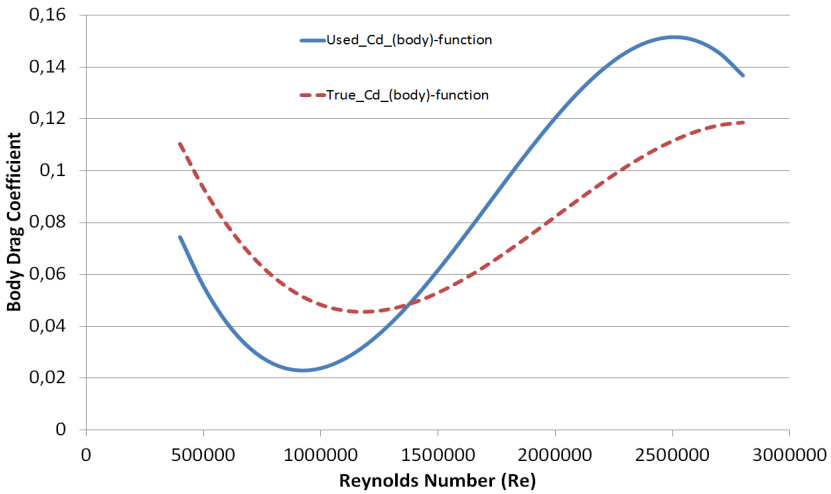

Figure 8-5: Used- and True Body Drag Coefficient Curve for Isolated Body Configuration

Remember that $C_{d_{(Body)}}$ is used to manage equilibrium setting for free-stream propulsor configuration. The $C_{d_{(Strut)}}$ is used for WI and BLI configurations. Correction is useless, because these curves are used to set the thrust for equilibrium setting. The real thrust is already computed and visualized in Fig. 8-3. In order to perform damage assessment, the net-force can be computed (see Fig. 8-6). The blue lines are the curves generated using the wrong $C_{d_{(Body)}}$ and $C_{d_{(Strut)}}$ function. These lines follow the equilibrium setting nicely because a net-force of zero is almost achieved. It can be seen however, when observing these blue lines, that for BLI configuration equilibrium is poorly satisfied. This can be the case when the experiment is simply poorly executed, meaning that the propulsor thrust is not perfectly aligned with the calculated body drag. A possible reason for this, according to the author, can be the close interaction effect that exists between propulsor and body for this configuration. Because when increasing the propulsor thrust, the drag of the body increases with it (for the same wind-speed setting) due to the suction effect the propulsor causes on the body. This causes the body to see a higher velocity locally hence increasing its drag. Which requires the increase of thrust setting again to balance the instantaneous drag of the body. These small-scale effects cause a large equilibrium settling time during the experiment and larger thrust settings for the same wind-tunnel setting. This explanation is also supported by Fig. 8-3, where larger thrust settings can be found for BLI w.r.t. free-stream and WI configurations.

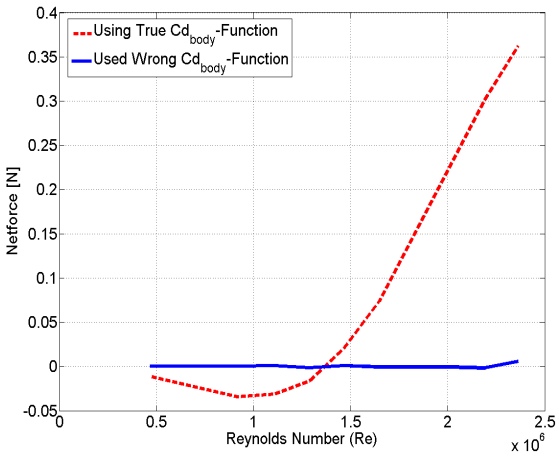

(a) Net-force Free-stream Propulsor Configuration

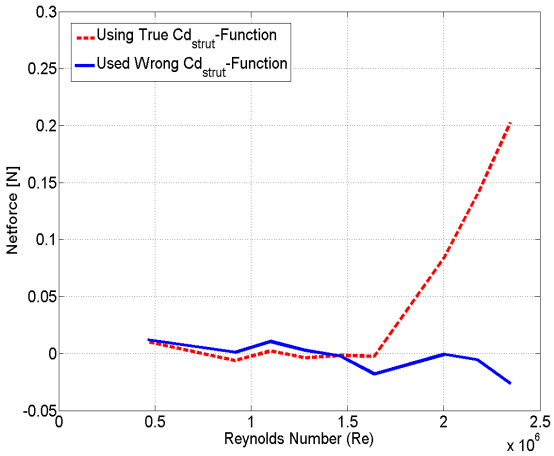

(b) Net-force WI Configuration

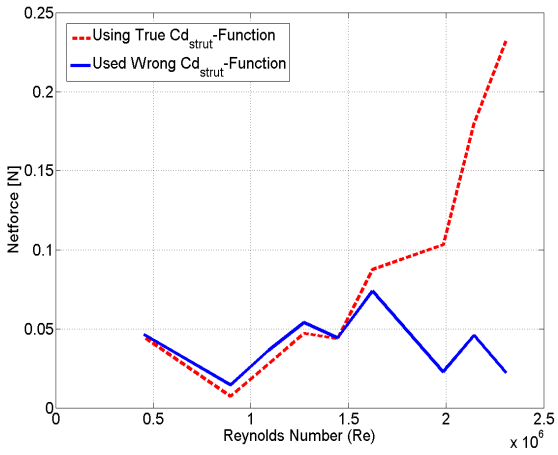

(c) Net-force BLI Configuration

Figure 8-6: Equilibrium Setting for All Configurations

Figure 8-6 illustrates the real net-force (in green) obtained by using the correct $C_{d_{(Body)}}$ and $C_{d_{(Strut)}}$ function found during post-processing. It shows that for the free-stream propulsor configuration (Fig. 8-6(a)) equilibrium setting is certainly not satisfied. The same holds for WI and BLI configurations illustrated in Fig. 8-6(b) and 8-6(c) respectively. Although equilibrium is not satisfied the author has tried to use this data anyway. In order to asses whether this data can be used, all three of the configurations with their respective net-force condition are plotted in Fig. 8-7.

Here it can be seen that the free-stream configuration shows significant differences between WI and BLI configurations. The net-force starts lower and ends significantly higher for larger Re. This is probably caused because of the difference in computation that exist between these configurations, namely that free-stream computes the drag differently than WI and BLI does. This difference is already explained using Eqns. 8-8 and 8-9. Instead of omitting all the data obtained from 'equilibrium' setting, it is decided to use the data obtained from WI and BLI configurations for comparison reasons. This is because WI and BLI curves follow approximately the same wrong net-force setting which can be observed in Fig. 8-7. Thus a comparison between WI and BLI in terms of performance for equilibrium setting is possible. These results can be found in Sec. 9-2.

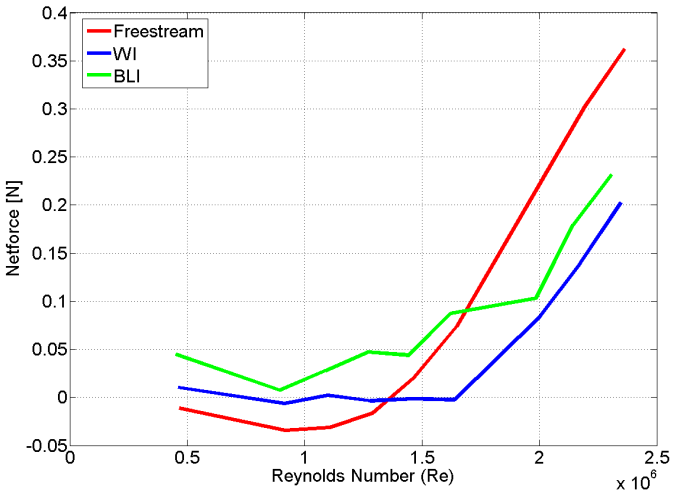

Figure 8-7: True Net-force for All Configurations

8-2 Error Analysis

Error is defined as the difference between the measured value and the 'true value'. In experiments however, the true value can never be found. By repeating the measurement, confidence is built in acquiring the 'true value'. This is because random errors in the form of outliers are identified. However, systematic errors that cause some sort of biasing can not be captured by simply repeating the experiment over and over again. This is why the uncertainty of the measuring device is computed using calibration. This uncertainty is then propagated inside the equations to be able to confine the measurement in a range of uncertainty. In this concise section, random errors in the form of outliers are identified and deleted. This is followed by an uncertainty analysis (Sec. 8-3) in which the uncertainty obtained from calibration is propagated inside calculations.

In Sec. 8-1 the coefficient of determination (R^2) was introduced. This parameter is very sensitive to outliers. An outlier is usually defined as an observation that is well outside of the expected range of values in a study or experiment. There is no rigid mathematical definition of what actually defines 'well outside'. Determining whether or not an observation is an outlier is ultimately a subjective exercise. Outlier detection can be visual or model-based. Model-based methods assume that the data are from a normal distribution, and identify observations which are deemed "unlikely" based on mean and standard deviation. The methods that use this principle are Chauvenet's criterion and Grubbs' test for example.

The author decided to use an outlier detection method that is more visual. Meaning that an outlier is defined when a measurement lies far outside the measurement expectancy without calculations. This method is very easy to carry out but also very subjective.

The experiment is conducted in two different settings, 'constant speed' and 'equilibrium', which requires a separate treatment to keep it clear and transparent. During the experiments a signal loss of the propulsor RPM was observed. The signal loss constitutes in lost RPM counts which is the main problem present in the data. The remaining data, captured by the load cell and torque sensor, seems sufficiently accurate. This is the reason why outliers caused by RPM signal loss is treated in this section only.

8-2-1 RPM Outlier Detection for 'Constant Speed' Setting

For the 'constant speed' setting, the data is first investigated cycle based. This is because, in the 'constant speed' setting ,the wind-tunnel is set at 26 m/s and the propulsor thrust is increased and decreased gradually throughout the duration of the experiment. In order to detect RPM outliers for this configuration, plots in the form depicted in Fig. 8-8 is required. In this figure, a proper cycle (Fig. 8-8(a)) and a cycle with three outliers (Fig. 8-8(b)) is illustrated. In the figure it can be seen clearly that RPM is increased and decreased gradually.

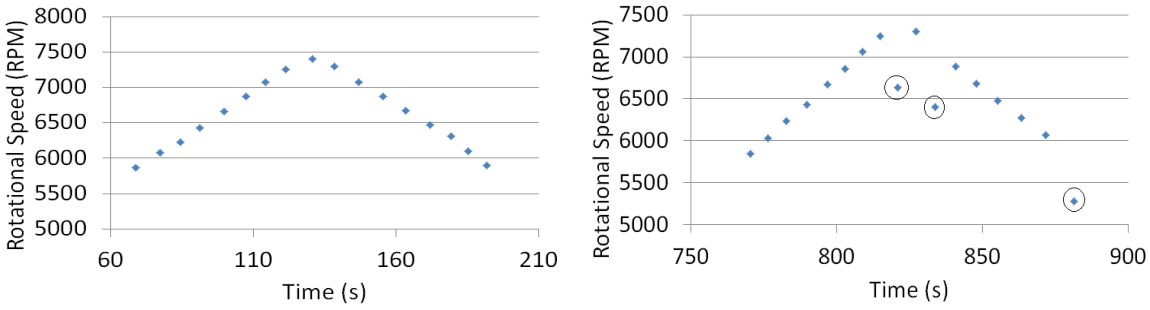

(a) Proper Cycle in Constant Speed Setting

(b) Cycle with Three RPM Outliers

Figure 8-8: Detect Cycle Based RPM Outliers for Free-stream Configuration in 'Constant Speed' Setting

Also cloud based investigation can be applied. Here the entire data cloud obtained during a configuration, free-stream propulsor in this case, is used to detect outliers visually. The data is grouped around certain regions, these regions correspond to the RPM step increase for 'constant speed' setting.

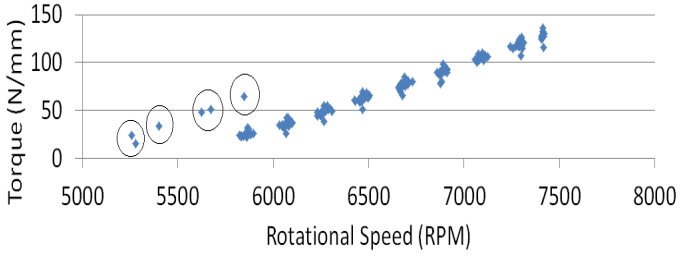

Figure 8-9: Detect Cloud Based RPM Outliers for Free-stream Configuration in 'Constant Speed' Setting

8-2-2 RPM Outlier Detection for 'Equilibrium' Setting

In the equilibrium setting the wind-speed is increased according to Table 7-1. When investigating RPM outliers for the 'equilibrium' setting, graphs can be plotted based on the wind-speed. In Fig. 8-10, the RPM signal losses can be clearly identified for 16 and 18 m/s. For example, if the RPM versus torque is plotted for the entire data cloud, Fig. 8-11(a) appears. At first sight it might look that the torque sensor is performing poorly because the data points do not follow a nice curved path and deviate at higher RPM counts. But this is not the case. Because when plotting wind-speed versus torque, see Fig. 8-11(b), the torque sensor performs properly since the data points follow a second order curve. This only leaves the RPM signal loss as the sole reason for the outliers that exist in Fig. 8-11(a). These outliers are of course deleted from the data.

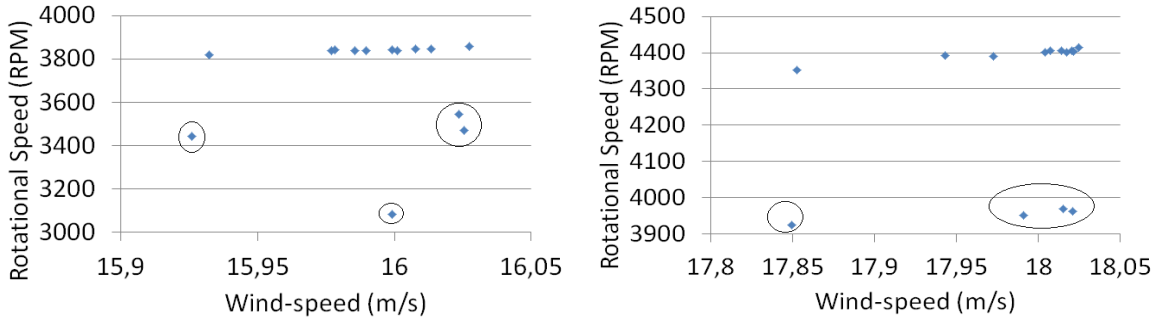

(a) RPM for 16m/s (b) RPM for 18m/s

Figure 8-10: RPM Outlier Detection using the Wind-speed

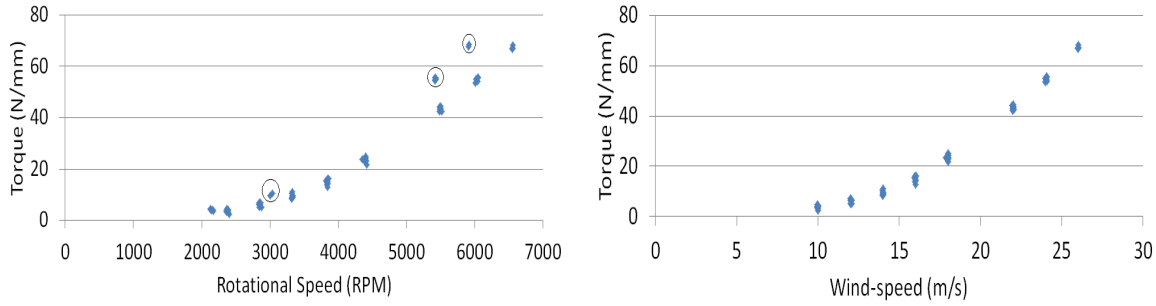

(a) RPM vs. Torque (b) Wind-speed vs. Torque

Figure 8-11: Cloud Based RPM Outlier Detection for 'Equilibrium' Setting

8-3 Uncertainty Analysis

This section deals with measurement uncertainty. First, the instrument uncertainty, expressed in the estimated Standard Deviation (SD) for the calibration curve, is obtained using calibration data in Sec. 8-3-1. Then the obtained SD's are propagated inside equations to the desired parameters in Sec. 8-3-2. Finally, some preliminary results regarding uncertainty distribution for certain parameters are provided in Sec. 8-3-3.

8-3-1 Instrument Uncertainty

Calibration of the balance, load cell and torque cell is introduced in Ch. 6. This section deals with the results that are found in these calibrations. The calibration process is performed by, roughly speaking, applying a regression through the data and obtaining the SD of this regression. The regression is applied using a linear function (see Eqn. 8-10). The SD of this regression curve is called the estimated standard deviation ($\hat{\sigma}$). Assuming the data is normally distributed, the estimated SD found from regression, which is automatically generated in Matlab, can be used to generate the confidence interval. A 95% confidence interval is chosen for post-processing the data. In Fig. 8-12 it can be seen that the estimated SD must be multiplied by two and added or subtracted from the mean observed value to build the confidence interval. This is what is being performed for plotting the results with 95% SD in the upcoming sections.

$$\hat{y} = \hat{a}x + \hat{b} \tag{8-10}$$

In Table 8-1 the $\hat{\sigma}$ for the balance (drag), load cell (thrust), torque sensor and wind-tunnel pressure can be found. Note that these values are simply obtained using the calibration curves provided in Fig. 6-11(b), 6-19(a) and 6-19(b) for drag, thrust and torque respectively. For the pressure, or delta P, the value depicted in Table. 8-1 is obtained by the combined effect of wind-tunnel calibration uncertainty plus digital pressure gauge uncertainty. The calibration data of the wind-tunnel, provided by Nando Timmers, gives an estimated SD of 0.314 Pa. However, in order to make the uncertainty more authentic, the digital pressure gauge SD is added using Eqn. 8-12. Since the digital pressure gauge has a measurement range between -1000 and 3500 Pa and a 0.03% full scale error, it gives an uncertainty of 1.05 Pa. This uncertainty is set by the author equaling to 1 SD. This value is typically chosen as a way of creating a situation in which the instrument precision is in a disadvantageous position. Meaning that the uncertainty of the instrument will produce results that lie in 68% of the observations. This means that a higher uncertainty will exist for the 95% confidence interval which is aimed for. Equaling the uncertainty to 1 SD thus actually is preventing an instrument from biasing towards precision. According to the author, this approach generates more realistic (higher) confidence levels. The uncertainty for the used encoder, which counts the revolutions of the motor, is found using Eqn. 8-11. Substituting encoder properties, which can be found in the product data sheet (not included in this report), in Eqn. 8-11 gives the uncertainty depicted in Table 8-1. Also in this case, the calculated uncertainty is set to 1 SD. The temperature sensor used in the wind-tunnel has a property of 0.1 K uncertainty. Again, this value is set as 1 SD which can be found in Table 8-1. Since the uncertainty, expressed in SD, of each measurement device is known it is time to propagate these uncertainties to the desired parameters. This is performed in Sec. 8-3-2.

$$uncertainty_{(RPM)} = (last\,adjustment\,time \times aging\,rate) + temperature\,effect + line\,voltage\,effect \tag{8-11}$$

Table 8-1: Calibration Regression Data

Parameter	$\hat{a}$	$\hat{b}$	R^2	$\hat{\sigma}$
Thrust [N]	1.022	-0.07556	0.9999	0.0107
Torque [N/m]	0.8656	−0.001387	0.9992	0.0008936
Drag [N]	1.008	−0.003371	0.9999	0.0076
Pressure [Pa]	1.272	−0.01817	1.0000	1.1046
Revolutions [RPM]				1.5470E-07
Temperature [K]				0.1

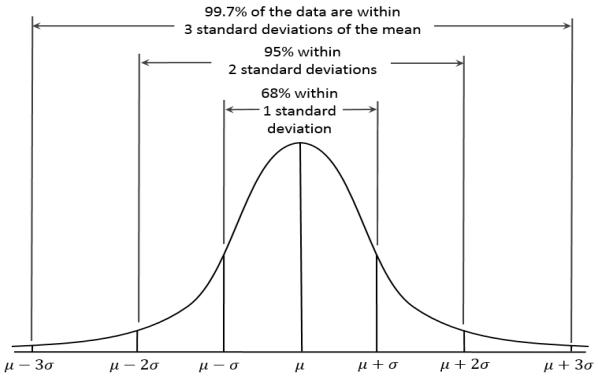

Figure 8-12: Confidence Interval using Normal Distribution[5]

$$\hat{\sigma}^2_{pressure} = \hat{\sigma}^2_{calibration} + \hat{\sigma}^2_{gauge} = 0.314^2 + 1.05^2 \tag{8-12}$$

8-3-2 Uncertainty Propagation

There exists basic uncertainty propagation rules in mathematics which can be found in Eqn. 8-13. The propagation strongly depends on the relation between the measurements whether they are independent or not. For the remainder of this section it is assumed that all the observations are independent, meaning they are uncorrelated. The consequence for the relations depicted in 8-13 is that the σ_{AB}-term, which is the cross-correlation term between the two parameters A and B, equals zero.

$$\sigma_f = a\sigma_A \qquad for \qquad f = aA \tag{8-13a}$$

$$\sigma_f = \left| \frac{fb\sigma_A}{A} \right| \qquad for \qquad f = aA^b \tag{8-13b}$$

$$\sigma_f = \sqrt{a^2\sigma_A^2 + b^2\sigma_B^2 + 2ab\sigma_{AB}} \qquad for \qquad f = aA + bB \tag{8-13c}$$

$$\sigma_f = \sqrt{a^2\sigma_A^2 + b^2\sigma_B^2 - 2ab\sigma_{AB}} \qquad for \qquad f = aA - bB \tag{8-13d}$$

$$\sigma_f = |f| \times \sqrt{\left(\frac{\sigma_A^2}{\overline{A}}\right)^2 + \left(\frac{\sigma_B^2}{\overline{B}}\right)^2 + 2 \times \frac{\sigma_{AB}}{\overline{AB}}} \qquad for \qquad f = AB \tag{8-13e}$$

$$\sigma_f = |f| \times \sqrt{\left(\frac{\sigma_A^2}{\overline{A}}\right)^2 + \left(\frac{\sigma_B^2}{\overline{B}}\right)^2 - 2 \times \frac{\sigma_{AB}}{\overline{AB}}} \qquad for \qquad f = \frac{A}{B} \tag{8-13f}$$

The equations stated above are used for uncertainty propagation. The specific equations that are applied for the parameters can be found in App. D. The relations for density, velocity, dynamic viscosity and Rotations per Second (RPS) can be found in Eqn. D-1a, D-1b, D-1c and D-1d respectively.

Note that the velocity is deduced from the dynamic pressure (delta P) measured in the wind-tunnel. Also, the density is calculated using the measured pressure and temperature multiplied with a reference value ratio. The dynamic viscosity is also a function of the temperature. The RPS is simply computed by dividing the RPM by 60.

The basic parameters provided in Eqn. D-1 are required for further calculations. Note that these parameters are shared variables computed in the wind-tunnel real time. The reference values and constants such as reference length (l) and frontal surface (S) are provided in Table. 8-2. Before proceeding to the uncertainty propagation, the relations used to compute each parameter are provided first in Eqn. D-2. Here the Re, advance ratio, shaft-power, thrust-power, propeller efficiency, shaft-power coefficient, thrust coefficient and drag coefficient can be found in Eqn. D-2a, D-2b, D-2c, D-2d, D-2e, D-2f and D-2g respectively.

Table 8-2: Reference Values used for Calculations

Parameter	Abbreviation	Value	Unit
Reference Length	l	1.385	m
Frontal Surface	S	0.0201	m^2
Density	ρ_o	1.225	$^{kg}/_{m^3}$
Pressure	p_o	101325	Pa
Temperature	T_o	288.15	K
Dyn. Viscosity	μ_o	1.7894×10^{-5}	Pa × s
Sutherland's Constant	C	110.4	K

The used uncertainty propagation relations can be found in Eqn. D-3. Here the uncertainty propagation for Re, advance ratio, shaft-power, thrust-power, propeller efficiency, shaft-power coefficient, thrust coefficient and drag coefficient can be found in Eqn. D-3a, D-3b, D-3c, D-3d, D-3e, D-3f and D-3g respectively. These relations are applied by first finding the SD's for density, velocity, dynamic viscosity, RPS and the product between dynamic pressure and velocity as intermediate steps. The uncertainties in SD for density, dynamic viscosity, RPS and dynamic pressure velocity product can be found in Eqn. D-4a, D-4b, D-4c and D-4d respectively. The SD for velocity requires two steps which can be found in Eqn. D-5. The SD's found in Eqn. D-3 and D-4 are used to build the 95% confidence interval (CI) using Eqn. D-6. Note that a bar on top of each parameter denotes the mean value.

8-3-3 Uncertainty Distribution

The confidence interval build using the SD's from the previous section gives an idea on how well the experimental observations must scatter inside a region of 95%. In Ch. 9 these confidence interval's are plotted along with the actual measurements. If the experimental observations are scattered within the calculated confidence interval it means that the experiment is conducted inside the expectations. This is also the reason why in Sec. 9-1 the raw direct measurements with their confidence intervals are plotted in order to see whether the experimental observations coincide with the calculated confidence interval.
In this concise section the uncertainty distribution is mapped. This is done in order to see the uncertainty proportion between the used instruments. This way the instrument that has a poor accuracy w.r.t. other instruments will stand out.

In Eqn. D-3 it can be noticed that the squared ratio's inside the squared roots give the interrelation that exists between the parameters. For example, if the squared ratio of one parameter is very high and the other low it means that the uncertainty of the combination of these is mainly governed by the parameter that has the larger squared ratio. Using this philosophy, the author has mapped the uncertainty distribution throughout the measured wind-speed regime for 'equilibrium' setting. The wind speeds that are measured in the 'equilibirium' setting can be found in Table 7-1. It is important to understand that the generated graphs are simply comparing the ratio $(\sigma_x/\overline{x})^2$ with $(\sigma_y/\overline{y})^2$ where x and y are parameters that match the parameter in question.

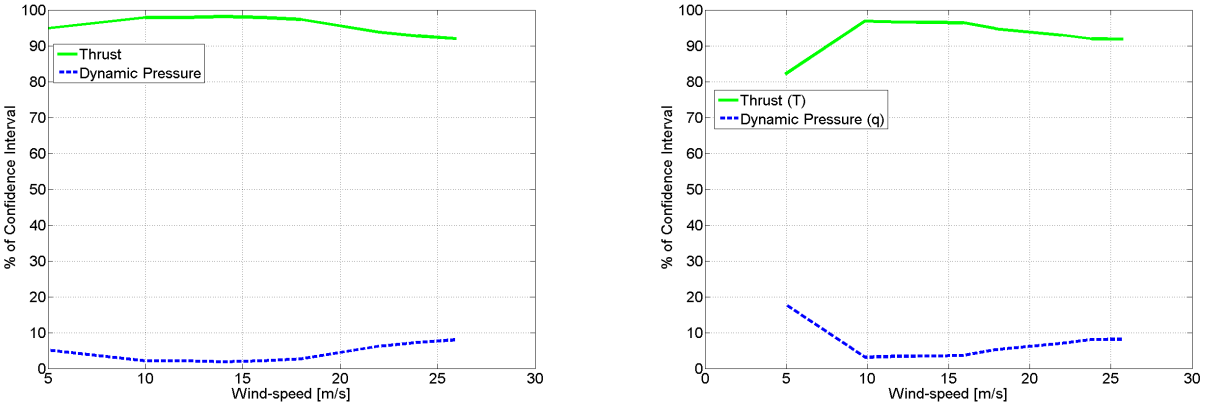

(a) Uncertainty Distribution for WI Configuration

(b) Uncertainty Distribution for BLI Configuration

Figure 8-13: Confidence Interval Distribution: Thrust Coefficient for WI and BLI Configuration

Figure 8-13 shows that the uncertainty for thrust coefficient is mainly dictated by the load cell uncertainty (thrust) for both configurations. The dynamic pressure uncertainty causes only 10% of the thrust coefficient uncertainty. The same principle holds for the shaft-power coefficient because Fig. 8-14 shows that the shaft-power is dominantly causing the uncertainty. The qv_∞-term, similar to the dynamic pressure in Fig. 8-13, is below 10% responsible for the uncertainty of the shaft-power coefficient.

The SD's which build the confidence interval for the propeller efficiency can be found in Eqn. D-3e. When plotting the uncertainty distribution in Fig. 8-15 it can be seen that the shaft-power uncertainty is more dominant. The shaft-power consists of torque multiplied with RPS. In order to see which of the two parameters is dominantly propagating to the propeller efficiency, Fig. 8-16 is plotted. Here it can be clearly seen that the shaft-power uncertainty is totally dictated by the torque sensor. The RPS uncertainty is negligibly small. The higher uncertainty for the torque is thus propagated to the shaft-power where it is visualized in Fig. 8-15. Observing Fig. 8-15 also shows that the thrust uncertainty becomes less influential for higher wind speeds in WI configuration.

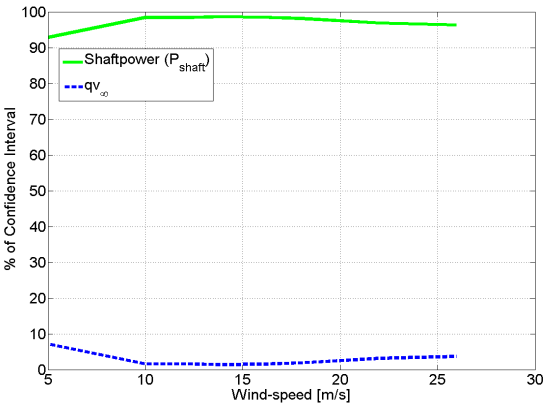

(a) Uncertainty Distribution for WI Configuration

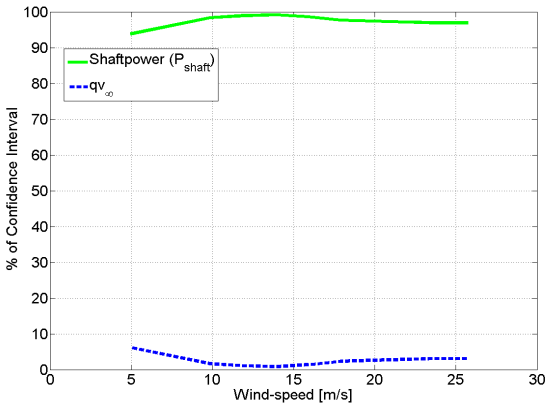

(b) Uncertainty Distribution for BLI Configuration

Figure 8-14: Confidence Interval Distribution: Shaft-power Coefficient for WI and BLI Configuration

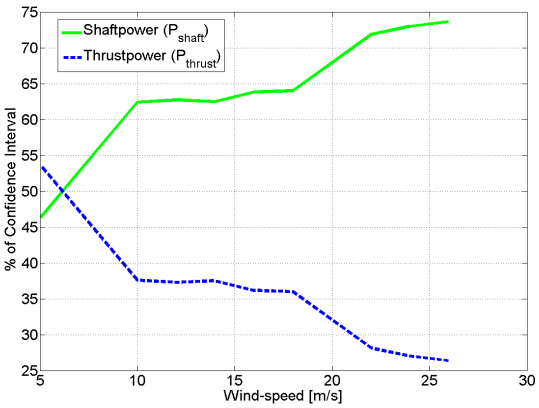

(a) Uncertainty Distribution for WI Configuration

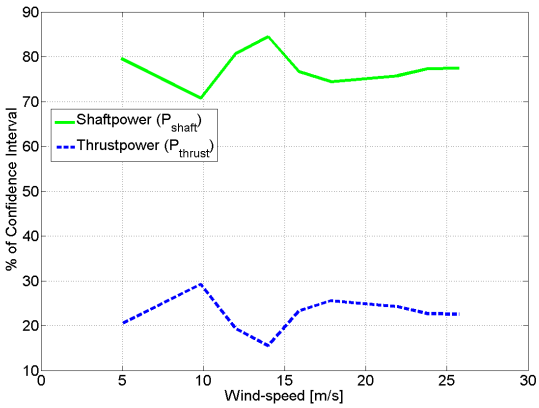

(b) Uncertainty Distribution for BLI Configuration

Figure 8-15: Confidence Interval Distribution: Propeller Efficiency for WI and BLI Configuration

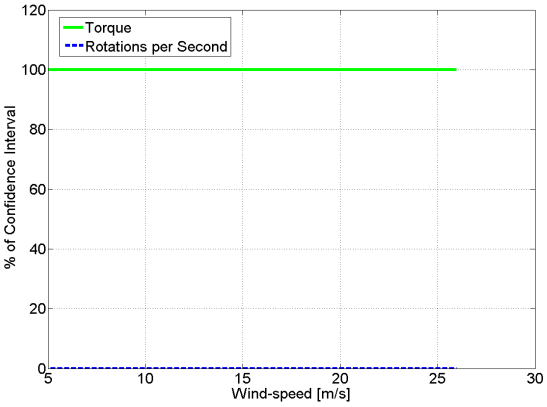

(a) Uncertainty Distribution for WI Configuration

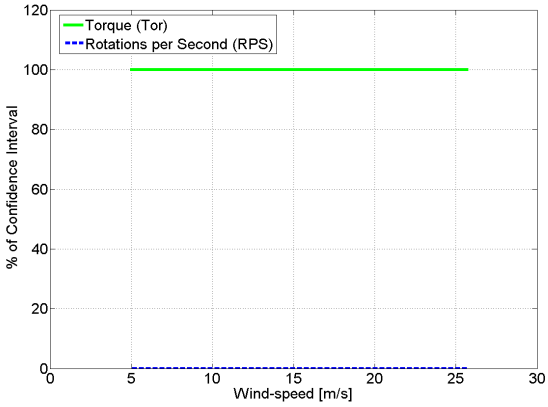

(b) Uncertainty Distribution for BLI Configuration

Figure 8-16: Confidence Interval Distribution: Shaft-power for WI and BLI Configuration

Chapter 9

Results

This chapter provides the results obtained from the wind-tunnel experiment. It is subdivided in four sections where first the raw measurements are plotted in Sec. 9-1. The description 'raw measurements' means that the direct measured values are plotted. This is done in order to show whether the measured observations lie within the calculated 95% confidence interval. This is followed by the results obtained from the 'equilibrium' setting tests in Sec. 9-2. Equilibrium setting refers to the state that the drag of the pure body equals the thrust of the propulsor for different wind-speed regimes. In Sec. 8-1 it is found that equilibrium is not satisfied due to calculation mistakes made during wind-tunnel testing. Thus it is chosen to omit the results obtained for free-stream propulsor configuration completely and only use Wake Ingestion (WI) and Boundary Layer Ingestion (BLI) configurations for comparison reasons. For an extensive discussion on this topic, see Sec. 8-1. The wind-tunnel experiments also covered a different setting, namely the so called 'constant speed' setting. Here the wind-tunnel is set at 26 m/s and the thrust is varied by manually changing the Rotations Per Minute (RPM) setting of the propulsor. The results obtained for this setting can be found in Sec. 9-3. Finally, the results obtained for Particle Image Velocimetry (PIV) are discussed in Sec. 9-4.

9-1 Raw Measurements

Fig. 9-1 shows the measurements obtained for the balance. The configurations in which these measurements are made can be visualized in Fig. 7-1. When Fig. 9-1 is carefully examined it can be seen that the calculated confidence interval, using balance calibration data, is too narrow. Differently formulated, the actual drag measurements lie for a large portion outside the 95% confidence interval. In order to understand this phenomenon it must be realized that the confidence interval is calculated using calibration data which is generated in near perfect conditions. The actual wind-tunnel environment causes strong vibrations on the balance which causes more scattered data increasing the uncertainty of the balance. These vibrations could also be experienced on-site, during the wind-tunnel tests, by watching the monitor showing drag fluctuations.

Figure 9-1 shows an exponential increase in drag for a linear increase in Reynolds Number (Re). This can be explained by simply checking the relation between drag (D) and velocity (see Eqn. 9-1). Here it can be seen that for a constant density (ρ), frontal surface area (S) and drag coefficient (C_d) the drag increases with the square of the velocity. The Re in the x-axis can be regarded as the velocity because the density, dynamic viscosity (μ) and characteristic length (l) of the body remain constant.

$$D = \frac{1}{2}\rho V^2 C_d S \tag{9-1}$$

Figure 9-2 shows the thrust measurements for WI and BLI configurations with the calculated 95% confidence interval. A similar exponential increasing pattern can be observed for the thrust. This is because the thrust is set to follow the drag to meet the equilibrium condition. It can be seen that the measurements are slightly more scattered w.r.t. the predicted confidence interval. It can be concluded that the load cell embedded inside the propulsor is capturing the force sufficiently accurate, especially for the BLI configuration illustrated in Fig. 9-2(b).

The same plot can be found for the torque in Fig. 9-3. In Sec. 8-3-3 it was concluded that the torque sensor accuracy is poor compared to the thrust sensor which therefore dominates the uncertainty present for the propeller efficiency. But when observing the torque uncertainty in Fig. 9-3 it can be seen that the observations are scattered according to the calculated confidence interval. This means that the confidence interval, calculated using calibration data, represents the uncertainty for the torque well.

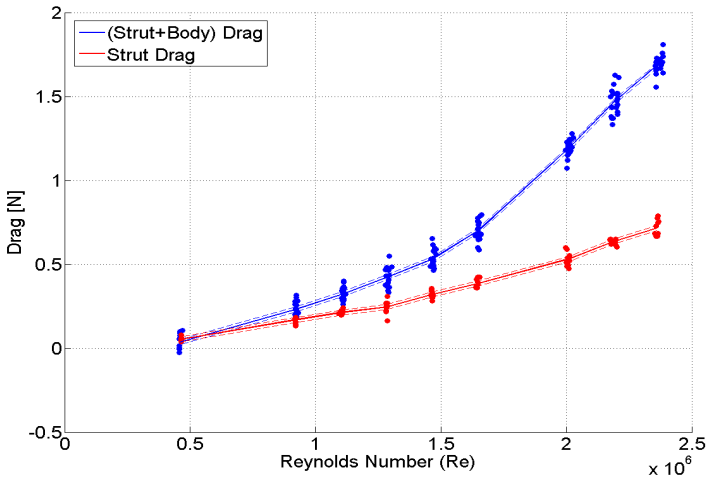

Figure 9-1: Drag Measured for Body-Configurations with 95% Confidence Interval

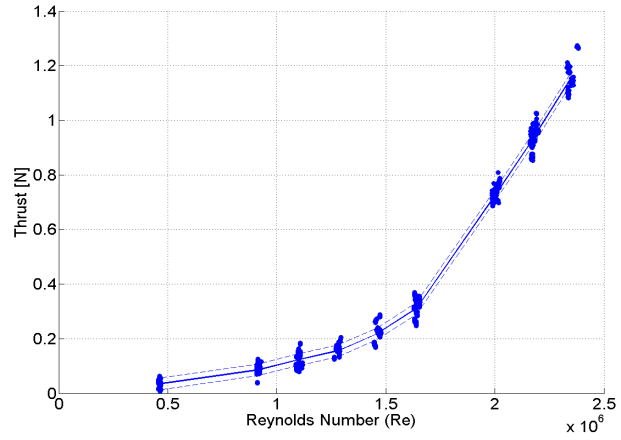

(a) Thrust for WI Configuration

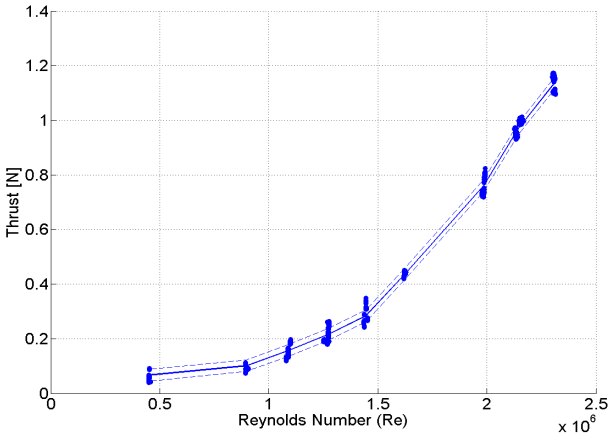

(b) Thrust for BLI Configuration

Figure 9-2: Thrust Measured for WI and BLI Configuration with 95% Confidence Interval

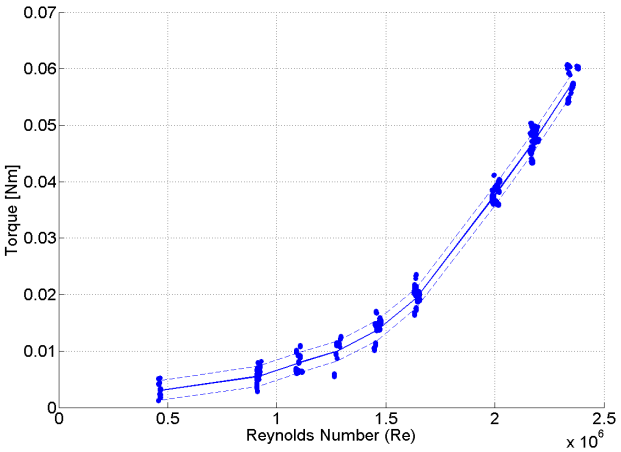

(a) Torque for WI Configuration

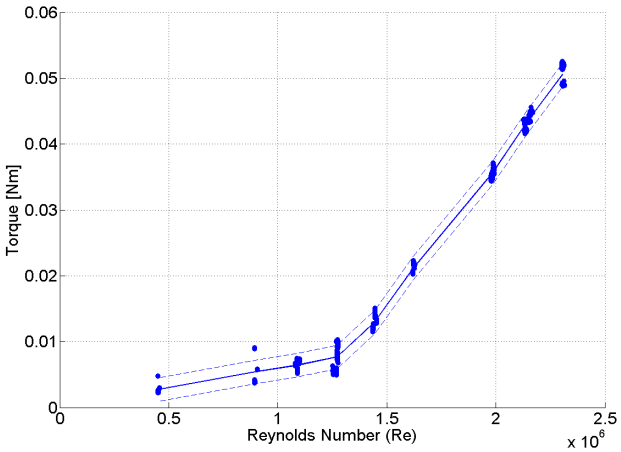

(b) Torque for BLI Configuration

Figure 9-3: Torque Measured for WI and BLI Configuration with 95% Confidence Interval

9-2 Equilibrium Setting Results

In this section the processed results for equilibrium setting can be found. First the drag coefficient for the isolated body configuration is provided in Fig. 9-4. Then a comparison between WI and BLI configuration is illustrated by embedding these into one figure.

Figure 9-4 shows three curves for the drag coefficient. The strut+body and strut-only configuration are illustrated in blue an green respectively. For a visualization of the isolated body setup, see Fig. 7-1. These two curves stand out for the presence of their actual measurement points scattered in the graph. In Fig. 9-1 it could be seen that drag measurements are more scattered w.r.t. the calculated confidence interval, the same holds for the drag coefficient in Fig. 9-4 because of the propagation rules explained earlier in Sec. 8-3-2 of course. Figure 9-4 also shows the body drag coefficient depicted in red. Note that this curve is calculated

using a subtraction process quantified in Eqn. 8-3 meaning that physically no measurements are possible, hence no dots are present.

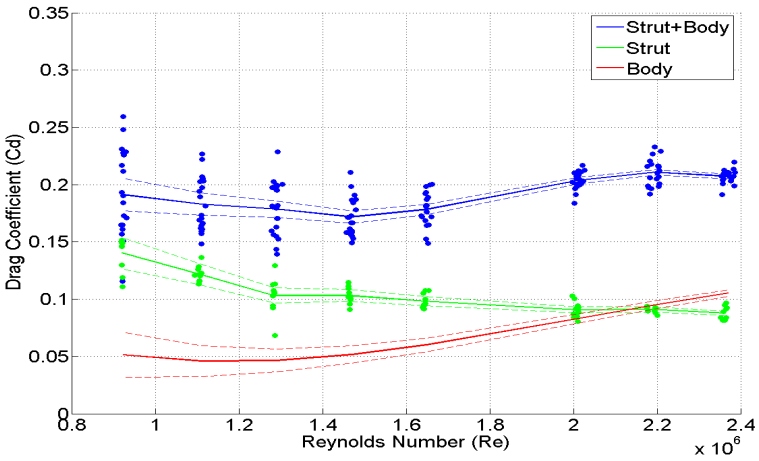

Figure 9-4: Drag Coefficient Measured for Body-Configurations with 95% Confidence Interval

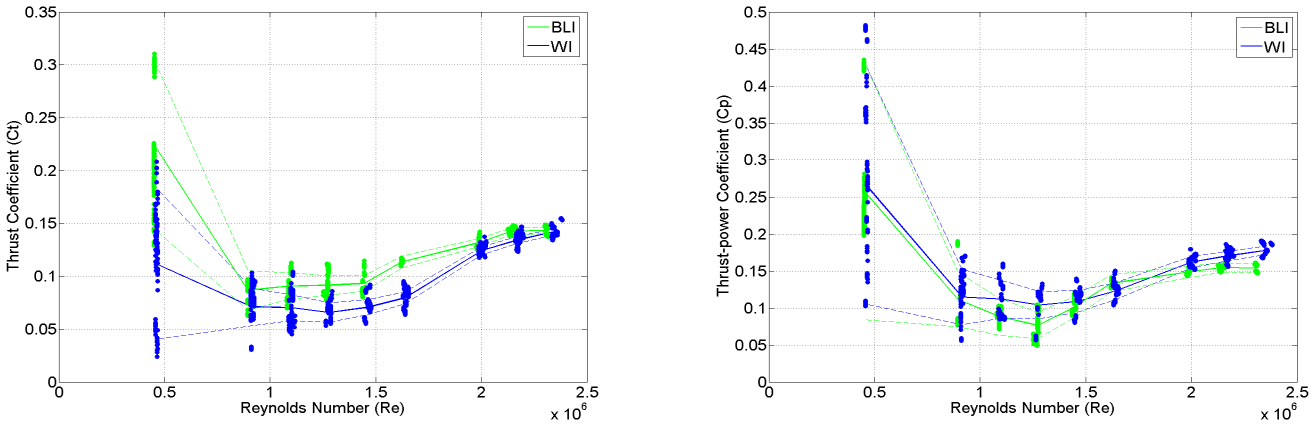

(a) Ct for WI and BLI Configurations

(b) Cp for WI and BLI Configurations

Figure 9-5: Thrust and Thrust-Power Coefficient for WI and BLI Configuration with 95% Confidence Interval

$$C_T = \frac{T}{qS} \tag{9-2}$$

$$C_P = \frac{P_{shaft}}{qV_\infty S} \tag{9-3}$$

Figure 9-5 shows the thrust and thrust-power coefficient for WI and BLI configurations. It can be seen clearly that the measured observations lie inside the confidence interval. Also it can be seen that the measurements made around 500,000 Re, which represents a wind-speed value of 5 m/s, has an extreme large scatter. This shows that at this low speed, the uncertainty is very high making the measurements useless. The cause for this high scatter is due to the combined effect of dynamic pressure (q) and thrust (or torque for C_P) uncertainty. This can be concluded by observing the constant uncertainty of the thrust and torque for varying Re in Fig. 9-2 and 9-3 respectively. Taking a closer look at the uncertainty distribution for thrust and thrust-power coefficient in Fig. 8-13 and 8-14, it can be seen that the dynamic pressure uncertainty portion increases at this low speed regime. This is because the dynamic pressure uncertainty is constant throughout the entire wind-speed regime which becomes more dominant in slower wind-speeds where thrust and torque and significantly small. The thrust and thrust-power coefficient are repeated in Eqn. 9-2 and 9-3 respectively. The dynamic pressure is present in the denominator for C_T and C_P definitions. This makes it possible for these parameters to cause large scatter. For example, the thrust is divided by the dynamic pressure to get the thrust-coefficient. For relative low thrust values, the high constant uncertainty of the dynamic pressure causes the large scatter in C_T. The same holds for the thrust-power coefficient where torque is divided by the dynamic pressure.

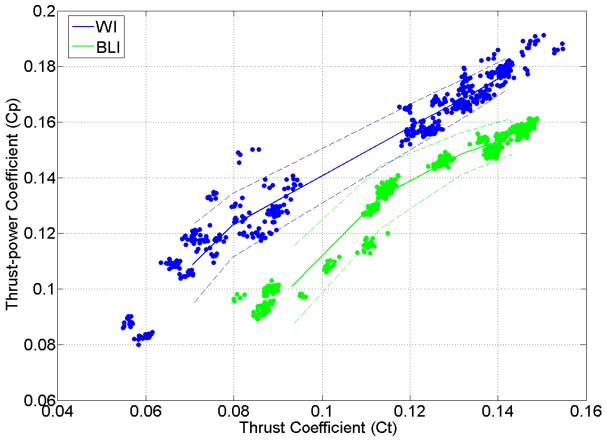

Figure 9-6: Thrust Coefficient vs. Thrust-Power Coefficient for WI and BLI Configuration with 95% Confidence Interval

Figure 9-6 shows the thrust coefficient (C_T) versus thrust-power coefficient (C_P). It can be seen that there exists a near linear relation between C_T and C_P. This is because an increase in thrust requires higher RPM which in turn increases the shaft-power (P_{shaft}) resulting in higher C_P. This plot is made for performance comparison purposes. A couple of observations can be made for this figure. First, the confidence interval follows the observations reasonably well which gives some confidence in the obtained results and calculations. Secondly, more importantly, is the fact that these confidence intervals do not overlap each-other. Because if the confidence intervals would overlap, a conclusion based on a comparison could hardly be made. Figure 9-6 shows clearly that the propulsor in BLI configuration requires less shaft-power (lower C_P) to generate the same thrust (C_T) for the entire measured wind-speed range. This shows that a propulsor in BLI configuration is more efficient compared to a propulsor operating in WI.

9-3 Constant Speed Setting Results

This section treats the results obtained during experiments for the so called 'constant speed' setting. For this setting, three different configurations are tested; free-stream propulsor, WI and BLI. The setup of these configurations can be visualized in Sec. 7-3 and 7-4. The three configurations are plotted in one graph for comparison. The graphs are grouped in such a way that the averaged curve with 95% confidence interval is plotted with and without the actual observations. This is performed because the observations drawn in the figure can cause the curve to be less visual. The averaged Re at which the configurations are tested can be found in Table 9-1. It is important that they are as identical as possible to make the comparison more realistic. Table 9-1 shows that the three configurations are tested in similar wind-speed regimes using the Re which is based on the used body.

Table 9-1: Reynolds Number for Various Configurations

Configuration	Reynolds Number
Free-stream propulsor	2.3541×10^6
Wake Ingestion	2.3549×10^6
Boundary Layer Ingestion	2.3207×10^6

$$J = \frac{V_\infty}{RPS \times D_{prop}} \tag{9-4}$$

Figure 9-7 shows propulsor performance in terms of thrust-power coefficient for each configuration. The figure is plotted using the advance ratio (J) which is defined in Eqn. 9-4. When a propeller is moving at high speed relative to the fluid, the advance ratio is a high number; and when it is moving at low speed the advance ratio is a low number. Since the propeller is not moving in the wind-tunnel and the wind-speed is fixed, the advance ratio is formed by changing the Rotations per Second (RPS) of the propulsor. An exponentially declining curve can be seen in Fig. 9-7. This is because, for an increase in advance ratio, the RPS needs to decrease which lowers the shaft-power inside the C_P. This relation becomes exponential because the shaft-power also decreases due to a reduction in torque. There exists a linear relation between torque and RPS which can be noticed when observing Fig. 8-9. Thus an increase in advance ratio due to a decrease in RPS means a squared decrease in shaft-power because there exists a linear relation between the torque and RPS for a constant wind-speed.

Figure 9-7(a) shows that for the same thrust-power, BLI advances more compared to WI and free-stream configurations. This can be seen from the fact that the curve for BLI is shifted to higher advance ratio's. Figure 9-7(b) shows the actual scattered measurements. It can be seen that these measurements lie inside the 95% confidence interval. This is mainly due to the fact that, referring to Fig. 9-5(b), the confidence interval for C_P reflects the scattered values in a satisfying manner.

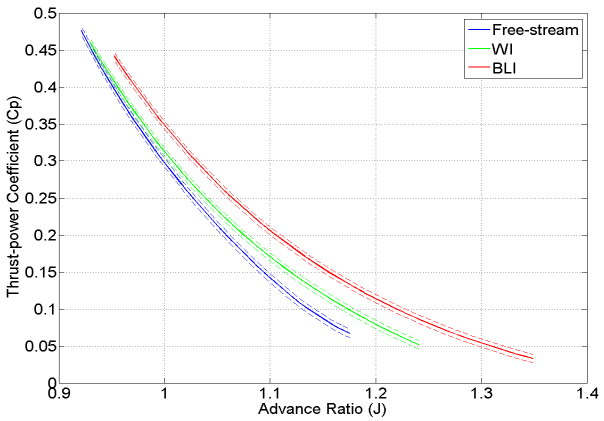

(a) J-Cp for Various Configurations

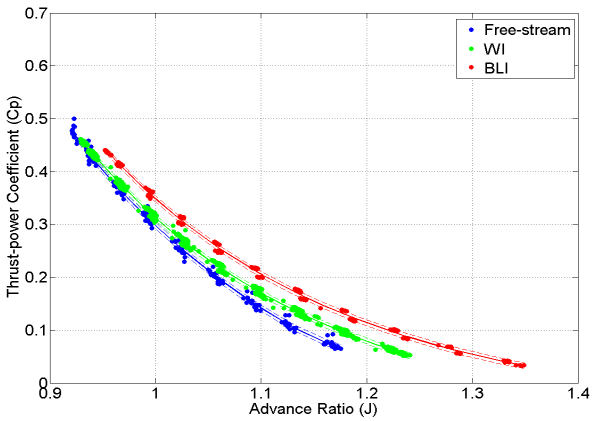

(b) J-Cp for Various Configurations with Observations

Figure 9-7: Thrust-Power Coefficient for Free-Stream, WI and BLI Configuration with 95% Confidence Interval

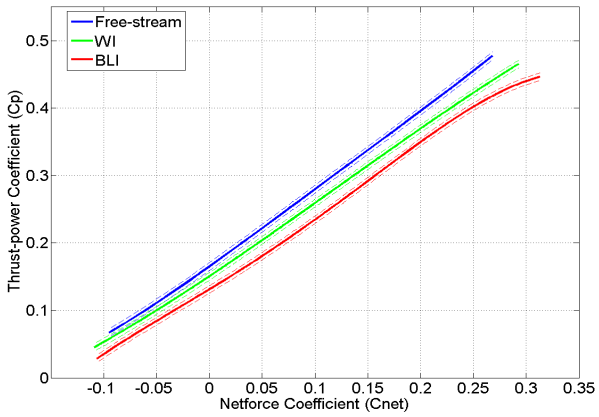

(a) $C_{(net-force)}$ vs. Cp for Various Configurations

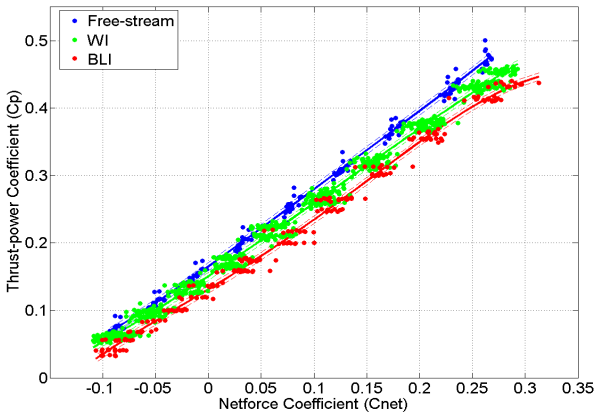

(b) $C_{(net-force)}$ vs. Cp for Various Configurations with Observations

Figure 9-8: Net-Force Coefficient vs. Thrust-Power Coefficient for Free-Stream, WI and BLI Configuration with 95% Confidence Interval

Figure 9-8 shows the net-force coefficient versus the thrust-power coefficient for free-stream, WI and BLI configurations. The equation used for the net-force coefficient can be found in Eqn. 9-5 where the body drag term is found using Eqn. 8-9 for WI and BLI configurations. For the free-stream configuration, in which the airframe is not present, the body drag term is found using Eqn. 8-8. It must be realized first that the net-force coefficient mimics flight behavior, meaning that a net-force equal to zero can be interpreted as an aircraft in cruise condition. A positive and negative net-force coefficient can be regarded as ascending and descending of the aircraft respectively.

$$C_{(net-force)} = \frac{T - D_{body}}{q \times s} \tag{9-5}$$

A positive linear relation can be found when observing Fig. 9-8. This is because an increase in net-force means an increase in thrust which requires more shaft-power. Observing Fig. 9-8(a) a clear conclusion can be drawn, namely that BLI consumes less shaft-power for the entire net-force range whether it is positive or negative. Remember that the thrust-power coefficient is comprised out of the shaft-power (see Eqn. 9-3). Figure 9-8(b) shows the results including the measurements. The measurements for WI and BLI seem to be scattered in the horizontal net-force direction. This is due to the combination of thrust and drag measurement uncertainties involved in these configurations when calculating the net-force coefficient. This is not the case for the free-stream configuration because here the net-force is computed simply by measuring only the thrust and subtracting a calculated body drag value. The measured values lie properly inside the (vertical) confidence interval for thrust-power coefficient but poorly in the horizontal direction. Nonetheless, if the average shaft-power benefit is taken the following percentages arise; 9% benefit for WI and 18% for BLI w.r.t. free-stream case.

The propeller efficiency is plotted in Fig. 9-9. In Eqn. 3-2 the definition for the propeller efficiency can be found. Note that it is different from the propulsive efficiency. It can be seen in Fig. 9-9 that the propulsor in BLI and WI configuration has a higher propeller efficiency w.r.t. free-stream configured propulsor. Taking an advance ratio equal to 1 gives 11% efficiency increase for WI and 21% increase for BLI configurations w.r.t. free-stream propulsor configuration. The efficiency increase w.r.t. free-stream configuration grows even further for higher advance ratios. It is nice to see that the confidence interval of these separate performance curves do not intersect and that the measurements are positioned for a great part inside the calculated 95% confidence interval (See Fig. 9-9(b)).

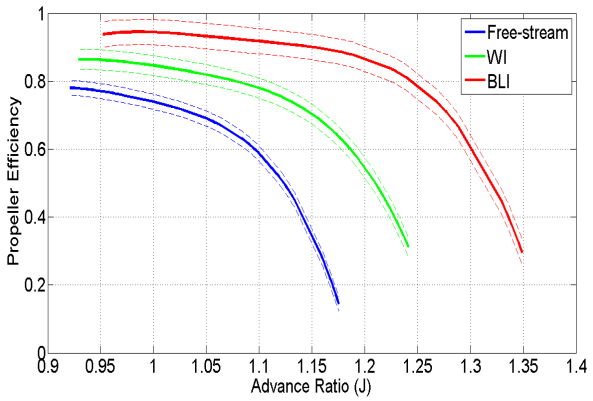

(a) Propeller Efficiency for Various Configurations

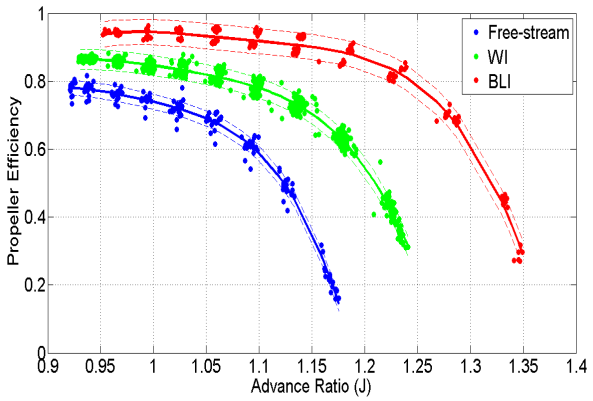

(b) Propeller Efficiency for Various Configurations with Observations

Figure 9-9: Propeller Efficiency vs. Advance Ratio for Free-Stream, WI and BLI Configurations with 95% Confidence Interval

9-4 PIV Results

This section deals with the results obtained using PIV measurement technique. The theory behind this technique is treated in Ch. 5. The experimental setup required for this technique can be found in Sec. 7-5. PIV is performed for 'constant-speed' setting where the wind-speed is fixed at a value that coincides with 26 m/s. Three configurations are tested; free-stream propulsor, WI and BLI. Post-processing PIV data for BLI posted difficulties which could

not be solved in time for this report. This is the reason why, in this section, the free-stream propulsor and WI configurations are compared and BLI is omitted. The same holds for the uncertainty and error analysis, which are omitted in Peijian et al. (2015) and therefore also omitted in this section. This unfortunately means that the uncertainty of the obtained PIV values are unquantified.

In Fig. 9-10 the Control Volume (CV) used for PIV can be found with the velocity vectors illustrated by the colored bar. This CV is captured using the setup illustrated in Fig. 5-2 where the green rectangle suggests this CV. Figure 9-10 is generated by averaging 700 sets of pictures at the timing of random propeller blade phases. Monte Carlo time averaging of these data sets eliminates the transient effect. The velocity field is aligned with the defined coordinate, and trimmed by the boundary illustrated as the green dashed line in Fig. 9-10(b). It can be seen in Fig. 9-10(b) that close to the surface of the propeller hub the flow stagnates. This is depicted in dark blue region. Also, a value close to 26 m/s in the far edges of the CV can be observed. This shows that the CV is sufficiently large to capture the effects of the propeller. Another observation is the propeller loading visible as dark red region in front and aft the propeller blade. Note that the upper boundaries in Fig. 9-10 is not a horizontal line, but actually a stream line starting from a point at inlet. This stream line allows a convenient integration without considering the flow penetrating the boundary. The thick blue dashed line in Fig. 9-10(a) depicts the CV inlet and outlet surface used for computations.

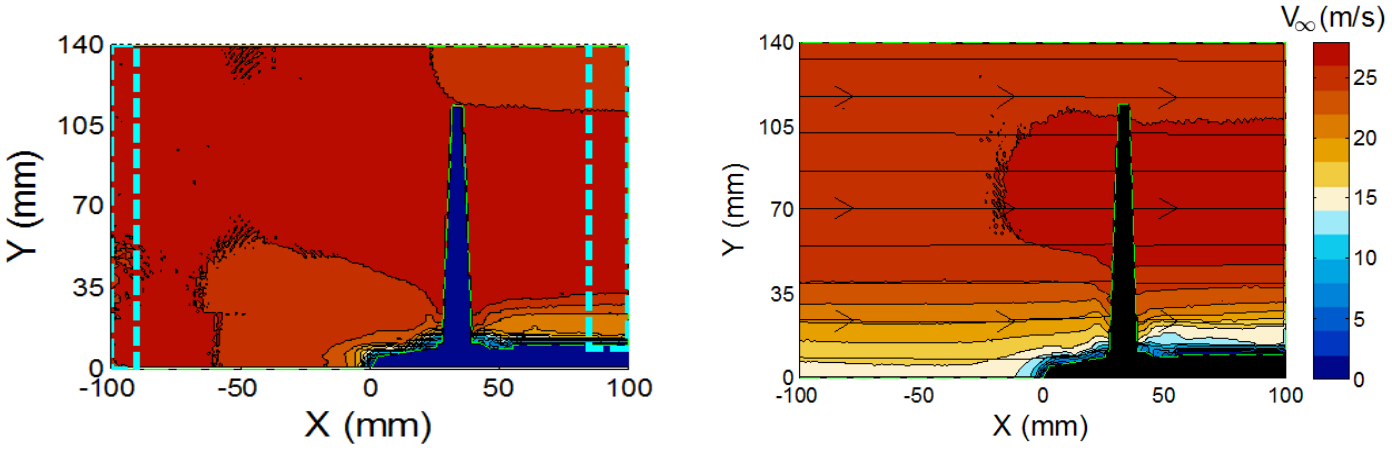

(a) Velocity Magnitude Contour for Free-stream Propulsor

(b) Velocity Magnitude Contour for WI Propulsor

Figure 9-10: Velocity Magnitude Contour for Free-stream and WI Configured CV[20]

The velocity components can also be generated using pressure measurements. The pitot-static tube is traversed vertically (in y-direction) for two x-locations; -100 (CV inlet) and +100 (CV outlet). These locations coincide with the blue dashed region in Fig. 9-10(a). The results of this pressure survey for WI configuration can be found in Fig. 9-11. Comparing the velocity components found using pressure measurements (Fig. 9-11) with velocity components found using PIV (Fig. 9-10(b)) it can be seen that they are equal. Which builds confidence in the measurement technique. Propeller loading aft of the propeller could also be sensed by the pitot-static tube because a bulge is present in Fig. 9-11(b).

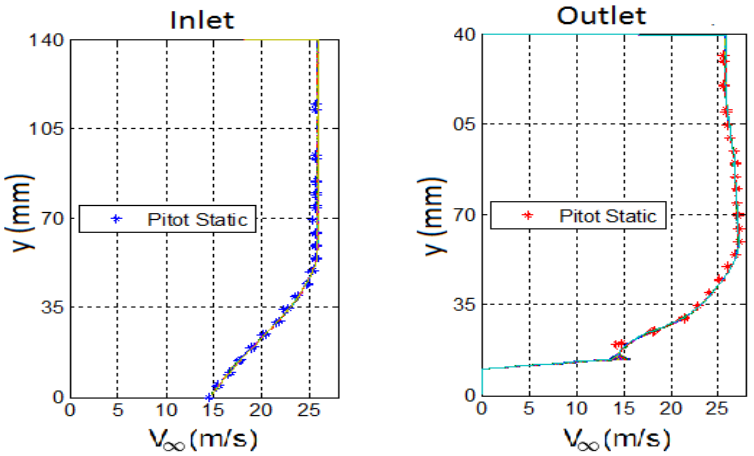

(a) Velocity at inlet (x = -100) (b) Velocity at outlet (x = +100)

Figure 9-11: Velocity Distribution using Pressure Survey at CV Inlet and Outlet[20]

Using the velocity vector fields found in Fig. 9-10, the momentum difference can be calculated. First the 2D plane depicted in Fig. 9-10 needs to be integrated over 360 degrees. Then, the velocity integral is taken at inlet and outlet of the circular surface. This is performed in order to compute the force of the propeller since it is directly related to the momentum excess. The equation to compute the momentum can be found in Eqn. 9-6a. Note that it has no pressure terms. In order to compute the momentum excess provided by the propeller, the velocity addition w.r.t. free-stream value is integrated over the entire surface (See Eqn. 9-6b).

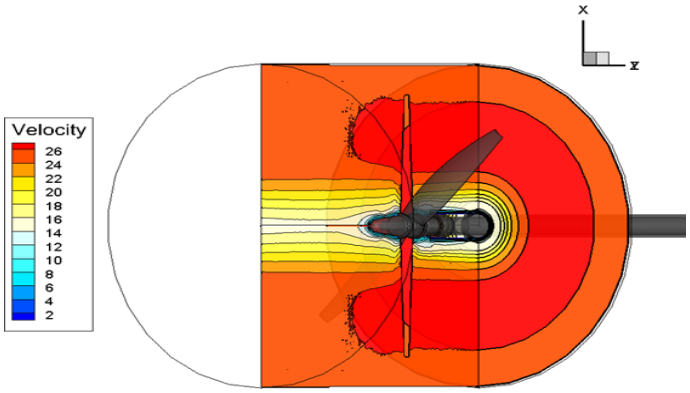

Figure 9-12: Integrating Velocity Components over Entire Propeller Surface[20]

$$M = \iint \rho u dA \tag{9-6a}$$

$$M_{excess} = \Delta M = \iint \rho u \times (u - V_\infty) dA \tag{9-6b}$$

For the next couple of pages, WI configuration is highlighted in order to treat the problems and inconsistencies in a more clear and detailed manner. The results for free-stream configuration is integrated at the end of this section.

The result of the integration using Eqn. 9-6b can be found in Fig. 9-13(a). Here it can be seen that the WI propeller creates a momentum excess equal to 0.75 N. Before proceeding any further, the mass conservation law for the CV depicted in Fig. 9-10(b) can be checked. The mass-flow history can be found in Fig. 9-13(b). Here it can be seen that mass conservation law is obeyed since the mass-flow at inlet and outlet of CV is (almost) identical.

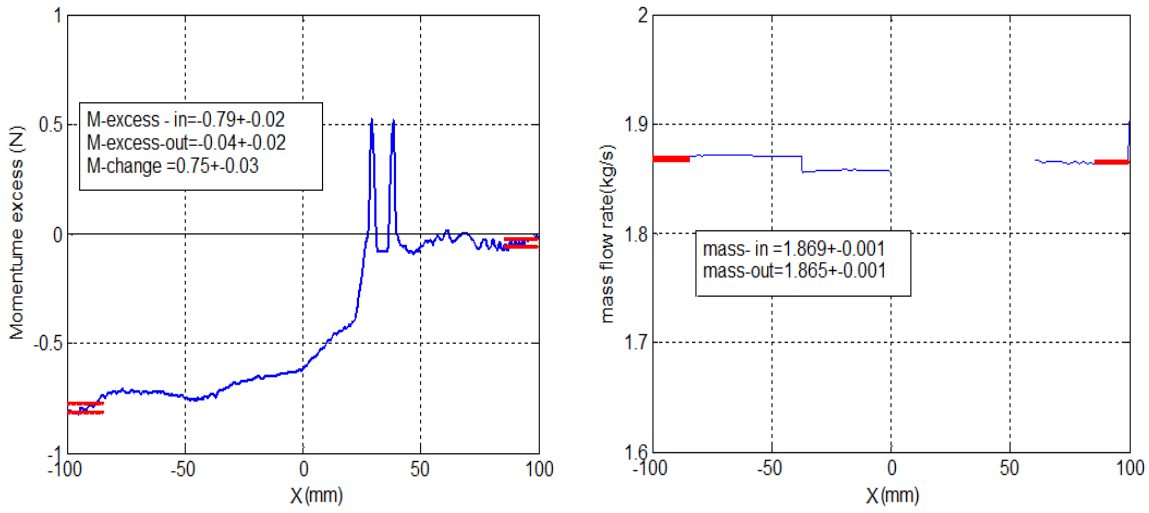

(a) Momentum Distribution Along x-axis

(b) Mass-flow Distribution Along x-axis

Figure 9-13: WI Configuration: Momentum and Mass-flow Distribution Along CV x-Axis[20]

The thrust which is found using the momentum equations can be compared with the actual load cell measurements. This is performed in Fig. 9-14 where the orange observations denote the load cell measurements accompanied by the uncertainty level (orange bar). In the same graph the thrust obtained from momentum equations using PIV is found in blue. Here it can be seen that the load cell measures significantly higher thrust values w.r.t. PIV, around 0.47 N. Remember that the thrust found using momentum equations assume that the static pressure remains constant throughout the CV. This assumption needs to be checked because it is suspected to cause the inconsistency between load cell and PIV results.

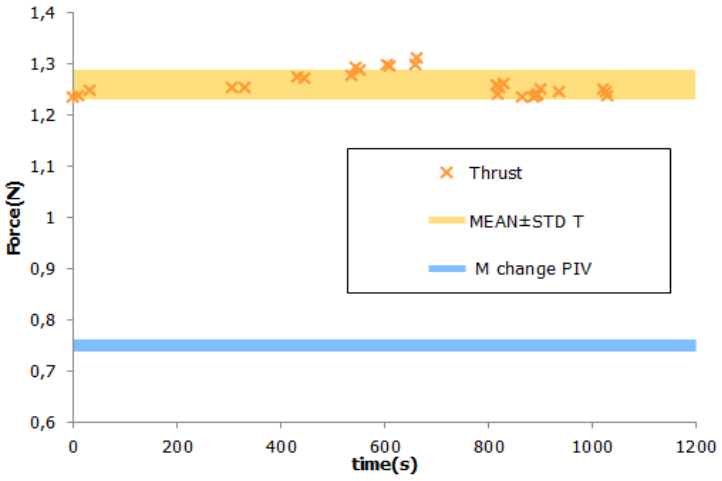

Figure 9-14: WI Configuration: Thrust Values found using Load Cell and PIV[20]

Figure 9-15 shows the static pressure at CV inlet (left, blue) and outlet (right, red). Here an average difference of 5 Pa can be found. Meaning that the static pressure increases with 5 Pa from CV inlet to outlet. This value might seem small but nothing is further from the truth because the force of this pressure, calculated using Eqn. 9-7, gives a value of 0.35 N. Note that the surface (S) coincides with inlet and outlet surface of the CV. This additional static pressure explains a large portion of the discrepancy between load cell measurements and PIV measurement. Please note that the load cell of course senses this pressure rise as a pulling force which is neglected in PIV momentum relations.

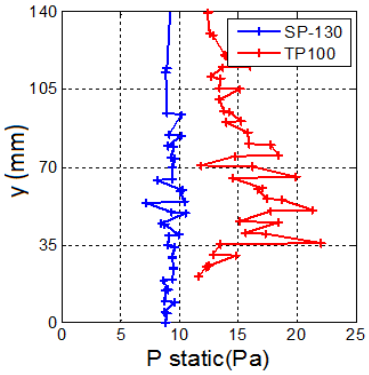

Figure 9-15: WI Configuration: Static Pressure for CV Inlet (left,blue) and Outlet (right,red)[20]

$$\Delta F = S \times \Delta P = 0.07 \times 5 = 0.35N \tag{9-7}$$

Data misalignment can also be the cause for the difference that exists between load cell and PIV measurements. In Fig. 9-16(a) the misalignment of the calibration plate w.r.t. the propeller shaft can be observed. It can be seen from Fig. 9-16(b) that the calibration plate is rotated by 0.482 deg w.r.t. the shaft of the propeller, when observed by the camera. The shaft is carefully aligned with the wind-tunnel test-section using lasers (See Fig. 9-17). Here the red laser light is positioned perpendicular to wind-tunnel test-section.

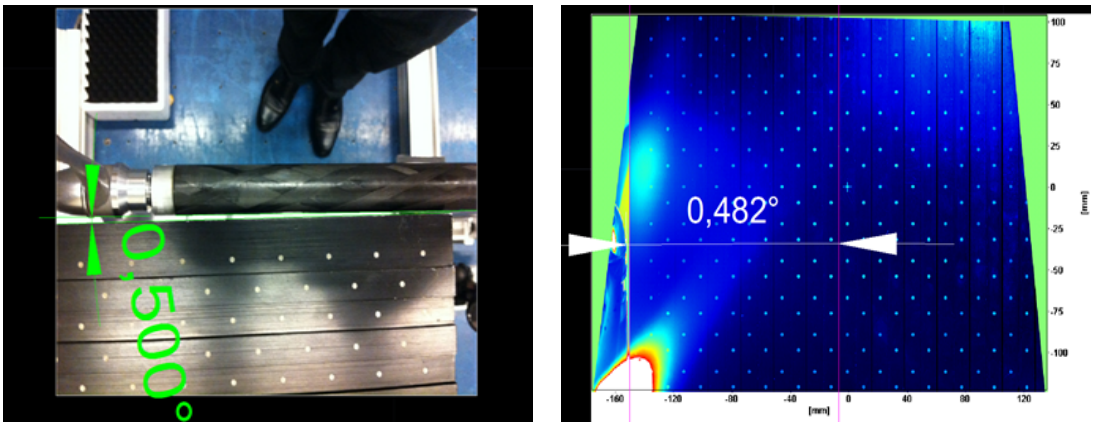

(a) Top-view: Calibration Plate Misalignment (b) Camera-view: Calibration Plate Misalignment

Figure 9-16: Misalignment of the Calibration Plate w.r.t. Propulsor Shaft[20]

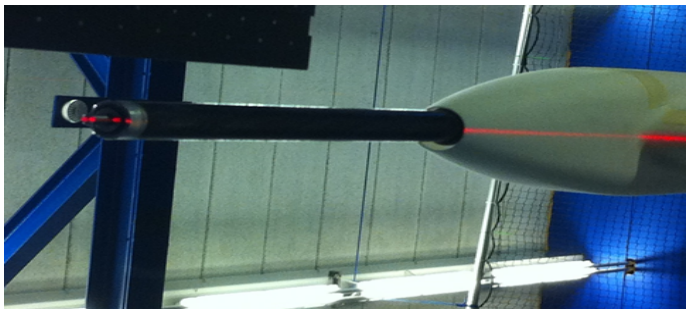

Figure 9-17: Shaft Alignment w.r.t. Wind-Tunnel Test Section using Laser[20]

Thus the misalignment of the calibration plate can also be the cause of the discrepancy that exists between load cell measurements and PIV measurements. This can be checked by simply rotating the data in PIV during post-processing and computing the momentum equations over again. In Table 9-2, the calculated momentum and force for PIV with and without rotation of the CV can be found. Since the pressure term found earlier accounts for 0.35 N, the alignment needs to be performed such that the force from the momentum analysis must be around 1 N. In order to increase the momentum excess to 1 N, the CV needs to be rotated by 2 deg and translated 3 mm. The CV for this case can be found in Fig. 9-18. For this case however, the mass-flow conservation law is not obeyed. This can be observed in Table 9-2 where the difference in mass-flow inlet and outlet can be observed. This means that the value found without post-processing the CV alignment (0.5 deg) captures the flow direction better since here the mass-flow is conserved. This concludes that post-processing CV alignment does not improve PIV results.

Table 9-2: WI Configuration: Thrust and Momentum for PIV Alignment

Parameters	0.5 deg misaligned	2 deg + 3 mm misaligned
Momentum Defect at Inlet	0.86	1.12
Momentum Defect at Outlet	0.08	0.13
Thrust	0.78	1.00
Mass-flow at Inlet	2.146	2.121
Mass-flow at Outlet	2.142	2.015

Since changing CV alignment poses problems in mass conservation, only the pressure term remains as a means of improving results such that PIV coincides with the actual load cell measurements. The pressure term, neglected in momentum equations, can also be reconstructed using PIV measurements. The direct consequence of including the static pressure in theoretical sense means that the power balance equation defined in Eqn. 6-1 needs to be transformed into Eqn. 9-8. Here the static pressure term is included for the wake and propulsor. If an even more realistic representation of the power terms is required, the swirl and viscous dissipation terms might also be added on the right hand side of Eqn. 9-8. In order to properly capture the pressure term it needs to be constructed through the entire CV. The process for doing this is complicated. It involves solving the Poisson equation by using an iterative process by first applying discretization to the 2D Cartesian equation. For further details regarding pressure reconstruction using PIV data, reference is made to Peijian et al. (2015). Reconstructing the pressure inside the CV for both configurations results in Fig. 9-19. By integrating the pressure for the entire surface of the CV gives the force. The computed pressure and momentum force can be plotted in Fig. 9-20.

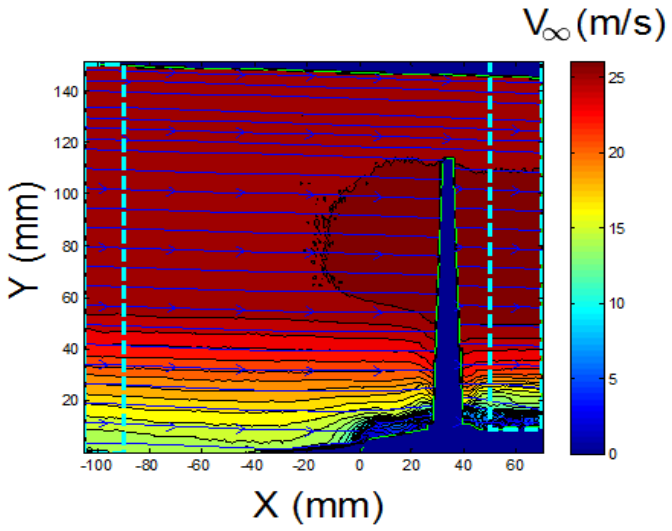

Figure 9-18: WI Configuration: CV for (2 deg + 3 mm) Change in Data Alignment[20]

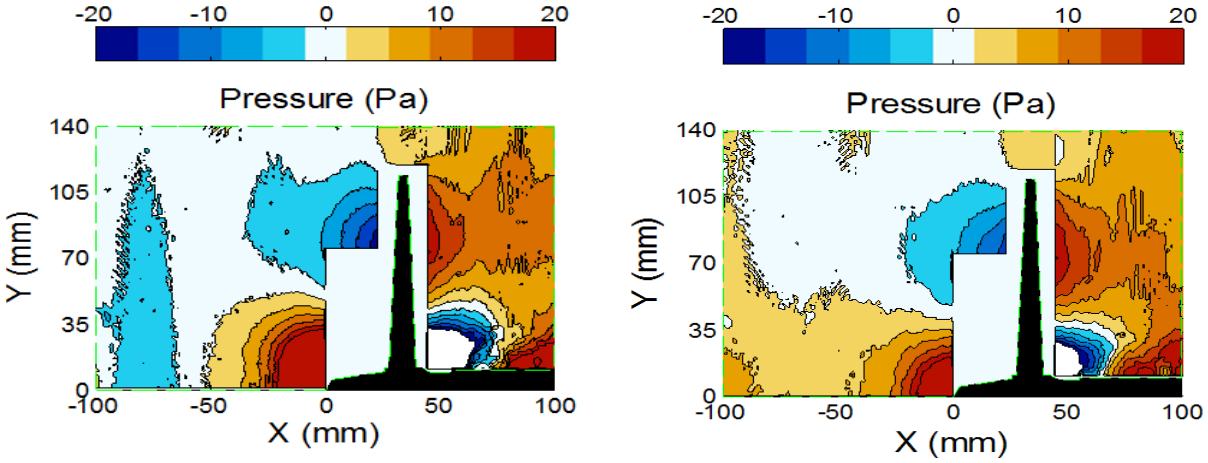

(a) Reconstructed Static Pressure for Free-stream CV

(b) Reconstructed Static Pressure for WI CV

Figure 9-19: Reconstructed Static Pressure for Both Configurations[20]

$$(\dot{E}_{\text{wake,body}} + p_{(wake,in)}) + (\dot{E}_{\text{kinetic energy}} + p_{(propulsor)}) = TV_{\infty} + (\dot{E}_{\text{wake, propulsor}} + p_{(wake,out)}) \tag{9-8}$$

A couple of observations can be made for Fig. 9-20. For Fig. 9-20(b), the momentum excess is tuned such that there exists no momentum excess at CV outlet plane. This tuning causes the momentum excess to start negatively. It can be seen that the total momentum excess through the CV equals 0.75 N for WI, which was already found and plotted in Fig. 9-13(a) of course. Continuing the observations for Fig. 9-20(b) shows that the static pressure, obtained by solving the Poisson equation, is increased by the propulsor to a value that depicts 0.5 N. This value coincides with the body force of the propeller. This means that a total of 1.13 N is captured by PIV. This matches the load cell measurement of 1.25 N more closely for WI configuration.

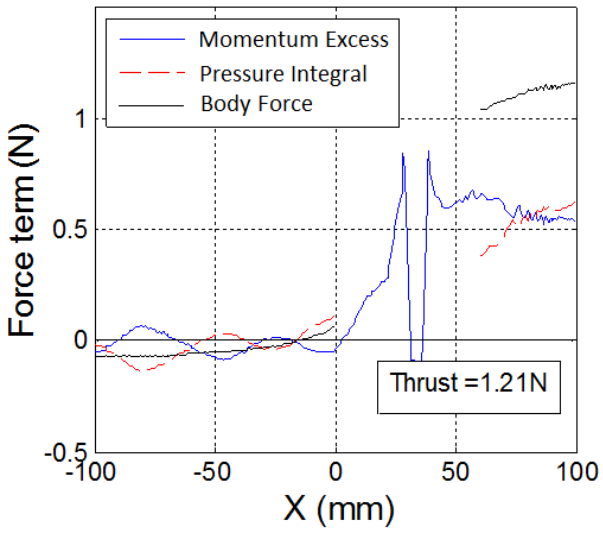

(a) Distribution Along x-axis for Free-stream

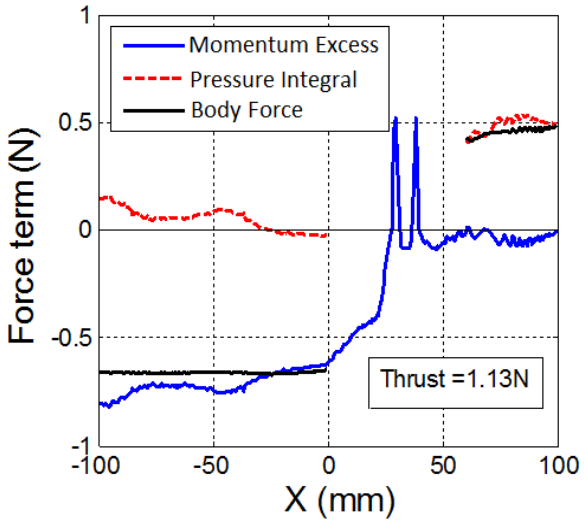

(b) Distribution Along x-axis for WI

Figure 9-20: Momentum and Pressure Distribution Along x-axis for Free-stream and WI[20]

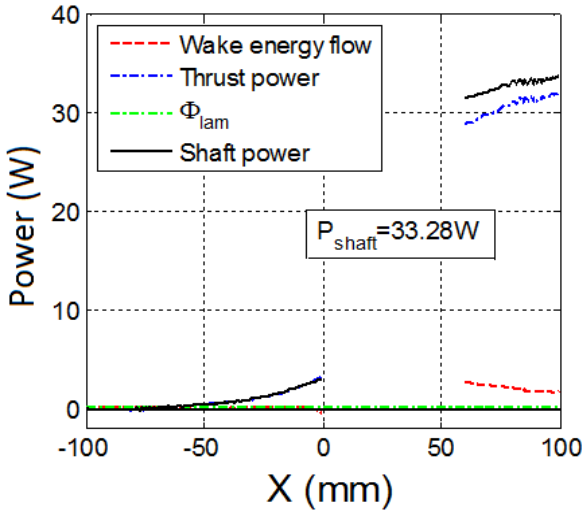

(a) Power Balance Integral Terms for Free-stream

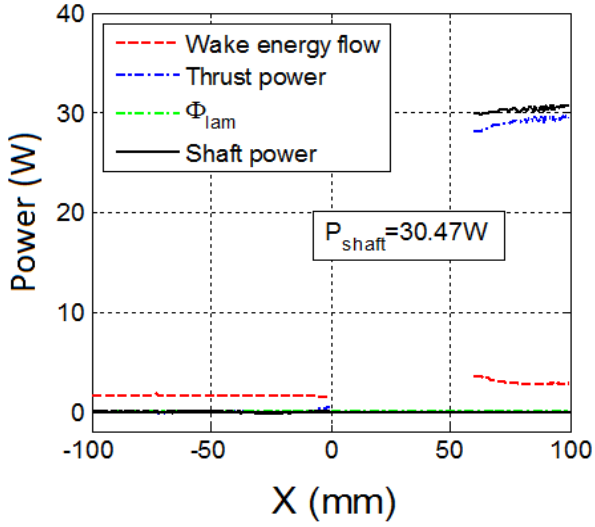

(b) Power Balance Integral Terms for WI

Figure 9-21: Power Balance Integral Terms for Free-stream and WI[20]

For free-stream configuration, depicted in Fig. 9-20(a), the momentum excess is trimmed in a way that it starts with zero and ends with a positive value. Here it can be seen clearly that the force produced by a momentum excess equals 0.5 N. The force produced by the presence of static pressure equals around 0.71 N. The addition of these forces gives a value of 1.21 N. This value closely coincides with load-cell measurements (See Table. 9-3). This firmly concludes that the static pressure term cannot be neglected for both configurations since its effect is significant.

PIV is also used to capture other power terms. In Fig. 9-21 the wake energy, thrust-power, viscous dissipation and shaft-power are plotted. It can be seen clearly that the dissipation term is negligible. Also, a higher wake behind the propeller can be visualized which is caused by the increase in wake flow velocity. The shaft-power term is slightly larger than the thrust-power term for both configurations. If the thrust-power becomes lower for the same shaft-power, the propulsor becomes less efficient. Observing Fig. 9-21 more closely it shows that the thrust and shaft-power are significantly larger than the wake power. This shows that a limited amount of power gain can be realized by utilizing the wake for performance increase. A simple and quick glans to Fig. 9-21(b) shows that if the entire wake energy is utilized, a power gain of around 3 W is possible. This power is then subtracted from the shaft-power which accounts for roughly 9.84% power gain. This value was also found in Sec. 9-3. Thus the body wake energy causes the efficiency increase. This observation was already introduced theoretically by Peijian in Sec. 4-1 where he states that the body wake is an intermediate power term explaining the efficiency increase. For the free-stream case, there exists no wake to be utilized since there is no body which creates it. This can be seen in Fig. 9-21(a) where there exists no wake energy before the propeller but is present after it.
To compare PIV data with the data obtained using more conservative instruments (load cell, balance, torque sensor etc.) for the 'constant speed' setting, gives Table. 9-3. It can be seen that the thrust values for free-stream configuration are similar. For WI configuration, the thrust obtained using PIV is 0.12 N lower w.r.t. load cell measurement. When taking a look to the shaft-power values in Table. 9-3, it can be noticed that PIV produces values that lie 10 W lower for both configurations. Thus the results in Table 9-3 unfortunately show that PIV produces different values compared to the conservative instruments used in the wind-tunnel. A possible reason for this discrepancy can be originated from the error embedded in the pressure reconstruction. Also, turbulent dissipation is a possibility which is not captured using PIV. Laminar dissipation power term is captured which can be found in Fig. 9-21(b). Remember that the standard deviation for the obtained values are omitted for PIV values since the error analysis posed unsatisfactory results.

Table 9-3: Thrust and Shaft-power for Free-stream and WI

Parameters	Free-stream	WI	Unit
Thrust using Load-cell	1.226 ± 0.012	1.259 ± 0.023	N
Thrust using PIV	1.21	1.13	N
Shaft-power using Multiple Instruments	44.501 ± 1.260	40.651 ± 0.495	W
Shaft-power using PIV	33.28	30.47	W

Fig. 9-22 is included to visualize the swirl and laminar dissipation power terms w.r.t. thrust-power. Here the power decomposition of the CV can be found for WI configuration. Here it can be seen that the swirl component is almost negligible compared to the thrust-power. Using the power terms in Fig. 9-22 the shaft-power can be derived by simply applying the Power Balance Method (PBM) equation provided in Eqn. 9-8. Figure 9-22 shows that different power terms present in WI can be quantified using PIV.

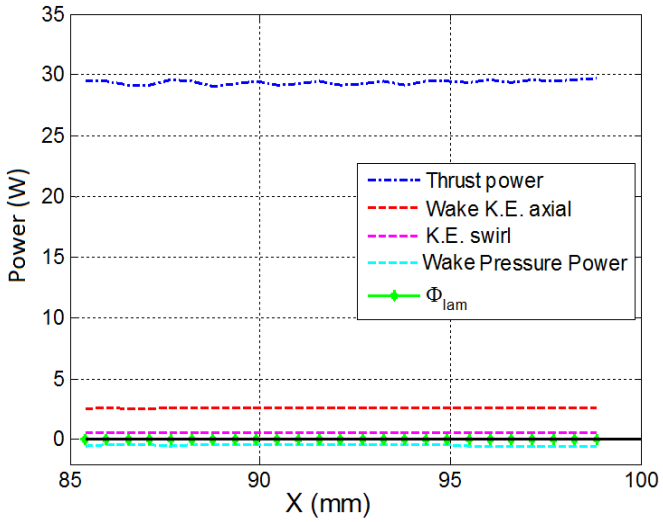

Figure 9-22: Power Decomposition for WI at 'Constant Speed' Wind-Tunnel Setting[20]

Chapter 10

Conclusion and Recommendations

This thesis work has focused on answering two main research questions proposed in Sec. 1-2. These are answered theoretically and experimentally in Sec. 10-1. The recommendations can be found in Sec. 10-2.

10-1 Conclusions

Theoretical Conclusions

- In the Wake Ingestion (WI) configuration, the actuator uses the body wake Kinetic Energy (K.E.) flow as power input and therefore saves losses from the downstream wake. Compared to a conventional free-stream actuator, a substantial power amount can be saved to generate equivalent thrust at same flight condition.

- The classical propulsive efficiency is not representative for WI and Boundary Layer Ingestion (BLI) configurations since the efficiency can exceed 100%. The power of the ingested body wake has been taken as external power source for propulsion. This external power source is not isolated in the propulsive efficiency by definition. This explains the value more than 1 observed in some previous studies.

- Using a propulsive efficiency definition that generates values below 100% for WI and BLI configurations requires the power of the propulsor to increase with an amount equal to $^1/_2 TV_\infty$. This amount of thrust-power can also be interpreted as drag-power for T=D configurations. This means that the wake generated by the body which needs to be restored extra by the propulsor equals $^1/_2 DV_\infty$.

- For the BLI integrated vehicle, the pressure distribution of the frontal body is affected by the propulsor suction. The interaction generally determines an increased body profile drag.

- BLI is characterized by less energy consumption and possibly higher airframe drag. To design the aircraft utilizing BLI, it is suggested to pursuit the minimization of the total power consumption, instead of the airframe drag.

Experimental Conclusions

- The benefits, in terms of shaft-power, are investigated for Wake Ingestion (WI) and Boundary Layer Ingestion (BLI) configurations using wind-tunnel experimentation. It is found that a propulsor in WI configuration saves 9% shaft-power w.r.t. an identical propulsor in free-stream configuration under equal net-force conditions. This power saving effect is more prominently present in BLI configuration where 18% power saving is measured. In terms of propeller efficiency these gains alter to 11% WI and 21% BLI configurations for an advance ratio equal to 1.

- Power Balance Method (PBM) is applied to define and quantify the power terms present in free-stream and WI configuration. The inter-relation between these power terms are quantified using Particle Image Velocimetry (PIV). The quantification showed that the shaft-power and thrust-power are significantly larger than laminar dissipation and wake kinetic energy power terms. More importantly, it showed that the utilization of wake energy is limited because it is a significantly lower energy source compared to thrust-power and shaft-power which drive the propeller efficiency.

- PIV in combination with conventional instruments such as torque sensor and load cell showed that the pressure term has a substantial impact and should therefore be integrated in the PBM as an additional power term. It has been shown that including the pressure term in the PBM results in Eqn. 9-8.

10-2 Recommendations

- In theoretical sense a new propulsive efficiency definition is required which can deal with tightly integrated propulsor configurations. An attempt is made by the author which can be disproved or extended. It is recommended to prove whether these newly developed definitions have physical significance.

- The interaction between propulsor and body needs to be understood better. The propulsor in BLI configuration accelerates the air around the body, decreasing the static pressure and thus increasing the pressure drag. It would be helpful to quantify this effect experimentally.

- The performance decrease of the propulsor unit due to unsteady wake ingestion is a large topic which needs to be investigated further. The question remains whether the efficiency gain outweighs the financial setbacks such as lower lifetime of blades due to unsteady blade loading. Vibrations that require more maintenance etc.

- For future experiments it is highly discouraged to perform real-time processing during experimental conduct. This is the main reason why equilibrium condition was not satisfied.

- The airframe and propulsor unit must be coupled to measure the net-force instead of deriving it. Every derivation is accompanied by higher uncertainties.

- Pressure measurements were unreliable because the pitot-static probe was vibrating at high speeds. A better design is proposed for the future to increase pressure measurement fidelity. The same holds for the propulsor tube which was also vibrating, partly because the motor shaft was bent. A better non-vibrating design is proposed.

- The wind-tunnel dynamic pressure uncertainty causes relatively large deviations for very low wind-speeds (5-10 m/s). These deviations cause large scatter for non-dimensionalized coefficients that use this dynamic pressure. This should be improved.
- Better preparation and experience is required for processing PIV data. Processing the data posed many problems for Peijian that could not be resolved in time. This is the reason why there is no uncertainty analysis, no BLI configuration results and poor consistency between PIV and other measurement results. It is believed that pressure recovery techniques for PIV caused this poor consistency.

Appendix A

Derivation for Drag

In this chapter, the drag for an airfoil inside a Control Volume (CV) is derived using momentum analysis. Momentum analysis is easily applied in finding an expression for the drag of a body by calculating the momentum loss in its wake. When a viscous fluid moves past a body, the shear stresses cause a momentum reduction. This can be seen in the CV depicted in Fig. A-1. For this case, steady, incompressible, 2D flow is assumed. The viscous effects along the control surface are neglected. Stream surfaces are used for upper/lower boundaries of the CV meaning that there is no flow crossing the top and bottom. The control surface is at a distance from the body in all directions such that the pressure equals the ambient atmospheric pressure. The width of the CV, into the paper direction, is assumed to be taken as z.

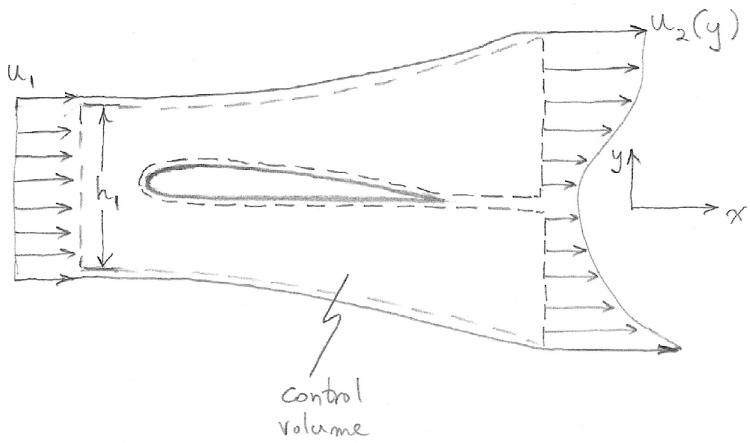

Figure A-1: CV for Airfoil in Free Flight[18]

In order to keep the derivation clear, integral notations are worked out and emerge only in the final expressions. It is important to realize that the airfoil exerts a viscous force (using its Boundary Layer (BL)) on the fluid inside the CV which slows it down reducing the momentum. Thus the momentum out (location 2) is smaller than momentum in (location 1). According the Newton's second law, a time rate of change of momentum equals a force. Thus the only step which is needed is taking the x-momentum change per unit time through

the entire CV (see Eqn. A-1).

$$F_x = \dot{M}_{x,out} - \dot{M}_{x,in} = \dot{M}_2 - \dot{M}_1 \tag{A-1}$$

$$\dot{M}_2 = M_2 u_2(y) = \rho z \int_2 u_2(y) u_2(y) dy \tag{A-2}$$

$$\dot{M}_1 = M_1 u_1 = \rho z h_1 u_1 u_1 \tag{A-3}$$

Substituting Eqns. A-2 and A-3 in Eqn. A-1 gives the force in x-direction which is the drag of the body in Eqn. A-4.

$$D = \rho z \int_2 u_2(y) u_2(y) dy - \rho z h_1 u_1 u_1 \tag{A-4}$$

Using the mass conservation law expressed in Equation A-5, the surfaces between surface 1 and 2 can be related. Substituting Eqn. A-6 in Equation A-4 gives the usable full expression of the drag in Equation A-7. It can be seen clearly that the drag depends on the velocity differences between the two planes of the CV. Note that the velocity terms are interchanged due to sign convention. This means that drag results in a positive number using Eqn. A-7 since exit velocities (at point 2) are lower than inlet velocities (point 1). Applying the same principles to derive the thrust, the same equation can be found (see Eqn. B-2). But in this case, equation B-2 generates negative numbers meaning a force is produced in opposite (thrust) x-direction.

$$\rho z h_1 u_1 = \rho z h_2 u_2 \tag{A-5}$$

$$h_1 = \frac{h_2 u_2}{u_1} \tag{A-6}$$

$$D = \rho z \int_2 u_2(y)(u_1 - u_2(y)) dy \tag{A-7}$$

$$T = \rho z \int_2 u_2(y)(u_1 - u_2(y)) dy \tag{A-8}$$

Appendix B

Derivation for Propulsive Efficiency

B-1 Momentum Theory

In this section, the momentum theory is applied to generate an expression for the propulsive efficiency. First a Control Volume (CV) is defined (see Fig. B-1). The CV shown in Fig. B-1 assumes the boundaries far enough from the actuator disk device such that the pressure is everywhere equal to a constant. Assuming a steady flow, Newton's second law can be applied in the positive x-direction (see Eqn. B-1). The only force on the control volume is due to the change in momentum flux across its boundaries because the pressure forces are assumed equal. This yields an expression for the thrust provided in Eqn. B-2.

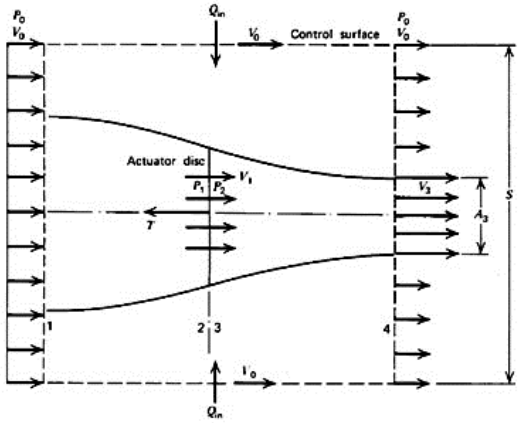

Figure B-1: Control Volume for Analysis of Propeller[3]

$$\sum F_{\mathrm{x}} = \int_{\mathrm{surface}} u_{\mathrm{x}} \rho \vec{u} \vec{n} dS \tag{B-1}$$

$$T = \dot{\mathrm{m}}(u_{\mathrm{e}} - u_{\mathrm{o}}) \tag{B-2}$$

The power imparted to the fluid which is the change in kinetic energy of the flow as it passes through the propeller, can be found in Eqn. B-3. This term is considered as E_{in} because

the propeller engine requires energy to spin the propeller blades which in turn causes an increase in kinetic energy inside the predefine CV. Note that u_e and u_o correspond to the velocity after and before the propulsor respectively. Notice that the power consumed to cause a rotational movement of the propeller is assumed to be equal to the kinetic energy increase inside the CV by the propeller blades. This is the conservation of energy in the conversion process. Propulsive power, the rate at which useful work is done, is defined as the thrust multiplied with flight velocity. This can found in Eqn. B-4. The propulsive efficiency is simply the ratio between propulsive power and the power imparted to the fluid (see Eqn. B-5). Thus in effect, the propulsive efficiency measures the effectiveness of a propulsive device in converting mechanical power input (which is assumed to equal the kinetic energy increase to the fluid) to propulsive power output. Working out the velocity terms gives the equation for the propulsive efficiency in Eqn. B-6.

$$P_{KE} = \dot{m}\left(\frac{u_e^2}{2} - \frac{u_o^2}{2}\right) \tag{B-3}$$

$$P_{\text{propulsive}} = T u_o \tag{B-4}$$

$$\eta = \frac{\text{propulsive power output}}{\text{mechanical power input}} = \frac{\text{propulsive power output}}{\text{power imparted to fluid}} = \frac{T u_o}{\dot{m}(\frac{u_e^2}{2} - \frac{u_o^2}{2})} \tag{B-5}$$

$$\eta = \frac{2}{1 + \frac{u_e}{u_o}} \tag{B-6}$$

B-2 Actuator Disk Theory

In order to apply the actuator disk theory, the following assumptions are adopted:
1. Assume infinite number of blades that form a thin disk.
2. Neglect rotation, compressibility and unsteadiness in the flow.
3. Assume discontinuous pressure change and continuous velocity change (see Fig. B-2)

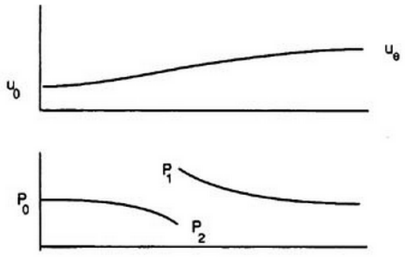

Figure B-2: Schematic of Actuator Disk Model[3]

A CV is taken around the actuator disk (see Fig. B-3).

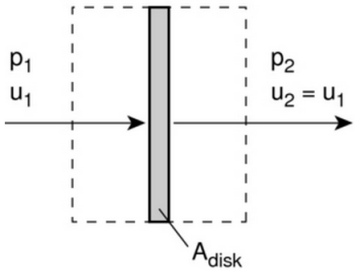

Figure B-3: CV Around Actuator Disk[3]

Using the assumptions and defined CV, the force (Eqn. B-7), thrust power (Eqn. B-8), disk velocity (Eqn. B-9) and massflow (Eqn. B-10) can be defined. The propulsive efficiency (Eqn. B-12) can be found by an integration process of the massflow in the thrust equation and applying the ratio between thrust power and kinetic energy imparted on the fluid (Eqn. B-11).

$$T = A_{\text{disk}}(p_2 - p_1) \tag{B-7}$$

$$\text{Thrust Power} = Tu_{\text{disk}} = A_{\text{disk}}(p_2 - p_1)u_{\text{disk}} = \dot{m}(u_{\text{e}} - u_{\text{o}})u_{\text{disk}} \tag{B-8}$$

$$u_{\text{disk}} = \frac{(u_{\text{e}} + u_{\text{o}})}{2} \tag{B-9}$$

$$\dot{m} = \rho u_{\text{disk}} A_{\text{disk}} = \rho A_{\text{disk}} \frac{(u_{\text{e}} + u_{\text{o}})}{2} \tag{B-10}$$

$$\text{Kinetic Energy Imparted on Fluid} = \dot{m}\left(\frac{u_{\text{e}}^2 - u_{\text{o}}^2}{2}\right) \tag{B-11}$$

$$\eta = \frac{2}{1 + \sqrt{\frac{T}{0.5 A_{\text{disk}} u_{\text{o}}^2 \rho} + 1}} \tag{B-12}$$

Appendix C

Load-Cell Calibration Results

In this chapter, the raw measurements regarding the load-cell calibration can be found for both isolated and integrated load-cell configurations. The setup for these configurations can be visualized in Fig. 6-7.

The results for the isolated calibration using 50, 100, 200 and 500 grams can be found in Fig. C-1(a), C-1(b), C-1(c) and C-1(d) respectively. Observing these results it can be seen that the load cell measures values (in red) that are biased upwards between 0.3% and 0.8% w.r.t the applied weight (in blue). Biased values are relatively constant and small such that it can be accounted for. This means that the load cell performs satisfying.

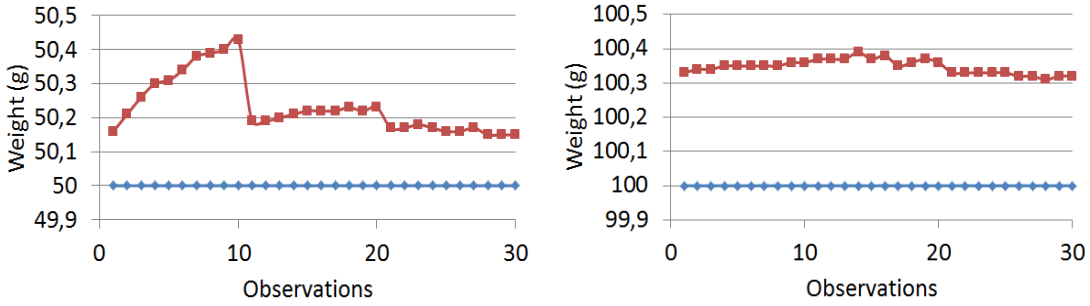

(a) Applying 50 Grams of Weight

(b) Applying 100 Grams of Weight

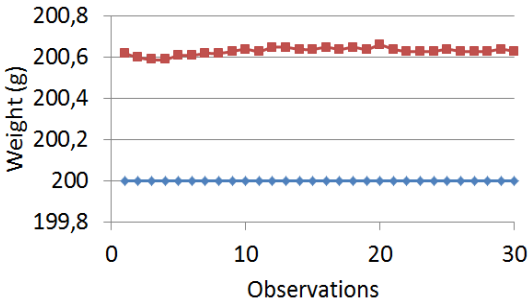

(c) Applying 200 Grams of Weight

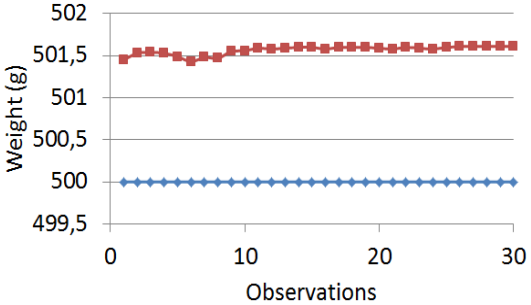

(d) Applying 500 Grams of Weight

Figure C-1: Isolated Load Cell Calibration Results: Applied Weight (blue) vs. Measured Weight (red)

The results for the integrated (Fig. 6-7(b)) load cell calibration using 50, 100, 200 and 500 grams can be found in Fig. C-2(a), C-2(b), C-2(c) and C-2(d) respectively. Observing these results it can be seen that the load cell measures values (in red) that deviate less than 0.14% from the true value (in blue). Because the deviations are smaller using the L-shaped hook (see Fig. 6-7(b)) it can be concluded that the integration of the hook does not have a negative effect for the measurements.

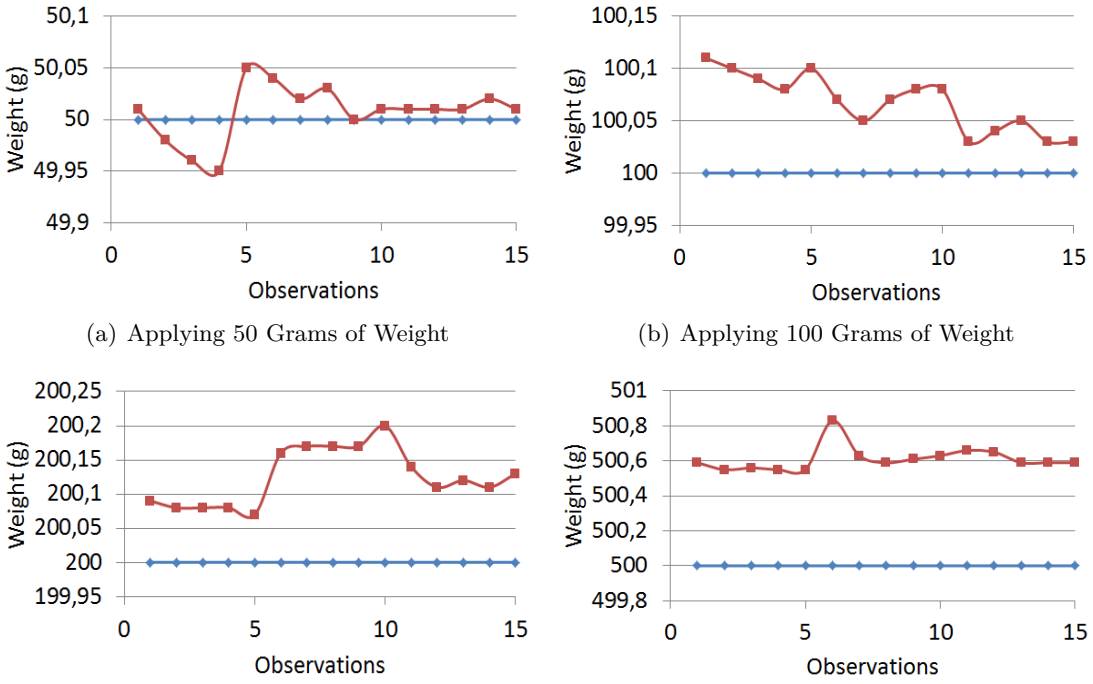

(a) Applying 50 Grams of Weight

(b) Applying 100 Grams of Weight

(c) Applying 200 Grams of Weight

(d) Applying 500 Grams of Weight

Figure C-2: Integrated Load Cell Calibration Results: Applied Weight (blue) vs. Measured Weight (red)

Appendix D

Uncertainty Propagation Equations

$$\rho = \left(\frac{\rho_o \times T_o}{p_o}\right) \times \left(\frac{p}{T}\right) \tag{D-1a}$$

$$V_\infty = \sqrt{2 \times \frac{q}{\rho}} \tag{D-1b}$$

$$\mu = \mu_o \times \left(\frac{T}{T_o}\right)^{1.5} \times \left(\frac{T_o + C}{T + C}\right) \tag{D-1c}$$

$$RPS = \frac{RPM}{60} \tag{D-1d}$$

$$Re = \frac{V_\infty \times \rho \times l}{\mu} \tag{D-2a}$$

$$J = \frac{V_\infty}{n \times D_{prop}} \tag{D-2b}$$

$$P_{shaft} = 2\pi \times Tor \times RPS \tag{D-2c}$$

$$P_{thrust} = T \times V_\infty \tag{D-2d}$$

$$\eta_{prop} = \frac{P_{thrust}}{P_{shaft}} \tag{D-2e}$$

$$C_P = \frac{P_{shaft}}{q \times V_\infty \times S} \tag{D-2f}$$

$$C_T = \frac{T}{q \times S} \tag{D-2g}$$

$$\sigma_{Re} = l \times \frac{V_\infty \rho}{\mu} \times \sqrt{\left(\frac{\sigma_{V_\infty \rho}}{\overline{V_\infty \rho}}\right)^2 + \left(\frac{\sigma_\mu}{\overline{\mu}}\right)^2} \tag{D-3a}$$

$$\sigma_J = \frac{V_\infty}{n D_{prop}} \times \sqrt{\left(\frac{\sigma_{V_\infty}}{\overline{V_\infty}}\right)^2 + \left(\frac{\sigma_n}{\overline{n}}\right)^2} \tag{D-3b}$$

$$\sigma_{P_{shaft}} = 2\pi \times Tor \times RPS \times \sqrt{\left(\frac{\sigma_{Tor}}{\overline{Tor}}\right)^2 + \left(\frac{\sigma_{RPS}}{\overline{RPS}}\right)^2} \tag{D-3c}$$

$$\sigma_{P_{thrust}} = T \times V_\infty \times \sqrt{\left(\frac{\sigma_T}{\overline{T}}\right)^2 + \left(\frac{\sigma_{V_\infty}}{\overline{V_\infty}}\right)^2} \tag{D-3d}$$

$$\sigma_{\eta_{prop}} = \frac{P_{thrust}}{P_{shaft}} \times \sqrt{\left(\frac{\sigma_{P_{thrust}}}{\overline{P_{thrust}}}\right)^2 + \left(\frac{\sigma_{P_{shaft}}}{\overline{P_{shaft}}}\right)^2} \tag{D-3e}$$

$$\sigma_{C_p} = \frac{P_{shaft}}{q \times V_\infty \times S} \times \sqrt{\left(\frac{\sigma_{P_{shaft}}}{\overline{P_{shaft}}}\right)^2 + \left(\frac{\sigma_{qV_\infty}}{\overline{qV_\infty}}\right)^2} \tag{D-3f}$$

$$\sigma_{C_T} = \frac{T}{q \times S} \times \sqrt{\left(\frac{\sigma_T}{\overline{T}}\right)^2 + \left(\frac{\sigma_q}{\overline{q}}\right)^2} \tag{D-3g}$$

$$\sigma_\rho = \frac{T_o \rho_o}{p_o} \times \frac{p}{T} \times \sqrt{\left(\frac{\sigma_p}{\overline{p}}\right)^2 + \left(\frac{\sigma_T}{\overline{T}}\right)^2} \tag{D-4a}$$

$$\sigma_\mu = \mu_o \times \left(\frac{T_o + C}{T_o^{1.5}}\right) \times \frac{T^{1.5}}{T + C} \times \sqrt{\left(\frac{\sigma_T^{1.5}}{\overline{T^{1.5}}}\right)^2 + \left(\frac{\sigma_{T+C}}{\overline{T + C}}\right)^2} \tag{D-4b}$$

$$\sigma_{RPS} = \frac{1}{60} \times \sigma_{RPM} \tag{D-4c}$$

$$\sigma_{qv_\infty} = qV_\infty \times \sqrt{\left(\frac{\sigma_q}{\overline{q}}\right)^2 + \left(\frac{\sigma_{V_\infty}}{\overline{V_\infty}}\right)^2} \tag{D-4d}$$

$$\sigma_{V_\infty^2} = 2 \times \frac{q}{\rho} \times \sqrt{\left(\frac{\sigma_q}{\overline{q}}\right)^2 + \left(\frac{\sigma_\rho}{\overline{\rho}}\right)^2} \tag{D-5a}$$

$$\sigma_{V_\infty} = \frac{0.5 \times V_\infty \times \sigma_{V_\infty^2}}{\overline{V}_\infty^2} \tag{D-5b}$$

$$CI_{95\%} = \overline{y} \pm 2 \times \sigma \tag{D-6}$$

Appendix E

Data Processing Results

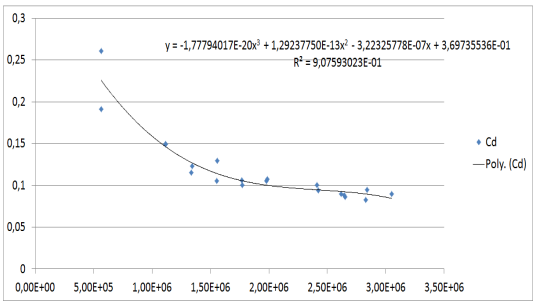

(a) Cycle 1

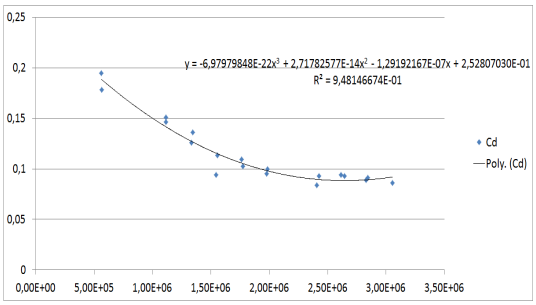

(b) Cycle 2

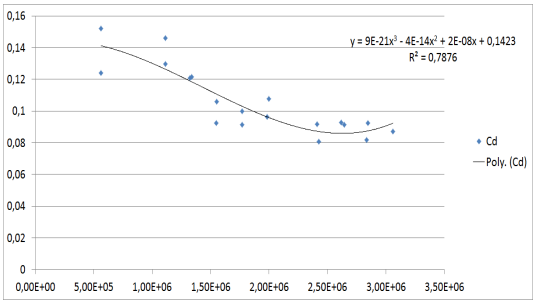

(c) Cycle 3

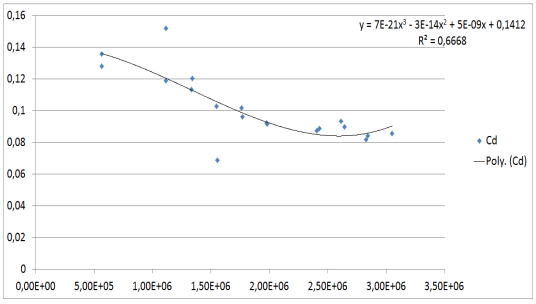

(d) Cycle 4

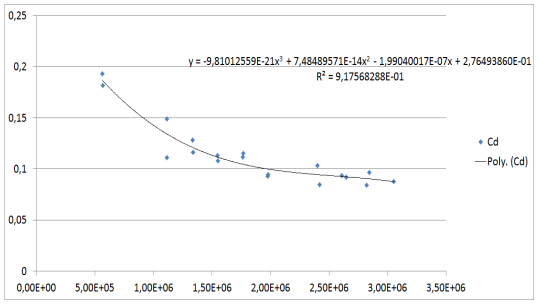

(e) Cycle 5

Figure E-1: Strut Drag Coefficient ($C_{d_{(Strut)}}$) vs. Re for Configuration with only Struts

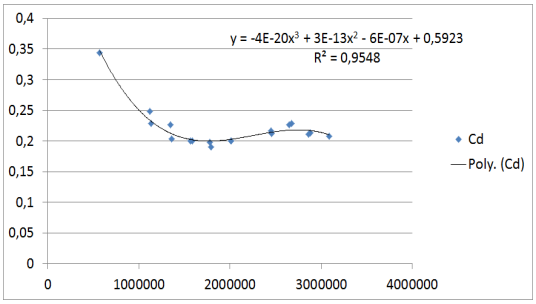

(a) Cycle 1

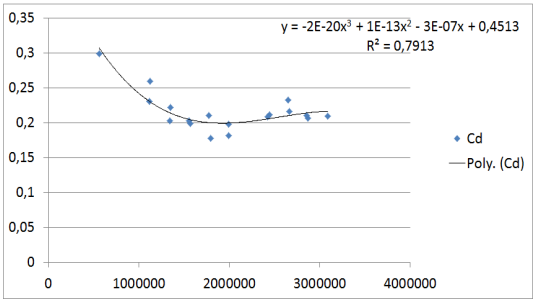

(b) Cycle 2

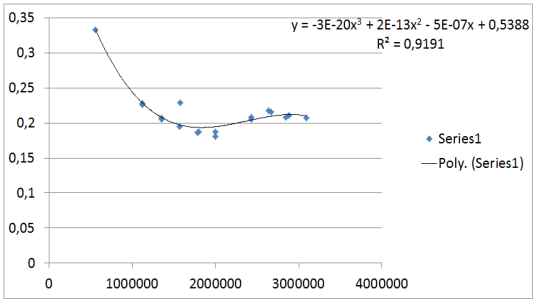

(c) Cycle 3

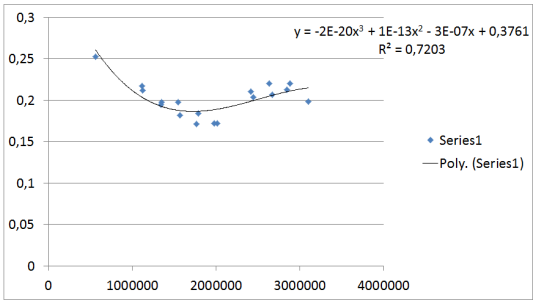

(d) Cycle 4

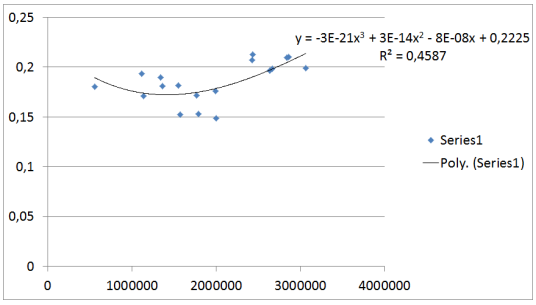

(e) Cycle 5

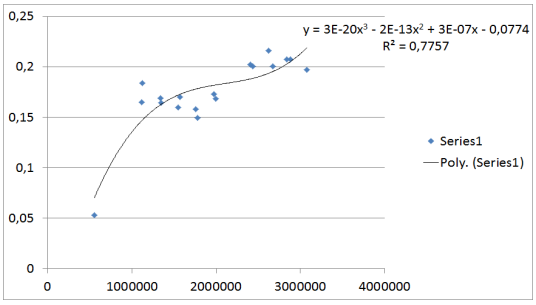

(f) Cycle 6

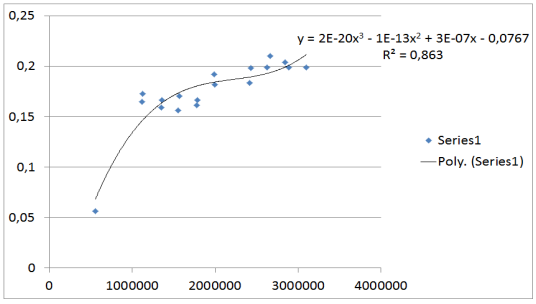

(g) Cycle 7

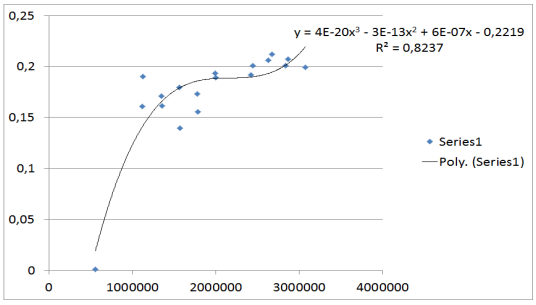

(h) Cycle 8

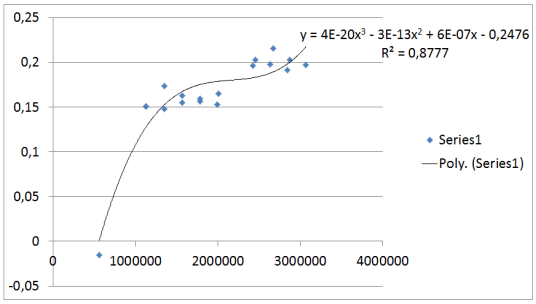

(i) Cycle 9

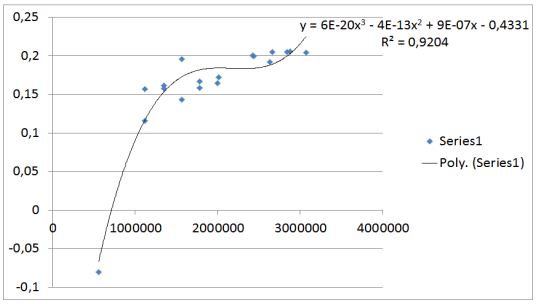

(j) Cycle 10

Figure E-2: $(C_{d_{(Body+Strut)}})$ vs. Re for Isolated Body Configuration

Bibliography

[1] Model 1668(S) Single Point Load Cells. URL http://www.bcmsensor.com/upload/1668(S)_single_point_load_cell_TEC.pdf.

[2] Left turning tendencies. URL http://users.skynet.be/sky92472/Ltt.htm.

[3] Production of thrust for a propeller. URL http://web.mit.edu/16.unified/www/SPRING/propulsion/UnifiedPropulsion7/UnifiedPropulsion7.htm.

[4] The Open Jet Facility. *Present Press B.V.*

[5] 68-95-99.7 rule. URL http://en.wikipedia.org/wiki/68%E2%80%9395%E2%80%9399.7_rule.

[6] Aviation and the Global Atmosphere, 2013. URL http://www.grida.no/publications/other/ipcc_sr/?src=/climate/ipcc/aviation/avf9-3.htm.

[7] S. Bell. Good Practice Guide A Beginner ' s Guide to Uncertainty of. (11):33, 1999.

[8] C.Krishnaswami. *Experimental Analysis of Near and Transitional Wind Turbine Wake Using Stereo Particle Image Velocimetry.* PhD thesis, Delft University of Technology, 2013.

[9] M. Drela. Power Balance in Aerodynamic Flows. In *27th AIAA Appl. Aerodyn. Conf.*, number June, San Antonio, 2009.

[10] S. Gorton, L. Owens, L. Jenkins, B. Allan, and E. Schuster. Active Flow Control on a Boundary-Layer-Ingesting Inlet. *42nd AIAA Aerosp. Sci. Meet. Exhib.*, pages 1–12, Jan. 2004. doi: 10.2514/6.2004-1203. URL http://arc.aiaa.org/doi/abs/10.2514/6.2004-1203.

[11] L. W. Hardin, G. Tillman, O. P. Sharma, and N. Glenn. Aircraft System Study of Boundary Layer Ingesting Propulsion. (August):1–12, 2012.

[12] C. He. *Wake Dynamics Study of an H-type Vertical Axis Wind Turbine.* PhD thesis, 2013.

[13] A. Kammerer. Blade Vibration Due to Inlet Flow Distortion, 2008. URL http://gasturbinespower.asmedigitalcollection.asme.org/article.aspx?articleid=1427250.

[14] Z. Kathleen. Glenn Aeronautics Research and Development, 2009. URL http://www.nasa.gov/centers/glenn/aeronautics/aero_overview.html.

[15] R. T. Kawai, D. M. Friedman, and L. Serrano. Blended Wing Body (BWB) Boundary Layer Ingestion (BLI) Inlet Configuration and System Studies. (December), 2006.

[16] L. D. Kral. Active Flow Control Technology. *ASME Fluids Eng. Div. Tech. Br.*, pages 1–28, 2009. URL http://files.asme.org/Divisions/FED/16309.pdf.

[17] H. McLemore Clyde. Wind-Tunnel Tets of a 1/20-Scale Airship Model with Stern Propellers. Technical report, National Aeronautics and Space Administration, Virginia, 1962.

[18] N. J. Mourtos. Momentum (Newton âĂŹ s 2 nd Law of Motion). pages 1–11. URL http://www.engr.sjsu.edu/nikos/courses/AE160/pdf/M3.E2.pdf.

[19] L. Peijian. A Conceptual Analysis of Boundary Layer Ingestion For Aircraft Application (Draft Version). page 27, 2014.

[20] L. Peijian. Powerpoint: BLI test 2014 V2, 2015.

[21] L. Peijian and A. G. Rao. Conceptual Analysis of Boundary Layer Ingestion Towards Aircraft Propulsion Integration. Technical report, 2013.

[22] L. Peijian, A. G. Rao, D. Ragni, and L. Veldhuis. *Conceptual Analysis of Boundary Layer Ingestion for Aircraft Application*. PhD thesis, 2015.

[23] A. Plas. *Performance of a Boundary Layer Ingesting Propulsion System*. PhD thesis, Massachusetts Institute of Technology, 2006.

[24] Scaime. Weighing Technology. URL http://www.scaime.com/en/4/support/general-information.html.

[25] F. Scarano. Experimental Aerodynamics. page 180, 2013.

[26] L. Smith. Wake Ingestion Propulsion Benefit. In *27th AIAA/SAE/ASME/ASEE Jt. Propuls. Conf.*, page 11, Sacramento, 1991.

[27] A. Uranga, M. Drela, E. M. Greitzer, N. A. Titchener, M. K. Lieu, N. M. Siu, A. C. Huang, G. M. Gatlin, J. A. Hannon, and N. Langley. Preliminary Experimental Assessment of the Boundary Layer Ingestion Benefit for the D8 Aircraft. pages 1–25, 2014.

Glossary

List of Acronyms

BLI	Boundary Layer Ingestion
WI	Wake Ingestion
PIV	Particle Image Velocimetry
NASA	National Aeronautics and Space Administration
GE	General Electric
AFC	Active Flow Control
BL	Boundary Layer
CFD	Computational Fluid Dynamics
Re	Reynolds Number
BWB	Blended Wing Body
PBM	Power Balance Method
CV	Control Volume
RPM	Rotations Per Minute
DUT	Delft University of Technology
OJF	Open Jet Facility
PIV	Particle Image Velocimetry
St	Stokes Number
API	Airframe Propulsion Interaction
TP	Trefftz Plane
K.E.	Kinetic Energy
SP	Survey Plane

NACA	National Advisory Committee for Aeronautics
Cd	Drag Coefficient
PTU	Processing Time Unit
FOV	Field of View
SD	Standard Deviation
RPS	Rotations per Second

List of Symbols

• A	Function
• $\overline{A}$	Mean of Function A
• A_{disk}	Surface Actuator Disk
• A_1, A_3, A_6, A_8, A_9 and A_{10}	Coefficient For Cycles 1,3,6,8,9 and 10 Respectively
• a	Coefficient
• $\hat{a}$	Estimated Coefficient a
• B	Function
• $\overline{B}$	Mean of Function B
• B_1, B_3, B_6, B_8, B_9 and B_{10}	Coefficient For Cycles 1,3,6,8,9 and 10 respectively
• b	Coefficient
• $\hat{b}$	Estimated Coefficient b
• C	Sutherland's Constant
• C_1, C_3, C_6, C_8, C_9 and C_{10}	Coefficient for Cycles 1,3,6,8,9 and 10 respectively
• C_d	Drag Coefficient
• $C_{d_{Average}}$	Average Drag Coefficient
• $C_{d_{body}}$	Body Drag Coefficient
• $C_{d_{body+strut}}$	(Body+Strut) Drag Coefficient
• $C_{d_{cycle-n}}$	Drag Coefficient for the nth Cycle
• $C_{d_{strut}}$	Strut Drag Coefficient
• $C_{net-force}$	Net-force Coefficient
• C_P	Thrust-power Coefficient
• C_p	Pressure Coefficient
• C_T	Thrust Coefficient
• $CI_{95\%}$	95% Confidence Interval
• D	Drag
• D_1, D_3, D_6, D_8, D_9 and D_{10}	Coefficient for Cycles 1,3,6,8,9 and 10 respectively
• D_{body}	Body Drag
• D_{prop}	Propeller Diameter
• DV_∞	Drag-power
• $\dot{E}_{\text{axial}}$ or $(\dot{E}_a)$	Axial Kinetic Energy (K.E.) Deposition Rate
• $\dot{E}_{\text{body,wake}}$	Body Wake Kinetic Energy Flux
• $\dot{E}_{\text{K.E}}$	Kinetic Energy Production Rate
• $\dot{E}_p$	Pressure-defect Work Rate
• $\dot{E}_{\text{prop,wake}}$ or $\dot{E}_{\text{propulsor,wake}}$	Propeller Wake Kinetic Energy Flux
• $\dot{E}_{\text{vortex}}$ or $(\dot{E}_v)$	Transverse K.E. Deposition Rate
• $\dot{E}_{\text{wave}}$ or $(\dot{E}_w)$	Wave Pressure Work Rate

- F_x Force in x-direction
- f_{corr} Wake Correction Factor
- h_1 Height for Control Volume Inlet
- h_2 Height for Control Volume Exit
- J Advance Ratio
- $KE_{body,wake}$ Kinetic Energy of Body Wake
- KE_{loss} Kinetic Energy Loss
- L or l Characteristic Length
- M Momentum
- M_1 Momentum at Control Volume Inlet
- M_2 Momentum at Control Volume Exit
- M_{excess} Excess Momentum
- $\dot{M}_1$ or $\dot{M}_{x_{in}}$ Time Rate of Change in Momentum at Control Volume Inlet
- $\dot{M}_2$ or $\dot{M}_{x_{out}}$ Time Rate of Change in Momentum at Control Volume Outlet
- $\dot{m}$ Mass-flow
- $\dot{m}_e$ Exit Mass-flow
- $\dot{m}_o$ Inlet Mass-flow
- $\dot{m_\infty}$ Undisturbed Far-field Mass-flow
- P or P_t Total Pressure
- P_{atm} Atmospheric Pressure
- P_0 Total Pressure In Far-field of Actuator Disk
- P_1 Total Pressure Before Actuator Disk
- P_2 Total Pressure After Actuator Disk
- P_{KE} Power by Kinetic Energy Increase
- P_k Net Mechanical Energy Inflow Rate
- $P_{propulsive}$ or P_{thrust} Thrust-power
- P_s Static Pressure
- P_{shaft} or (P_s) Shaft-power
- P_{total} Total Propulsor Power
- P_{useful} Useful Propulsor Power
- P_v Net Pressure-volume Power
- p_o Reference Pressure
- $p_{(propulsor)}$ Propulsor Static Pressure
- $p_{(wake,in)}$ Static Pressure at Propulsor Wake Inlet
- $p_{(wake,out)}$ Static Pressure at Propulsor Wake Outlet
- q Dynamic Pressure
- R_e Reynolds Number
- R^2 Coefficient of Determination
- S or s Frontal Surface
- St Stokes Number
- T Thrust
- T_o Reference Temperature
- TV_∞ Thrust-power
- t Time
- u or u_{out} Propeller Outlet Velocity
- u_j or u_e Jet Exit Velocity
- u_{in} Propeller Inlet Velocity

- u_w, u_{wake} or u_2 Wake Velocity
- u_∞, u_1 or u_o Free-stream Velocity
- u_{disk} Velocity at Actuator Disk
- V_∞ Free-stream Velocity
- v Wind-speed
- w Step function
- $\mathrm{W}\dot{h}$ Potential Energy Rate
- $\hat{y}$ Estimated Parameter
- z Control Volume Depth

- $\eta_{propeller}$ Propeller Efficiency
- η, η_p, η_{prop} or $\eta_{propulsive}$ Propulsive Efficiency
- η_{NEW} Newly Defined Propulsive Efficiency
- $\eta_{propulsive,free}$ Propulsive Efficiency for Free-stream Configuration
- $\eta_{prop,general}$ Propulsive Efficiency for the General Configuration
- $\eta_{p_{BLI}}$ Propulsive Efficiency for BLI Configuration
- η_{total} Control Volume Efficiency
- η_{WI} Propulsive Efficiency for WI configuration
- μ Dynamic Viscosity or Mean Value
- μ_o Reference Dynamic Viscosity
- ρ Density
- ρ_o Reference Density
- σ Standard Deviation
- σ_A Standard Deviation of Function A
- σ_B Standard Deviation of Function B
- σ_{AB} Cross-correlation between Functions A and B
- σ_{C_P} Standard Deviation of Shaft-power Coefficient
- σ_{C_T} Standard Deviation of Thrust-power Coefficient
- σ_f Standard Deviation of Function f
- σ_J Standard Deviation of Advance Number
- $\sigma_{P_{shaft}}$ Standard Deviation of Shaft-power
- $\sigma_{P_{thrust}}$ Standard Deviation of Thrust-power
- σ_{qv_∞} Standard Deviation of qv_∞
- σ_{Re} Standard Deviation of Reynolds Number
- σ_{RPM} Standard Deviation of Rotations per Minute
- σ_{RPS} Standard Deviation of Rotations per Second
- σ_T Standard Deviation of Thrust
- σ_{Tor} Standard Deviation of Torque
- σ_{v_∞} Standard Deviation of v_∞
- $\sigma_{v_\infty^2}$ Standard Deviation of v_∞^2
- σ_μ Standard Deviation of Dynamic Viscosity
- σ_ρ Standard Deviation of Density
- $\hat{\sigma}$ Estimated Standard Deviation
- $\hat{\sigma}^2_{calibration}$ Estimated Variance for Calibration Curve
- $\hat{\sigma}^2_{gauge}$ Estimated Variance for Digital Pressure Gauge
- $\hat{\sigma}^2_{pressure}$ Estimated Variance for Pressure
- Φ Viscous Dissipation Rate
- Φ_{BL} Viscous Dissipation Rate inside BL
- Φ_{lam} Laminar Viscous Dissipation Rate